UNIVERSITAT POLITÈCNICA
DE CATALUNYA
BARCELONATECH

Photodetectors based on low-dimensional materials and hybrid systems

Dominik Kufer

ICFO - The Institute of Photonic Sciences
Barcelona, 2016

Photodetectors based on low-dimensional materials and hybrid systems

Dominik Kufer

under the supervision of

Prof. Gerasimos Konstantatos

submitted this thesis in partial fulfillment
of the requirements for the degree of

Doctor

by the

Universitat Politècnica de Catalunya
Barcelona, 2016

To Iris and my family

Acknowledgements

This dissertation would not have been possible without the guidance and the support of several people. I am grateful to all who have contributed scientifically to this work or have supported me personally over the last couple of years.

Above all, I am deeply grateful to my supervisor Gerasimos Konstantatos who gave me the possibility to conduct my PhD in his group. I enjoyed an excellent working environment, in which he gave me direction, inspiration and plenty of freedom to pursue my own ideas. It was a great pleasure to work under your supervision.

Special thanks goes to my colleagues and friends from the SPNP group. First, I would like to express my gratitude to Silke Diedenhofen, who was my closest mentor in the first years at ICFO. Having someone like you around when starting a PhD is of great help. Thank you so much for all your support, for explaining me things with patience and for motivating me whenever I needed it. I have been lucky to share my office with Pelayo, David, Guillem and Luis. To Pelayo, I haven't met another person in my life who is so crazy and so brilliant at the same time. You helped me in so many ways during my PhD and made me laugh so many times. My years at ICFO wouldn't have been the same without you. David, your positive and happy attitude towards everything and everyone is unique. I hope you won't change that ever. Guillem a.k.a. Gilian, although we were just shortly office mates it was nice to have you around at the end of my time at ICFO. Thanks to the Rioja-ladies Maria and Tania, whom I had to annoy on a weekly basis to get my quantum dots. Maria, I appreciated you as a colleague and as a friend since the first day. I am very fortunate to have shared so many years with you at ICFO. To Nicky and Tim, thank you so much for proof-reading my thesis and for explaining us Europeans the american way of life at our lunch- and coffee-breaks. I am grateful to Agustin, who was a great support during the first years with helpful suggestions on how to survive a PhD. Finally I am thankful to all other group members with whom I have spent unfortunately too little time in our labs: Arup, Alex, Fiona, Luis, Helmut, Diana, Oscar, Santanu, Shuchi, Yu Bi, Jianjun and Nengjie.

I want to thank the cleanroom technicians Luis, Javi and Johann and PPL technician Vittoria. You guys do a great job and were always available when needed.

Special thanks to Frank Koppens for fruitful collaborations and his crew Stijn, Ivan and Gabi for all the useful discussions about hybrid detectors, for being good partners in the QD dealing business and for exchanging knowledge in the fabrication processes.

I am very grateful to all ICFOnians who helped me with other tasks: Anne for the warmest welcome possible at ICFO, Manuela, Cristina, Mery and Laia for handling all non-scientific issues and making my life easier, Rob for his great support during the last month.

During the course of this PhD I have met many great people at ICFO, too many to mention all of them here. I would like to especially thank Gabi and Esteban, who became good friends and with whom I shared many moments inside and outside ICFO. Gabi, you were from the beginning more a friend than a colleague and the most reliable person I have worked with at ICFO. Esteban, thanks for your patience when we tried to measure something useful for this stupid bowtie-experiment that has never led to anything. You started as my EBL-mentor in the clean-room and you have ended up as my best man. Pura vida!

Leider lässt sich wahrhafte Dankbarkeit mit Worten nicht ausdrücken. Ich möchte meinen Eltern, Gisela und Georg, ganz herzlich für ihre unermüdliche Unterstützung danken.

Por último muchísimas gracias a Iris, que ha tenido que aguantar la parte más dificil y animarme en momentos de crisis. Sin ti no hubiera empezado mi doctorado en Barcelona y hoy puedo decir que sin tu apoyo tampoco lo hubiera terminado. A ti y a tu familia os agradezco de todo corazón que me hayáis hecho sentir como en casa desde el primer día. Gracias por todo.

Contents

List of Figures **iii**

Abstract **v**

1 Introduction **1**

1.1 State-of-the-art photodetector technology 2
1.2 Photodetectors based on 2D materials 4
1.3 Thesis objectives 7
1.4 Thesis outline 8

2 Photodetection theory **11**

2.1 Photodetection mechanism 12
2.2 Figures of merit 17
2.2.1 Responsivity, quantum efficiency and gain 17
2.2.2 Dark current, noise and detectivity 18

3 Properties and characterization of 2D TMDCs **21**

3.1 Synthesis and electronic structure 22
3.2 Mechanical cleavage and device fabrication 23
3.3 Characterization techniques: AFM and Raman 24
3.4 Transport properties of MoS_2 27

4 Two-dimensional TMDC phototransistors **33**

4.1 Prior art in TMDC photodetection 34
4.2 Encapsulated monolayer MoS_2-FETs 35
4.3 Optoelectronic characteristics of MoS_2/HfO_2 38
4.3.1 Responsivity and charge carrier dynamics 38
4.3.2 Temporal response 41
4.3.3 Noise and sensitivity 43
4.4 Stability under environmental stress conditions 46

4.5 Encapsulation of other TMDCs: $MoSe_2$ 47
4.6 Summary and outlook 49

5 Hybrid 2D-0D TMDC-QD phototransistor 53
5.1 Colloidal quantum dots 54
5.2 Hybrid 2D–0D photodetectors 57
5.3 Vis-SWIR sensitive MoS_2/PbS photodetector 59
5.3.1 Doping effects after PbS deposition 60
5.3.2 Optoelectronic response and photocurrent dynamics 63
5.3.3 Backgate dependent sensitivity 66
5.4 Hybrid detectors based on other 2D and 0D systems 68
5.5 Summary and outlook 71

6 Interface engineering in hybrid TMDC-QD phototransistors 73
6.1 Device concept and electrical properties 74
6.1.1 Fabrication of MoS_2/TiO_2/PbS 74
6.1.2 Transport and doping 76
6.2 Fermi level pinning at the interface 76
6.3 Gate-dependent photoresponse and sensitivity 80
6.4 Summary and outlook 84

Conclusions 87

A Materials and methods 91

Bibliography 97

List of publications 115

List of Figures

1.1 2D material systems and flexible technology. 6

2.1 Photoconducting and photovoltaic mechnism. 14
2.2 Sensitized photo-FET and light induced shift 16
2.3 Noise power spectral density as a function of frequency. 18

3.1 MoS_2 structure and bandmodel. 23
3.2 Characterization techniques: Microscopy, AFM and Raman. 25
3.3 Few layer MoS_2 raman modes. 26
3.4 Thickness-depedent MoS_2-FET performance. 29

4.1 Encapsulated monolayer MoS_2-FET. 35
4.2 Device schematic, transfer, and output characteristics of MoS_2 and MoS_2/HfO_2 field effect transistor. 37
4.3 Optoelectronic response and charge carrier dynamics of MoS_2/HfO_2. 39
4.4 Encapsulation effect on photoresponse and temporal response of mono- and bilayer devices. 42
4.5 Measured noise and shot-noise limit of MoS_2/HfO_2 44
4.6 Gate-dependent performance parameters. 45
4.7 MoS_2 vs. MoS_2/HfO_2 device performance after exposure to humid conditions. 47
4.8 Modulation curves before and after encapsulation of $MoSe_2/HfO_2$ and MoS_2/Al_2O_3. 48
4.9 Full set of performance parameters of $MoSe_2/HfO_2$. 48

5.1 Hot-injection synthesis and ligand exchange of CQDs. 55
5.2 Absorbance spectra of PbS CQDs. 56
5.3 Device schematics and band alignment of MoS_2/PbS hybrid. 59
5.4 Transfer curves of MoS_2/PbS hybrids. 60
5.5 EDT doping effect and PbS reference transistor. 61

5.6 Isolation of PbS QDs from electrodes. 62
5.7 Spectral responsivity of MoS_2 and MoS_2/PbS hybrids. 63
5.8 Power-dependent optoelectronic response. 64
5.9 Gain mechanism and photocurrent dynamics. 65
5.10 Hybrid photodetector device characteristics. 67
5.11 Gate-dependent signal-to-noise ratio. 68
5.12 Hybrid PbS phototransistor based on $MoSe_2$ and WS_2. 69
5.13 Hybrid MoS_2/$AgBiS_2$ phototransistor. 70

6.1 Sequence of MoS_2/TiO_2/PbS device fabrication. 75
6.2 FET characteristics of MoS_2/TiO_2/PbS. 77
6.3 Modulation model and Fermi level pinning. 78
6.4 Transistor operation improvement after interface engineering. 79
6.5 Backgate dependent photoresponse. 80
6.6 MoS_2/TiO_2/PbS phototransistor properties. 82
6.7 Noise spectra and detectivity estimation. 83

Abstract

In the last decade, two-dimensional (2D) materials have attracted attention both in the nascent field of flexible nanotechnology as well as in more conventional semiconductor technologies. Within the rapidly expanding portfolio of 2D materials, the group of semiconducting transition metal dichalcogenides (TMDCs) has emerged as an intriguing candidate for various optoelectronic applications. The atomically thin profile, favorable bandgap and outstanding electronic properties of TMDCs are unique features that can be explored and applied in novel photodetecting platforms.

This thesis presents highly sensitive two-dimensional phototransistors made of sub-nanometre thick TMDC channels. Firstly, an encapsulation route is developed to address the detrimental and, to date, uncontrollable impact of atmospheric adsorbates, which severely deteriorate detector performance. The passivation scheme improves the transport properties of TMDCs, leading to high photoconductive gain with gate dependent responsivity of $10 - 10^4$ A/W throughout the visible, and temporal response down to 10 ms, which is suitable for imaging applications. The atomic device thickness yields ultra-low dark current operation and record detectivity of $10^{11} - 10^{12}$ Jones for TMDC-based detectors is achieved.

The use of monolayer TMDCs, however, has disadvantages like limited spectral absorption due to the bandgap and limited absorption efficiency. In order to increase the absorption and to extend the spectral coverage, TMDC channels are covered with colloidal quantum dots to make hybrid phototransistors. This compelling synergy combines strong and size-tunable light absorption within the QD film, efficient charge separation at the TMDC-QD interface and fast carrier transport through the 2D channel. This results in large gain of 10^6 electrons per absorbed photon and creates the basis for extremely sensitive light sensing. Colloidal quantum dots are an ideal sensitizer, because their solution-processing and facile implementation on arbitrary substrates allows for low-cost fabrication of hybrid TMDC-QD devices. Moreover, the custom tailored bandgap of quantum dots provides the photode-

tector with wide spectral tunability. For photodetection in the spectral window of NIR/SWIR, which is still dominated by expensive and complex epitaxy-based technologies, these hybrid detectors have the potential to favorably compete with commercially available systems.

The interface of the TMDC-QD hybrid is of paramount importance for sensitive detector operation. A high density of trap states at the interface is shown to be responsible for inefficient gate-control over channel conductivity, which leads to high dark currents. To maintain the unique electrical field-effect modulation in TMDCs upon deposition of colloidal quantum dots, a passivation route of the interface with semiconducting metal-oxide films is developed. The buffer-layer material is selected such that charge transfer from QDs into the channel is favored. The retained field-effect modulation with a large on/off ratio allows operation of the phototransistor at significantly lower dark currents than non-passivated hybrids. A TMDC-QD phototransistor with an engineered interface that exhibits detectivity of 10^{12} - 10^{13} Jones and response times of 12 ms and less is reported.

In summary, this work showcases prototype photodetectors made of encapsulated 2D TMDCs and TMDC-QD hybrids. Plain TMDC-detectors have potential for application as flexible and semi-transparent detector platforms with high sensitivity in the visible. The hybrid TMDC-QD device increases its spectral selectivity to the NIR/SWIR due to the variable absorption of the sensitizing quantum dots and reaches compelling performance thanks to improved light-matter interaction and optimized photocarrier generation.

1 Introduction

Photodetectors are one of the key components in many optoelectronic devices which facilitate the conversion of light into electric signals. Light, with a large spectral wavelength range from X-ray to IR, carries valuable information which needs to be detected fast and efficiently for further digital processing. Today, photodetectors have reached a mature technology level and comprise a huge market landscape including applications such as imaging, remote sensing, fibre-optic communication and spectroscopy among many others. Imaging has been a particularly thriving sector for years with smart-phones, automotive and medical applications (16B US$ by 2020 for CMOS image sensors) driving technological progress [1]. Therefore the ongoing search for new material systems and device architectures for a new generation of optoelectronics is not surprising. To open doors for new product designs, new photodetector systems should either outperform the existing state-of-the-art technology in terms of cost or performance or be on par with existing technologies while offering additional features, such as flexibility or transparency. In particular, flexible and wearable electronics hold great promise to become a tremendous new market [2]. 2D materials are considered a promising candidate for a new generation of low-power optoelectronics due to their flexible, thin and light-weight nature as

well as their remarkable optoelectronic properties. This chapter will briefly introduce state-of-the-art photodetector technology with vis-SWIR sensitivity and point out its strength and limitations. Then, the rising field of 2D materials is discussed in view of its potential application in flexible photodetectors. The chapter concludes with a point-by-point statement of the thesis objectives and organization.

1.1 State-of-the-art photodetector technology

Photodetectors are optoelectronic devices used to sense light by converting photons into electric charges. Its physical principle is based on the absorption of light, which generates a photocurrent or a photovoltage within the device that can be further processed by standard readout electronics. The efficiency of a photodetector depends on the optical absorption process, charge carrier separation and transport, and charge extraction into the electronic circuit system. A diverse range of semiconductors are used as photoactive materials in photodetectors, each having its advantages and disadvantages in view of fabrication complexity, stability and performance. Hence, before selecting the appropriate detector material or device architecture, many aspects of the desired application like wavelength range, sensitivity and speed have to be considered. Telecommunication, for instance, requires ultra-fast detectors for high information transmission rates, while imaging systems can tolerate lower speeds in order to have higher sensitivity detection of low light levels.

Photodetection in the visible. The use of silicon, with its indirect bandgap of 1.1 eV, is widespread in high-performance visible photodetectors. Two major technologies based on silicon diodes, charge coupled devices (CCD) and complementary metal-oxide-semiconductor (CMOS) sensors, have dominated the market for decades. Today, CMOS has the largest marketshare, as it became competitive with CCD cameras with the development of sophisticated processing techniques [3, 4]. CMOS image sensors with sensor arrays of millions of pixels achieve high image quality and provide compelling advantages over CCD in terms of speed and power consumption [5]. Apart from that, CMOS sensors have the advantage of being processed together with all circuitry functionality blocks on the same chip, benefiting from existing technological knowledge and simpler processing within the same CMOS Integrated Circuit production lines. The monolithic integration of image sensors with read-out and signal-processing electronics is crucial for high-volume production output at significantly lower costs. The growing area of smartphones is already dominated by CMOS imaging sensors, and forecasts predict annual growth

of the market value for fields such as smart-phones, automotive and medical application in future [1].

Yet, Si photodiodes possess some fundamental limitations which constrain their usage in certain applications. The performance of CMOS image sensors is limited by its noise, coming from the read-out circuit, and by its quantum efficiency (QE). Photodiodes can reach a maximum quantum efficiency of 100 %, meaning that in the ideal case only one electron can be extracted per incident photon. For imaging applications at extremely low light-intensity levels, however, a mechanism to create gain, i.e. several electrons per absorbed photon, is highly desired to overcome the noise-level floor of read-out electronics.

As a consequence, silicon avalanche photodiodes (APDs) were designed with a built-in amplification mechanism that generates gain of hundreds of electrons per absorbed photon. APDs are extremely sensitive photodetector systems reaching even single-photon sensitivity if operated in Geiger-mode. However, the strong signal enhancement in these diodes is only made possible by operating them at extremely large reverse biases of few hundred volts, which complicates their use as commercial, low-power image sensors. Another drawback of Si APDs is the high complexity of the fabrication processes, making it challenging to integrate them on the same chip with electronic circuits and therefore significantly increasing the manufacturing cost. New device designs are now developed to monolithically integrate APDs with CMOS, but the challenge of optimizing APD performance and compatibility of the high APD voltage operation with CMOS technology remains [6, 7].

Photodetection in the NIR/SWIR. To enable imaging beyond human vision, alternatives to silicon are needed as the bandgap of silicon only allows efficient detection up to 0.9 μm. Image sensors in the NIR/SWIR wavelength range currently employ III-V semiconductor compounds like indium gallium arsenide (InGaAs) and are used in a wide range of applications from optical communication to IR spectrometry. InGaAs detectors deliver fast speed and high sensitivity up to 1.7 μm with a possible extension to 2.5 μm, depending on the composition of the heterostructure [8].

InGaAs photodiodes suffer from similar limitations as silicon in view of its quantum efficiency and readout noise. In addition, they carry the burden of large fabrication cost due to complex epitaxy growth techniques under ultra-high vacuum conditions [9]. These growth methods are not compatible with standard manufacturing of silicon electronics, and complex hybrid integration methods like flip-chip bonding via indium bumps are required to integrate heterogenous InGaAs sensors

with current CMOS technology [10, 11]. Still, a huge consumer market exists for NIR/SWIR detection and a variety of applications such as night vision, security and surveillance systems, and automotive sensors could profit from the capability to sense beyond the visible. Under environmental conditions with low visibility like fog, haze, smoke and low light-levels at night time, the detection of wavelengths in the SWIR can overcome the shortcomings of Si-based technology [8]. However, current IR detector cameras, with costs of tens of thousands of dollars [8, 12], are still too expensive for commercial use in everyday applications. The need for new low-cost and sensitive detector systems in this spectral range drives current and future research on new photosensing systems.

1.2 Photodetectors based on 2D materials

Today, technological development is on the threshold of a very exciting new era, the era of flexible and wearable electronics. Future optoelectronic systems will have to fulfil many of the electronic, optical and mechanical functions required for flexible smart systems like smartphones, smartwatches, smartglasses, etc (see Figure 1.1(a)). The rapidly growing interest in flexible electronics is driving researchers and industry to find new material systems or to develop new device concepts with a high degree of flexibility, stretchability and even transparency. Despite its mature technology level, silicon faces limitations for application in flexible and transparent optoelectronics due to its indirect bandgap. An optically active region with rather large thickness in the order of microns is required to absorb incident light efficiently, making silicon detectors opaque, brittle and thus incompatible with flexible substrates. Polymers, organic materials, amorphous and metal oxide thin-film transistors form a large pool of potential material systems that are interesting for flexible electronics. Their low charge carrier mobility, however, make them suitable only for low-frequency electronic applications [13].

With the first isolation of monolayer graphene in 2004 [14], a new field of research was born: the field of two-dimensional (2D) materials. Graphene, a sheet of carbon atoms just one atomic layer thick, offers a vast variety of properties that are interesting for fundamental science and industry. Its high carrier mobility, mechanical flexibility, high transparency and constant optical absorption over a wide energy spectrum from UV to far IR are appealing for its implementation as an ultrathin photodetecting platform. Especially the latter is intriguing for optoelectronic technology and originates from the fact that graphene is a gapless material. Promising devices have been reported with high-speed performance in the GHz bandwidth, but with rather low responsivity in the range of mA/W due to low absorption and

short carrier lifetime in single layer sheets [15, 16]. Considerable effort has been devoted to increasing the absorption in graphene-based photodetectors by employing plasmonics [17, 18], integrating with waveguides [19, 20] or sensitizing with strong absorbing semiconducting materials [21–23]. A downside of the missing bandgap, however, is the large dark current when employed as a photodetector. High dark current is detrimental for several photodetector aspects such as noise and low power consumption. Additionally it makes the signal read-out process less efficient, as large dark currents saturate read-out electronics [24], calling for design of complex read-out schemes not typically used in current CMOS platforms.

With the advent of graphene, researchers expanded into other 2D materials, which share similar properties like the atomic thickness and flexibility, but also complement graphene with further functionalities. The group of semiconducting transition metal dichalcogenides (TMDCs) emerged as a promising candidate for both conventional semiconductor technology and flexible technology in view of its ultimate scalability down to the atomic level and the presence of bandgap. With decreasing layer thicknesses, quantum confinement effects come into play, leading to a sizeable optical absorption edge between 1-2 eV. The first photodetectors in the visible have been demonstrated on single-layer TMDCs with extension of sensitivity to the NIR for multilayer devices [9]. TMDC-based photodetectors can be operated at ultra-low dark currents achieved by the field-effect modulation of the channel into its depletion. This favorable condition for highly sensitive photodetection will be described in more detail in chapter 4.

The properties of semiconducting TMDCs complement semi-metallic graphene in many aspects and pave the way towards new functional device concepts based on a combination of 2D systems, also termed as Van der Vaals heterojunctions [25]. As depicted in Figure 1.1(b) an entire library of new 2D materials including graphene, TMDCs (MoS_2, WSe_2, etc.), boron nitride or Xenes (Silicene, Phosphorene) has been explored in recent years [25, 26]. The vertical stacking of a multitude of those 2D materials to heterostructures has provided new opportunities to achieve strong light-matter interactions [27] and to create innovative device concepts including p-n-diodes [28, 29], memories [30], tunnelling transistors [31] and many more.

Commercialization of flexible TMDC optoelectronics will require some open challenges, such as large volume manufacturing and its integration with flexible readout circuits, to be addressed. While most detector prototypes have been fabricated on brittle Si/SiO_2 substrates, the first electronic transistors have been demonstrated on soft polymeric and plastic substrates [32–34] with encouragingly high performance for bendable electronics. The majority of proof-of-concept devices, however, have

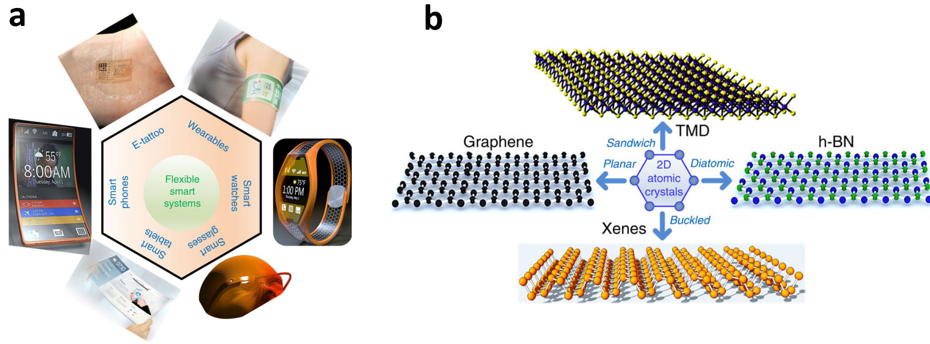

Figure 1.1: 2D material systems and flexible technology. (a) Four groups of heavily investigated 2D materials including graphene, TMDCs, boron nitride and Xenes. (b) Outlook on future technology and applications for flexible smart systems. Both Figures are adapted from [26]

been produced by scotch-tape exfoliation from single crystals. A crucial step towards realization in future photodetector technology will be the large-scale fabrication of high-quality, single-crystal TMDCs independent of the substrate. The viability of TMDC devices will thereby strongly depend on factors such as low cost, ease of fabrication and integrability with existing Si CMOS technology and flexible readout circuitry. Significant effort has been put in chemical vapor deposition (CVD), following the success of high-quality graphene. The self-organized growth mechanism in vapor-phase methods strongly depends on the substrate and temperature with best quality achieved at rather high temperatures of 500 - 1000 °C [35, 36]. Crystal defects from the growth process and contamination after the material transfer process are the biggest challenges to date [26]. Apart from these bottom-up techniques, liquid phase exfoliation of TMDCs in solution may turn out to be an interesting top-down procedure. The production of large quantities and mixtures of material systems would facilitate its use in flexible and light-sensitive spray coatings as well as printable electronics [37].

While large-scale manufacturing of TMDCs is still in its infancy, the rapid advances in graphene processing (e.g. roll-to-roll technique) have led to recent market penetration with the first graphene application in smartphone touchscreens [26]. The research on TMDC has so far largely profited from existing knowledge and experience on graphene. Likewise the technological maturity of graphene is expected to promote TMDCs for early commercialisation in the near future. The compatibility of 2D photodetector fabrication with existing low-cost CMOS manufacturing will play a key role in successful commercialization [38, 39].

2D materials such as graphene and TMDCs have great potential to create a

new generation of high-speed and highly sensitive photodetecting platforms. Their unique features such as light weight, bendability, transparency and shock-resistance will open a variety of applications in flexible cell phones, curved displays, electronic textiles and biomedical sensors.

1.3 Thesis objectives

The main goal of this thesis is the development of low-dimensional photodetector systems based on TMDCs with high sensitivity over a wide spectral range and the potential for flexible device concepts. The bandgap of TMDCs plays a crucial role in detector performance and is at the heart of this investigation. On the one hand, the bandgap is useful when TMDCs are implemented in a phototransistor device configuration, in which the dark current flow can be reduced by bringing the transistor to its off-state via field-effect modulation. On the other hand, the bandgap can govern the optical absorption efficiency and spectral selectivity in TMDCs depending on the number of layers. The direct bandgap of monolayer TMDCs provides with a high absorption coefficient, but the spectral sensitivity is limited to the visible and the absorption of light in absolute terms is small due to the atomically thin material body. With an increasing number of layers, the absorption onset of TMDCs can be extended into the NIR, but the overall absorption process is rather inefficient as the bandgap changes from direct to indirect. To overcome this absorption bottleneck, a novel method is developed to combine TMDCs with strongly absorbing colloidal quantum dots (QDs) to increase the absorption efficiency and introduce further spectral selectivity without compromising the flexible character of 2D TMDCs.

This research is focused on the development of first prototypes based on exfoliated semiconducting TMDC nanoflakes on rigid substrates such as Si/SiO_2 wafers, with the goal of gaining fundamental understanding of device functionality. From these findings, the potential for these devices to compete with state-of-the-art photodetectors and their application in large-scale photodetectors on bendable substrates is discussed. To reach this goal, the following issues are addressed within this work:

- First, the potential of plain MoS_2 phototransistors for visible light sensing is investigated. Reports of 2D TMDCs demonstrate encouraging performance in visible detection, although the reported results vary strongly due to different measurement environments [40–52]. The large surface-to-volume ratio of 2D materials and the impact of environment create instability in performance and are responsible for this large variety of results. To overcome this problem,

a simple device encapsulation scheme is developed and the impact of encapsulation on device performance is systematically studied. The objective is to further improve previously reported high detector performance and to maintain it even under harsh environmental conditions with this encapsulation technique. Finally fundamental limitations of plain TMDC phototransistors are identified and future prospects are discussed.

- The second goal is to improve the light-matter interaction of ultra-thin 2D photodetector systems and expand their spectral selectivity beyond the visible. Therefore a novel hybrid device architecture that combines 2D TMDCs with 0D colloidal quantum dots is used. The idea behind this hybrid strategy is to decouple the absorption process from the transport process, so that the device can profit from the strength of each material system. The employment of quantum dots with tunable absorption through control over their size expands the spectral selectivity and improves the devices absorption efficiency. The high mobility of TMDCs benefits efficient charge transport and gives them the potential to generate large photoconductive gain. The main scope is to study the impact of sensitizing QDs on the performance of TMDC phototransistors and to increase sensitivity compared to plain devices.

- Finally the optimization of hybrid-device performance is attempted with the aim to approach or even outperform state-of-the-art photodetector sensitivity. 2D materials react sensitively with surface modifications and the combination with other compounds can largely change and deteriorate their characteristic field-effect properties [53–57]. In nanotechnology the interface of devices often plays a crucial role. Especially for the studied hybrid devices, which consist of two low-dimensional nanomaterials, the interface has large potential to impact device performance. Careful interface engineering is applied and its impact on device operation is studied with a comparison to control devices with unprotected interface.

1.4 Thesis outline

The thesis is organized as follows:

Chapter 2 briefly introduces the fundamental theory of photodetectors. It shortly describes the different physical mechanisms which generate photoresponse and enable photodetection. The section will thereby focus on mechanism based on the quantum photoelectric effect, where absorbed photons create electron-hole pairs

and generate a photocurrent or photovoltage. Three different types of detectors are presented, the photoconductor, the photodiode and photo-field-effect-transistors (photo-FET). Finally all relevant figures of merit and standard terminology are described to facilitate the comparison of different photodetector types and to compare them with state-of-the-art detectors.

Chapter 3 presents the group of TMDCs with focus on MoS_2. It illustrates how layer thickness affects electronic structure and optical and electronic properties and points out optimized conditions for its application in the following chapters. The chapter briefly describes standard characterization methods used to identify layer thickness and quality as well as the device fabrication method used in this thesis. It concludes with the characterization of the electronic performance of TMDC field-effect transistors, which form the basis of the investigated photodetector systems.

Chapter 4 reports plain metal-TMDC-metal photodetectors in a transistor architecture. After summarizing and discussing previous work from literature, a possible solution to overcome existing limitations, such as the slow device speed, by encapsulating the detectors with a thin oxide layer is presented. The chapter presents device performance in air and under harsh conditions and illustrates significant performance improvement compared to previous work. Despite its remarkably high sensitivity, the sub-nanometer thick semiconducting channel yields limited absorption. Concluding this chapter, the challenges of 2D photodetectors are revisited.

Chapter 5 introduces a novel device concept for hybrid phototransistors. For the first time TMDC transistors sensitized with colloidal QDs are reported to tackle the issue of low quantum efficiency and spectral tunability/expansion in 2D systems. The synergy of strongly absorbing QDs with a high-mobility TMDC channel lead to higher performance compared to the plain MoS_2 reference. By making use of the QDs quantum size effect, the absorption onset is tuned throughout the vis-SWIR region and responsivity is increased by several orders of magnitude due to an effective gain mechanism. In particular, the role of the backgate voltage in controlling the device sensitivity is studied by changing the dark current flux and its corresponding noise.

In **Chapter 6** focus is placed on further development of hybrid TMDC-QD detectors by maintaining the initially high on/off ratio of TMDC FETs after QD deposition via interface engineering. In doing so, methods from previous chapters are employed to encapsulate the TMDC channel before QD deposition with large

bandgap semiconducting oxides such as TiO_2. This buffer-layer helps to maintain FET modulation as it passivates the high density of trap states created at the direct TMDC-QD interface. Through such control an enhancement of sensitivity by more than one order of magnitude, due to a strongly reduced noise floor, is demonstrated.

2

Photodetection theory

The large diversity of applications in our daily lives that rely on photodetecting technology requires photodetectors with distinct properties. The choice of an adequate photodetecting system depends on many factors such as its spectral selectivity, speed and sensitivity. While material properties determine the bandgap and spectral range that can be covered, the device architecture governs the mechanism behind the photosignal generation. The device design therefore has strong impact on other important performance parameters, such as speed or sensitivity. In the first part of this chapter, the most common photodetector types and their corresponding mechanism of photosignal generation are discussed. In the second part, all relevant terminology and figures of merit are defined.

2.1 Photodetection mechanism

Sensing of optical radiation can be divided into two classes: photodetectors and thermal detectors. Photodetectors are based on the quantum photoelectric effect, where incoming photons interact with the atomic lattice of the material and cause a change in conductance or generate a photocurrent or photovoltage. In thermal detectors, the absorbed photons produce heat, which can either change the resistance of the device or create a temperature gradient due to non-uniform heating and thereby generate photocurrent. As in graphene, both the photoelectric and the heat assisted mechanism have been reported for TMDC detectors [9]. Although thermal effects, i.e. the photo-thermoelectric or photo-bolometric effect, come into play under zero bias conditions, in this work the focus will lie exclusively on photoelectric effects as they dominate performance under applied bias voltage [58–60]. These include the photovoltaic and photoconducting effects.

Photoconductor. A photoconductor, in its most basic configuration, consists of a homogenous semiconductor slab with two ohmic metal contacts. When light of energy higher than the semiconductor bandgap is incident on the device, it induces a change of carrier density and increases conductivity by

$$\Delta\sigma = \Delta n q \mu \tag{2.1}$$

where σ is the conductivity, n the charge carrier density, q the elementary charge and μ the mobility. The generated electron-hole pairs are separated by an applied voltage and added to the dark current between electrodes. An important mechanism that often appears in photoconductors is the photoconductive gain, which depends on the ratio of the free carrier lifetime τ_{lt} to the transit time τ_{tr}. The transit time is the time span a free carrier needs to move from one electrode to the other and is defined as $\tau_{tr} = L^2/\mu V$, where μ is the mobility, L is the channel length and V_{DS} is the applied drain source bias. In a more descriptive picture, photoconductive gain is generated as soon as one photo-excited electron (hole) traverses the electrode spacing more than one time before recombination with a hole (electron). The most general expression for the gain is given by

$$G = \frac{\tau_{lt,n}}{\tau_{tr,n}} + \frac{\tau_{lt,p}}{\tau_{tr,p}} = (\tau_{lt,n}\,\mu_n + \tau_{lt,p}\,\mu_p)\,\frac{V_{DS}}{L^2} \tag{2.2}$$

Equation 2.2 suggests that gain can be of quite different origin. If trapping effects are neglected, a difference of mobility between electrons and holes can generate gain. If for simplicity only ohmic contacts for electrons are assumed, the lifetime of both carrier types is then equal to the transit time of the holes. The gain is then given by $\tau_{tr,p}/\tau_{tr,n}$. A much lower mobility of holes would therefore produce gain: to maintain the electrostatic equilibrium inside the semiconducting slab, the extracted electrons replenish the channel through the ohmic contact and recirculate the channel multiple times until the hole is extracted or recombined.

In a more realistic picture, semiconducting systems contain a certain amount of trap states within the bandgap, which can capture and localize one charge carrier type (see Fig. 2.1 (a)). If holes are trapped and ohmic contacts are formed for electrons, gain is produced until the captured holes recombine with freely moving electrons. In this case the lifetime of electrons is governed by the trapping time of holes and the gain is defined by $\tau_{lt,p}/\tau_{tr,n}$. This effect is often referred to as the photogating effect, where upon photoexcitation trapped carriers act as a local gate that induces charge carriers into the channel. The amount of traps and their corresponding capturing cross section for each carrier type vary for each material and depend on factors such as defects, impurities or surface states. Especially low dimensional systems with a large surface-to-volume ratios, such as TMDCs and QDs, possess a rather high density of trap states created by adsorbates or oxidization. It is noteworthy that the gain mechanism depends also on the quality of ohmic contacts formed for the circulating charge carrier type. Schottky-type contacts can strongly impede efficient charge replenishment and reduce photoconductive gain.

Photodiodes. Although it is not the focus of this work, a brief introduction into the working principle of photodiodes, which are based on the photovoltaic effect, is given. Photodiodes typically have vertical device configuration, either forming a p-n-junction between oppositely doped semiconductors (as illustrated in Fig. 2.1 (b)) or a Schottky-junction between a semiconductor and one of the metal electrodes. The junction leads to charge carrier separation after the excitation process and electrons and holes drift in different directions towards the electrodes driven by the built-in electric field at the interface. The response time of diodes is determined by the transit time of carriers to their corresponding electrode, leading to high-bandwidth operation in high carrier mobility semiconductors. At zero bias voltage, photodiodes operate at ultra-low dark currents with low power dissipation. However, photodiodes are generally operated at reverse bias, which increases the depletion region. The capacitance of the junction is thereby reduced and the charge carriers can be extracted on an even faster time scale. The signal strength detected

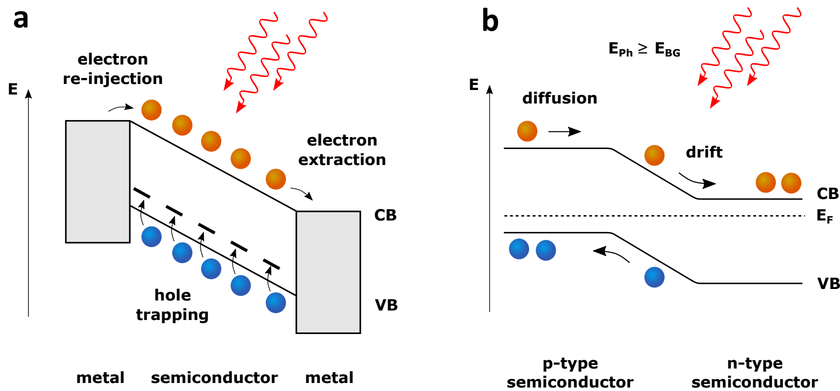

Figure 2.1: Photoconducting and photovoltaic mechnism. (a) Schematic to describe the photoconducting mechansim. After photo excitation of electron-hole pairs, holes (electrons) get trapped in localized states close to the valence band (conduction band) while the opposite carriers circulate between electrodes driven by the applied electric field. If the hole lifetime is longer than the electron transit time, photoconductive gain is produced yielding several electrons per absorbed photon. Ideal circulation conditions are reached for ohmic contacts to electrons. (b) The photovoltaic mechanism is depicted here on a p-n-junction. When p-type and n-type semiconductors are brought into contact, charge carriers flow until the Fermi level E_F is in equilibrium leading to band bending at the interface. Upon light exposure, the created electrons (orange) and holes(blue) are separated by the built-in field at the interface and drift in opposite directions generating a photovoltage.

in diodes is given by the quantum efficiency. As charge carriers are separated by a built-in field at the junction, the device can at its best produce one electron-hole pair per absorbed photon. The quantum efficiency is therefore always lower than 100 %, unless a gain mechanism is inherent. At strong reverse bias the phenomenon of impact ionization comes into play and excited charge carriers can be multiplied by factors of 10-1000 before extraction at the electrode. This mechanism is employed in APDs, which are highly sensitive down to single photon events and provide fast operation, rendering them one of the most efficient and sensitive photodetecting systems to date.

Phototransistor. There are different kinds of phototransistor device designs. The most common design is based on ordinary bi-polar transistors where the current amplification is controlled by the incidence of light. In this work the focus lies on unipolar devices, which are operated as standard field-effect-transistors (FETs). The device configuration is similar to lateral photoconductors with a metal-semiconductor-metal architecture forming the source and drain electrodes. While photodiodes and photoconductors are two terminal devices, an additional third electrode, the gate contact, is present in phototransistors. The gate electrode is insulated from the channel by a thin dielectric film. Under dark conditions the applied gate voltage changes the carrier density inside the channel, hence controlling the electrical conductivity between source and drain. Under illumination the channel conductance can be additionally altered by changing the carrier density after absorption of light, as is the case in photoconductors. The two features combined make this type of phototransistor, also referred to as photo-FET, a promising system for high signal-to-noise ratio photodetection. While the gate voltage can be used to electronically switch off the dark conductivity and thereby minimize noise, the incident light enables channel conductance.

The device concept of photo-FETs, based on gate voltage controlled photoconductivity, gets particularly interesting when combined with the photovoltaic effect of diodes. This can be realized by sensitizing the channel material with a semiconductor of opposite doping polarity to create a vertical p-n-junction, as shown in Figure 2.2(a). The built-in field between the channel and the sensitizer efficiently separates photo-excited electron-hole pairs and injects one carrier into the channel, where it can profit from strong signal amplification. The electric field of the trapped carrier remaining in the sensitizing material changes the Fermi level and induces multiple carriers of the opposite sign into the channel, based on the earlier discussed photogating mechanism. Thus, the vertically occurring absorption process is decoupled from lateral charge carrier transport and signal amplification.

The photogating effect in plain and sensitized photo-FETs can be identified by a vertical shift of the I_{DS}-V_G transfer curve under illumination. In the case of a plain photo-FET, one carrier type of the excited electron-hole pair is captured in charge traps within the channel or in interface/surface traps (adsorbates, molecules). In sensitized photo-FETs, the absorption takes place in the sensitizing film, where one charge carrier remains trapped while the other moves into the conducting channel. In both cases, the trapped carrier gates the FET-channel, and the opposite charge carrier recirculates many times between source and drain. Depending on the trapped charge carrier type, the photogate-doping under light can either be n-type or p-type as depicted in Figure 2.2(b) for a typical n-type photo-FET.

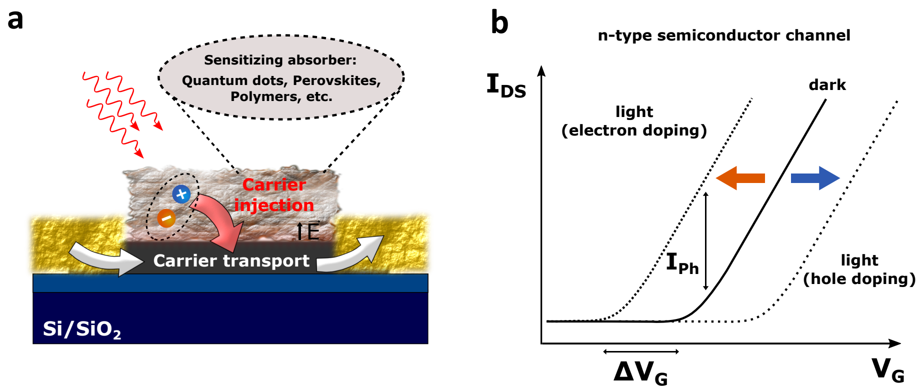

Figure 2.2: Sensitized photo-FET and light induced shift. (a) Illustration of a sensitized photo-FET. The sensitizer ideally consists of a strong absorbing material like QDs, perovskites, polymers, etc. The vertically occurring absorption and charge-separation process at the sensitizer/channel junction (red arrow) is decoupled from lateral charge carrier transport and signal amplification through the FET-channel (white arrows). (b) Transfer curves I_{DS}-V_G of a n-type photo-FET under dark (solid line) and illuminated (dashed line) conditions. Depending on the trapped charge carrier type after light excitation, the photogate-doping can either be n-type (orange arrow) or p-type (blue arrow) and shift the curve correspondingly.

The absorption of light in these hybrid photo-FETs is now determined by the sensitizing semiconductor, adding another degree of freedom for instance in choice of spectral selectivity. Especially 2D material-based photo-FETs can benefit from this approach. They usually offer remarkable electronic properties such as high mobility, a fundamental prerequisite for high gain generation (see Eq. 2.2), but they suffer from low light absorption due to their atomically thin body. The synergy of strong absorbing sensitizers (of any kind: colloidal quantum dots, perovskites, polymers, etc.) with high mobility channel materials lead to a new device design, which is highly promising for sensitive photodetection.

2.2 Figures of merit

Standard terminology and figures of merit are important for describing and comparing distinct photodetecting systems and deciding application. In this section the most important performance parameters are summarized; these are used throughout this thesis.

2.2.1 Responsivity, quantum efficiency and gain

The fundamental process behind photodetection is absorption of light. Responsivity R, a measure of output current per incoming optical power, describes how a detector system responds to illumination. The most general expression for responsivity is

$$R = \frac{I_{Ph}}{P_{In}} = QE\,\frac{q\lambda}{hc}\,\frac{1}{\sqrt{1+(2\pi f\tau)^2}}\,G \tag{2.3}$$

where I_{Ph} is the photocurrent, P_{In} is the incident light power, QE is the quantum efficiency, q is the electron charge, λ the wavelength, h is Plancks constant, c is the speed of light, f is the modulation frequency, τ the time constant and G the photoconductive gain.

The response of a detector to light depends primarily on the conversion efficiency of photon flux into electron flux, known as the quantum efficiency. The quantum efficiency typically takes into account all kind of external losses such as reflection and scattering and is often called external quantum efficiency (EQE). It is defined as the ratio of extracted electrons to incident photons, a value between 0 and 100 % unless an internal gain mechanism is present. In photodiodes the gain is limited to unity ($G = 1$) and charge extraction happens on extremely short time scales. The responsivity according to Eq. 2.3 is then solely determined by the quantum efficiency. For instance, in the ideal case of 100 % conversion efficiency at a wavelength of 630 nm, the responsivity is 0.5 A/W.

In photoconducting systems, the gain mechanism can be inherent, as discussed in the previous section. In the most common case, one carrier type is trapped and the other is free to traverse the channel, generating gain defined by $\tau_{lifetime}/\tau_{transit}$. This can lead to a large responsivity that is orders of magnitude higher than for photodiodes. Photoconductors with large gain usually show rather slow response times as described by the so called gain-bandwidth trade-off. Responsivity depends on the optical modulation frequency, and the 3 dB-bandwidth of a detector is defined

as the frequency at which responsivity drops to $1/\sqrt{2}$ of its value under continuous illumination. Since the response time constant and the photoconductive gain are dominated by the lifetime of trapped carriers, increasing gain decreases the 3 dB bandwidth. This trade-off must be considered when designing detectors for specific applications. For instance, in imaging and video capture applications where sensitivity has priority over detector speed, photoconductors with high gain are desirable, but also response times in the milliseconds range, beyond the limit of human vision perception, are required [12].

2.2.2 Dark current, noise and detectivity

The performance of a photodetector is not yet fully described by its response to optical illumination. The response also has to be distinguished from the background signal under dark conditions, the detector noise. The magnitude of dark current between the electrodes plays an important role, as it can be associated with the amount of noise in a device. As a consequence, one of the main goals in photodetection is to achieve dark currents as low as possible, which apart from low noise will also favor operation with low power consumption.

There are three major noise sources in photoconductors: the generation-recombination (G-R) noise, Johnson noise and low-frequency (1/f) noise [61]. Figure 2.3 shows a

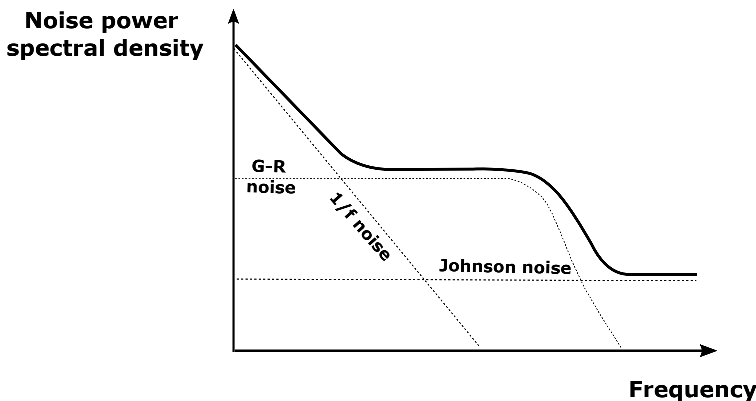

Figure 2.3: Noise power spectral density as a function of frequency. The theoretical noise spectral density describes how the three noise components contribute to the frequency dependent noise curve: At low frequency the 1/f noise dominates, in the mid-frequency range the G-R noise gets stronger and at large frequency the noise is associated with Johnson noise. Redrawn from [61]

schematic of a typical noise spectrum of photoconductors as a function of electrical frequency. At low frequency the predominant noise component is 1/f noise. As many

photoconductors or phototransistors possess gain and relatively long time constants, the device bandwidth is often limited to low frequency operation of kHz or less and therefore falls into the range of low-frequency noise. The origin of 1/f noise is still not well understood and often assigned to contact effects such as non-ohmic contacts. This suggests that careful control of contact fabrication could minimize their impact on overall noise. Another effect that adds 1/f noise is the presence of surface traps. The different lifetimes of these trap states disturb the current flow and generate a non-white noise spectrum. Fast detectors with moderate gain can circumvent low frequency noise by operating the system at high frequency with lock-in photodetection. At mid-frequencies the G-R noise becomes dominant. G-R noise appears in the form of fluctuation in conductivity due to a random number of free carriers. The free carriers are generated via background irradiance or thermal excitation and have varying lifetimes due to trapping and de-trapping events. G-R noise is important in photoconductors with gain and can be reduced by minimizing the detector volume. The G-R roll off frequency is determined by the carrier lifetime and above that, the frequency-independent constant white-noise spectrum is dominant. In single crystalline photoconductors this is given by Johnson noise, a noise component that is inherent to all resistive elements and stems from fluctuation in current flow caused by thermal motion of carriers.

Also, shot-noise is a major white-noise component in photodiodes and appears when dc-current has to cross a potential barrier. In more mathematical terms, this noise becomes important as soon as the number of flowing electrons is small enough that uncertainties due to poisson distribution cannot be neglected. Shot noise does not play a role when current flows through an ideal resistor as in single crystalline photoconductors, but can be present in polycrystalline photoconductors or phototransistors where current flow is interrupted by potential barriers. The shot-noise expression is given by

$$i_{SN} = \sqrt{2\,q\,I_{dark}\,B} \tag{2.4}$$

where q is the elementary charge, I_{dark} is the dark current and B is the bandwidth. Shot noise is often used to estimate a lower limit of noise and to evaluate the potential upper limit of sensitivity in detecting systems.

The ultimate figure of merit to describe sensitivity of photodetectors includes both the response to light and the noise floor. The higher the signal-to-noise (SNR) ratio, the easier it is to detect the light signal. The lowest detectable power, when

SNR = 1, defines the sensitivity limit of the detector and is called noise-equivalent power NEP, defined as

$$NEP = \frac{i_N}{R} \tag{2.5}$$

where R is the responsivity and i_N the noise current. The unit of NEP is Watts, being a direct of measure of the lowest distinguishable power. However, NEP depends on many parameters that have to be taken into account and specified, such as detector area A, electrical bandwidth B and modulation frequency f. To facilitate the direct comparison between different detector architectures independent of area and bandwidth, R.C. Jones defined a new term in 1953 called normalized detectivity D^*, given by

$$D^* = \frac{\sqrt{A\,B}}{NEP} = \frac{R\sqrt{A\,B}}{i_N} \tag{2.6}$$

The units of D^* are $cm\sqrt{Hz}/W$ = Jones. The detectivity D^* still depends on certain measurement conditions such as bias voltage, temperature and modulation frequency, which have to be specified for comparison with other systems. State-of-the-art detectors such as silicon or InGaAs diodes demonstrate detectivities on the order of $10^{12} - 10^{13}$ Jones at room temperature.

3

Properties and characterization of 2D TMDCs

This chapter provides some basic background information about structural, optical and electronic properties of transition metal dichalcogendides (TMDCs), focusing on molybdenum disulfide (MoS_2), and correlates them with their dependence on the number of layers. It also describes the fabrication method for the phototransistor devices developed in this thesis and covers the most common characterization techniques used to determine film thickness and quality. Finally the electronic properties of MoS_2-based FETs are presented and their impact on photodetector performance is discussed.

3.1 Synthesis and electronic structure

After the experimental discovery of graphene in 2004, the field has experienced rapid progress and many promising applications as radio-frequency electronics, transparent electrodes and numerous kinds of sensors have been demonstrated. Along with its success in certain areas, limitations of its use in other fields such as digital electronics have emerged due to the missing bandgap. The extraordinary properties of graphene, however, have aroused curiosity and have led to the discovery of other 2D systems.

The transition metal dichalcogendides form a class of semiconducting materials with the general chemical formular MX_2, where M comprises a transition metal element (for instance Mo, W, Hf, Ti, Zr, Nb,V, Ta, etc.) and X a chalcogen atom (S, Se, Te). The TMDCs form layered structures, where one layer consists of a plane of metal atoms lying between 2 planes of chalcogen atoms, thus forming a sandwiched X-M-X structure (see Figure 3.1(a)). While the atoms within a plane are bound together by strong covalent bonds, adjacent layers are only weakly coupled by Van-der Waals forces.

Molybdenum disulfide, the primary material throughout this work, appears in its thermodynamically stable form (the 2H-phase) with hexagonal symmetry with trigonal prismatic coordination of metal atoms. In the 2H-phase, MoS_2 shows semiconducting properties, but a change in crystal structure to the metastable 1T-phase can render the material metallic. The weak bonding of stacked layers in TMDCs allows isolation of extremely thin material slabs down to a single layer from its bulk material. Materials such as MoS_2, WS_2, $MoSe_2$ and WSe_2 retain stability down to the monolayer form and interestingly many optical and electronic properties depend on its number of layers.

The most intriguing change is the transition from indirect bandgap (1.2 eV) in bulk form to direct bandgap (1.8 eV) in monolayer form. From density functional theory (DFT) calculations, it is evident that the change of electronic structure is due to quantum confinement effects. This leads to a change in hybridization between p_z-orbitals on sulfur atoms and d-orbitals on molybdenum atoms, which mainly affects conduction band states at the Γ-point. In bulk form, a clear indirect bandgap can be observed at the Γ-point and its bandgap energy continually increases with decreasing slab thickness. Figure 3.1(b) shows that in the limit of a monolayer film, the indirect bandgap is larger than the direct exciton transition at the K-point, which stays widely unaffected by the change of thickness [62–64]. This transition to a direct bandgap semiconductor has important implications on optoelectronic

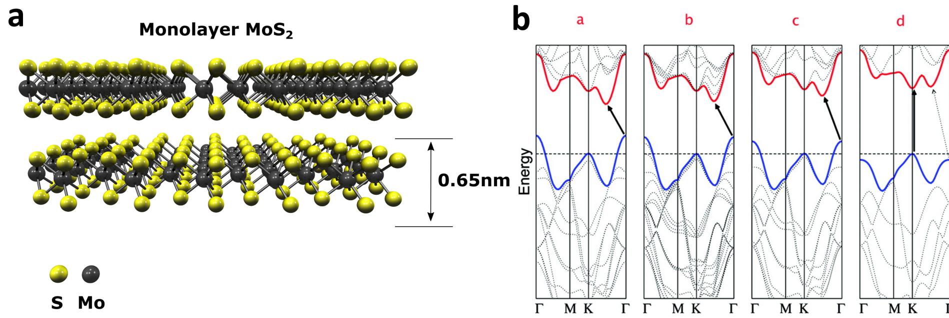

Figure 3.1: MoS_2 structure and bandmodel. (a) Schematic of two separated MoS_2 monolayers with a thickness of 0.65 nm. MoS_2 possess a layered structure, where a plane of molybdenum atoms is sandwiched between 2 planes of sulfur atoms, forming a S-Mo-S structure. (b) Calculated bandstructures for MoS_2 with different thickness: (a) bulk (b) 4 layers (c) 2 layers (d) 1 layer. In its bulk form, MoS_2 is an indirect semiconductor with an indirect transition of 1.2 eV at the Γ-point. As the number of layers decreases, the indirect bandgap increases and eventually becomes larger than the optical direct bandgap situated at the K-point in the monolayer limit. Figure (b) is adapted from [62]

device design. Photons with energy higher than the bandgap can efficiently be absorbed and emitted. For application in light emitting devices, monolayer TMDCs are therefore able to achieve significantly higher quantum yield than bilayer and bulk devices [63].

3.2 Mechanical cleavage and device fabrication

The weak interlayer coupling through Van-der Waals forces enables the isolation of monolayer and few-layer TMDCs using many different techniques. The easiest method is based on micromechanical exfoliation with scotch tape, first demonstrated by Geim and Novoselov on graphene [14]. Especially for naturally occurring crystals such as MoS_2, this makes high-quality 2D materials accessible to many research groups around the world, and rapid progress has been made on prototype development of various electronic devices. To mechanically cleave MoS_2, a small piece of single crystalline MoS_2 is enveloped several times with tape and peeled off repeatedly until sufficiently thin areas of MoS_2 are left over on the tape. These thin flakes are finally carefully dry-transferred onto Si/SiO_2 substrates. Despite the usage of standard scotch tape in first attempts, the method further developed to achieve large flakes over several tens of microns in diameter by using viscoelastic polydimethylsiloxane (PDMS) [65].

After the localization of high-quality nanoflakes (as will be explained in section 3.3), metal contacts are fabricated by standard lithography techniques. Two

methods, electron beam lithography (EBL) and laser writer lithography (LWL), have been applied with no obvious difference in device performance. While the throughput of LWL is much larger than in EBL, with LWL the smallest possible FET channel length is limited to 1 - 2 μm, whereas EBL can reach far sub-micron resolution. Various contact metals such as Au, Ti, Pd, Ag and Al have been tested to optimize FET performance. The best contacts have been achieved with Au or the combination Ti/Au, where Ti with thickness of 1 - 2 nm serves as an adhesion layer. The devices were then annealed in ultra-high vacuum for several hours at 150 °C to reduce contact resistance and remove adsorbates and resist residues.

3.3 Characterization techniques: AFM and Raman

There are various methods to localize nanoflakes of TMDCs and identify their thickness after transfer onto the desired substrate. The most critical and first evaluation is the layer thickness and flake quality, since exfoliation can often lead to wrinkles and cracks.

The left column of Figure 3.2 shows microscope images of a couple of MoS_2 flakes with thickness ranging from 1 - 5 layers on highly doped p-type silicon with 285 nm of SiO_2. Ideally, the oxide thickness should be around 90 nm or 285 nm to ensure optimized contrast for flake thickness recognition under the microscope. The thickness of thin few-layer flakes can be roughly estimated with the bare eye, although atomic force microscopy with sub-nm resolution is a reliable technique to determine the accurate number of layers. A layer thickness of 0.6 - 0.7 nm for single-layer MoS_2 is measured, in good agreement with values reported in literature [37]. The slight variation between devices may stem from substrate surface roughness and possible contamination. The two centered columns of Figure 3.2 demonstrate AFM images and step height profiles for different flake thicknesses. Exfoliated thicker films always show an integer multiple of the single layer thickness, demonstrating clean and uniform cleavage between layers. Apart from layer thickness control, AFM measurements also reveal valuable information about flake cleanliness and uniformity.

Micro-Raman spectroscopy is another convenient and powerful tool for accurate identification of the number of layers in 2D material research. The structural changes by thinning down bulk MoS_2 to its monolayer limit influence its vibrational spectrum and reduce the distance between the two characteristic peaks of the raman spectrum (see right column of Figure 3.2). Out of four known phonon modes in bulk 2H-MoS_2, only the E^1_{2G} and A_{1G} modes can be detected in few layer MoS_2 [66]. Figure

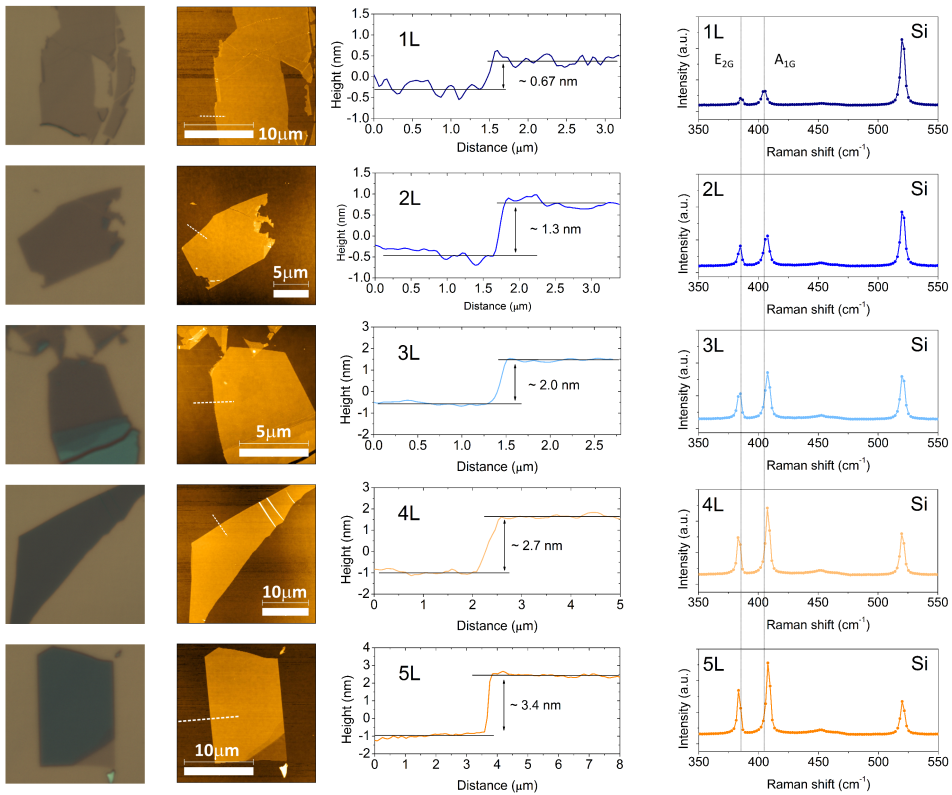

Figure 3.2: Characterization techniques: Microscopy, AFM and Raman. Results of standard characterization for MoS_2 flakes with different thickness ranging from 1 layer (top) to 5 layer (bottom). From left to right: captured microscopy images, AFM images, AFM height profile and Raman spectra around the characteristic phonon modes.

3.3(a) presents the two phonon modes and their atomic displacements for two layers of MoS_2. The E^1_{2G} phonon corresponds to a strong in-plane vibrational mode with spectral appearance around 386 cm^{-1} for monoloayer MoS_2. The A_{1G} mode originates from an out-of-plane mode and peaks around 405 cm^{-1}. With increasing flake thickness, E^1_{2G} red shifts and A_{1G} blue shifts, and both slowly approach their bulk phonon modes for flake thicknesses of more than 5 layers [66]. Following a classical model for coupled harmonic oscillators, an increase (blue shift) in both peak frequencies would have been expected due stronger restoring forces by adjacent planes. However, theoretical DFT calculations have revealed that neighboring layers of MoS_2 enhance the dielectric screening of long-range coloumb interactions, resulting in a decrease in the E^1_{2G} frequency [67]. Although the reported peak positions vary and depend on factors like temperature and the substrate [68, 69], the difference between the peaks of the two modes is a precise diagnostic tool for determination of the number of layers as depicted in Figure 3.3(b). The frequency difference has been correlated with AFM data to calibrate the Raman system on the used substrates. In agreement with literature, a striking difference is noticed for the first 1-4 layers. This difference decreases with increasing thickness, thus limiting its accuracy for thicker flakes.

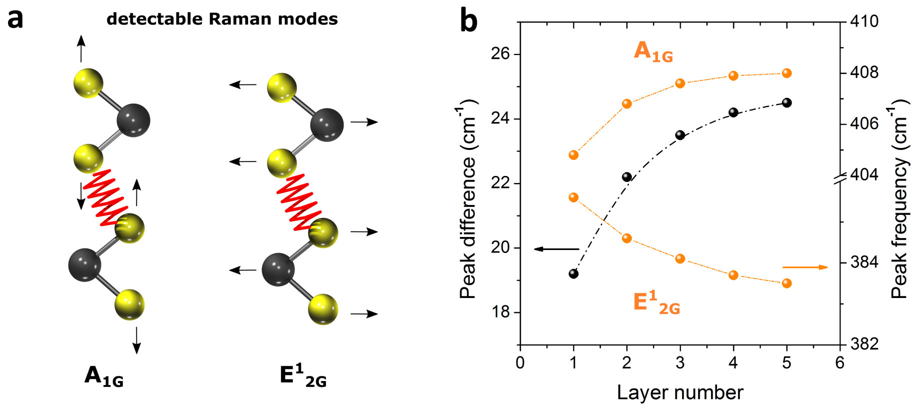

Figure 3.3: Few layer MoS_2 raman modes. (a) Schematic of the two characteristic and detectable raman modes, E^1_{2G} and A_{1G}, of few-layer MoS_2. The atomic displacement is affected by neighboring layers, leading to a thickness dependence of the raman spectrum. (b) Peak frequency and frequency difference between the characteristic raman modes for 1 - 5 layers. Extracting the difference is an accurate tool to estimate the number of layers for few-layer MoS_2 flakes.

Apart from AFM and Raman, additional reliable methods like the measurement of photoluminescence spectra offer insight into the quality and number of layers of the 2D sample under investigation. The continuous change in the band structure

with decreasing layer thickness has a strong impact on the quantum yield and shifts the peak energy of emitted photons, which can be used to distinguish between flakes of different layer thicknesses. The photoluminescence quantum efficiency of freestanding monolayer MoS_2 has been reported to be more than 4 orders of magnitude larger than in the bulk and a clear difference in the counts can already be observed between mono- and bilayers [63].

3.4 Transport properties of MoS_2

Ordinary FETs such as the widely used silicon-based MOSFET consist of a doped semiconducting body with oppositely highly doped contact regions to form a p-n junction within the channel. The degenerately doped n++ or p++ contact region, on which the metal is finally deposited, is thus just a highly conducting version of the same material as the channel and provides high quality contacts and low contact resistance. A third terminal, the gate electrode, is separated from the channel by a dielectric film and is used to electrostatically modify channel conductance. The channel conductance for this device concept is unipolar and determined by the channels' doping polarity.

In low-dimensional channel FETs, such as 1D carbon nanotubes or 2D TMDCs, the doped contact regions are substituted by metal electrodes. The direct contact of metal electrodes with the channel material often forms significant Schottky-barriers. These devices are therefore termed Schottky-MOSFET [70, 71]. The most commonly used device concept applies a global backgate, where the heavily doped silicon substrate provides the gate-terminal and its oxide serves as the dielectric layer. A microscopy image of a typical fabricated device is shown in Figure 3.4(a), and a schematic of the device design in Figure 3.4(b). The channel modulation of Schottky-MOSFETs is primarily controlled by changes in contact resistance rather than channel conductance. The alignment of the metal work-function with the conduction or valence band is therefore crucial for n-polarity or p-polarity, respectively. At a small enough bandgap even ambipolar device characteristic is possible with effective electrostatic gate control [72].

Figure 3.4(c) plots the linear and logarithmic (inset) modulation curves I_{DS}-V_G for MoS_2 FETs with exactly the same dimensions (width and length), Ti/Au contacts, and channel thicknesses varying from 1 to 4 layers. All devices possess clear n-type polarity and large on/off ratios of 10^6 - 10^7 for an applied electric field of $0.2\,V/\mu m$. It is noteworthy that the off-currents in the depletion regime are limited to few pA by the measurement system. These values correspond to few hundreds of

fA/μm, but are expected to be as low as 25 fA/μm [73], thereby further approaching the theoretically predicted on/off ratio of 10^{10} [74].

The n-type doping of MoS_2 is believed to stem from donor states introduced by sulfur vacancies [75, 76]. Titanium is theoretically predicted to form ideal ohmic contact for efficient electron injection in MoS_2 [77]. However even large work function metals such as platinum were reported to demonstrate n-type polarity with large contact resistance R_C due to Fermi level pinning at the semiconductor-metal interface [78]. For Mo-based TMDCs the pinning happens rather close to the conduction band, whereas for W-based TMDCs the E_F is pinned closer to the midgap leading to ambipolar behavior [79].The large R_C is one of the main obstacles for TMDC devices. Various techniques such as Li intercalation [80], degenerate doping of contact areas [55], global channel doping with chloride [81], the use of low work-function Scandium contacts [78] or the use of graphene contacts [82, 83] have been proposed to lower Schottky-barriers and R_C.

With increasing number of layers, more pronounced n-type doping and higher mobility is observed. These effects are indicated by a shift in the threshold-voltage to more negative V_G and an increase in the slope dI_{DS}/dV_G, respectively. Due to the higher density of states of few-layer MoS_2, a lower R_C and higher conductance is achieved for increasing film thickness [84]. The increased doping and mobility with increased thickness can also be explained by screening effects of charged impurities at the MoS_2/oxide interface [85, 86]. Moreover, since all measurements are performed in an ambient environment, this behavior may also be attributed to effects of atmospheric adsorbates such as H_2O and O_2 on the surface. These adsorbates are known to withdraw electrons from the channel and their influence is stronger for thinner channels. Apart from doping, gaseous adsorbates also significantly impact mobility and hysteresis, as demonstrated in more detail in chapter 4.

The field-effect mobility is approximated for measurements with a two-terminal device configuration by extracting the slope in the linear regime (for low bias voltage V_{DS}). Following conventional MOSFET theory, the field effect mobility μ_{FE} is given by

$$\mu_{FE} = \frac{dI_{DS}}{dV_G} \frac{L}{W\, C_{ox}\, V_{DS}} \tag{3.1}$$

where I_{DS} is the drain current, V_G is the backgate voltage, W is the channel width, L is the channel length, C_{ox} is the capacitance and V_{DS} is the bias voltage. This

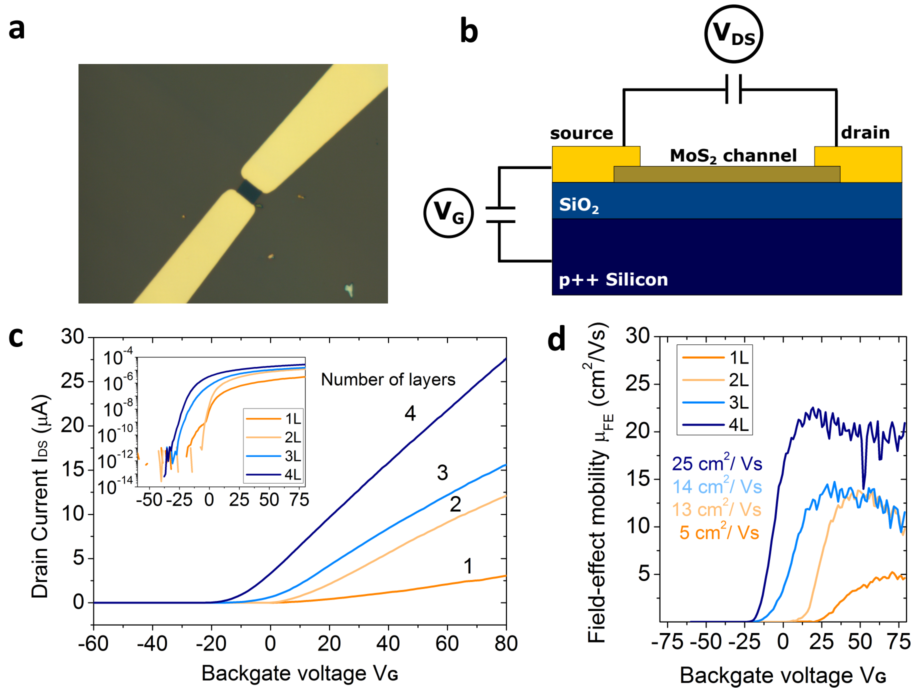

Figure 3.4: Thickness-depedent MoS_2-FET performance. (a) Microscopy image of a fabricated few-layer MoS_2 device contacted with Ti/Au. (b) Schematic of typical MoS_2-FET architecture. (c) Linear plot of the I_{DS}-V_G modulation curves for 1 - 4 layers thick MoS_2-FETs with equal channel dimensions. The inset shows the same graph on a logarithmic scale to visualize the large on/off ratios exceeding 10^6. $V_{DS} = 1V$. (d) Field-effect mobility for the 4 devices. Note that the correct value of μ_{FE} has to be extracted in the linear regime and at the maximum of the curves, where the modulation from (c) has its maximum slope. $V_{DS} = 0.1\,V$.

approximation is often used to estimate mobility, albeit underestimating real mobility values for Schottky-MOSFETs, where contact resistance has to be taken into account. The mobility can be more precisely determined by 4-terminal measurements in the Hall configuration, in which the electrode geometry circumvents the impact of contact resistance.

In this work, two-terminal measurements are performed to estimate μ_{FE}, and the extracted values for different number of layers agree well with literature [86]. Figure 3.4(d) plots the calculated 2-terminal mobility (from equation 3.1) versus V_G, and helps to identify the linear regime where field effect mobility saturates. A clear trend of increasing mobility with increasing layer thickness is observed, endorsing most experimental findings where mobility increases up to an ideal thickness around 10 nm. Afterwards the value drops with additional layers due to vertical access resistance from the electrode to the established electron channel at the oxide interface [78,87].

Although mobility is of paramount importance for photodetection, the focus of this thesis is not on the improvement of mobility. Yet, its improvement remains a puzzling task in the research community and will determine the future implementation of TMDCs in commercial applications. Despite theoretical prediction of phonon-limited mobilities up to 410 cm^2/Vs at room temperature [88], the best single layer MoS_2 mobilities reported to date still remain below 100 cm^2/Vs. A common assumption is the impact of charged impurities at the MoS_2/oxide interface and defects such as sulphur vacancies [86,89]. Fully encapsulated MoS_2 films sandwiched between boron nitride layers, have recently been demonstrated with record low-temperature mobilities of 10^3 - 10^4 cm^2/Vs for 1-6 layers, suggesting effective suppression of phonon- and impurity-scattering. However, the strongly reduced room temperature mobility of 40 - 120 cm^2/Vs leaves plenty of room for further improvement [83].

For the investigated phototransistors, some of the discussed FET performance parameters play an important role:

- **Low off-state current.** The ability to implement electrostatic control over conductance by applying a gate voltage is the major strength of the investigated phototransistors. Large on/off ratios together with low off-current operation in the device depletion regime can provide extremely low noise operation and are fundamental for high signal-to-noise output. The low dark current is also important in view of low power consumption and application in flexible and wearable devices. As the density-of-states in MoS_2 decreases

with thinner film thickness, monolayer devices are in favor as they carry much lower dark current.

- **Mobility.** In photodetectors, mobility is one of the most important material parameters, as it strongly influences the ability to extract photo-excited charge carriers from the semiconductor and determines the speed in photodiodes and the gain in photoconductors (phototransistors). In chapter 2, equation 2.2 describes the linear dependence of gain on mobility. The sensitivity of the investigated phototransistors is based on the photoconductive gain and a high mobility is therefore imperative for high detector performance. Moreover the temporal response of detectors to light requires fast carrier transport, and high gain-bandwidth products can only be reached with sufficiently high mobilities. In MoS_2, the largest mobility has been demonstrated in relatively thick films of around 10 nm. Low dark current and high mobility are both desired but competing features and therefore an appropriate compromise has to be reached depending on application.

- **Contact resistance.** Large schottky-barriers at the metal-semiconductor interface lead to high contact resistance and prevent efficient electron injection into the MoS_2 channel. It therefore hampers the charge recirculation through the MoS_2 channel and decreases the photoconductive gain. Apart from that and as discussed in chapter 2, the major noise source of the investigated phototransistors is 1/f noise, which also depends on R_c. Here again a trade-off exists, as thicker MoS_2 films usually possess lower contact resistances [84].

4

Two-dimensional TMDC phototransistors

Semiconducting, two-dimensional MoS_2 is considered a promising material for highly sensitive photodetection with potential for flexible applications because of its favorable bandgap and atomically thin profile. However, reported photodetectors to date show significant variation in performance [40–52]. Owing to the large surface-to-volume ratio of 2D materials, environmental adsorbates have a detrimental and uncontrollable impact on photodetecting devices. Herein, viable routes are sought to control these effects by protecting the devices from the atmosphere. In this chapter, highly stable, and high-performance monolayer and bilayer MoS_2 photodetectors encapsulated with atomic-layer-deposited (ALD) hafnium oxide (HfO_2) and aluminium oxide (Al_2O_3) are presented. The protected devices show enhanced electronic properties after isolation from ambient like strong n-type doping, vanishing hysteresis, and reduced device resistance. Effective control of the gate voltage allows tuning of the responsivity and temporal response by several orders of magnitude to achieve $R \sim 10^1$-10^4 A/W and $\tau \sim 0.01 - 10$ s. At strong negative gate voltage, the detector is operated at the fastest speed and simultaneously exhibits a low-bound, record sensitivity of $D^* \geq 7.7 \times 10^{11}$ Jones. The presented encapsulation route improves performance stability even under harsh humid conditions. Its versa-

tile implementation with other TMDCs is then shown for the example of few-layer $MoSe_2$ devices. The chapter concludes by emphasizing the importance of further investigation into encapsulated transition metal dichalcogenide optoelectronics and discusses fundamental limitations and challenges of 2D photodetectors.

4.1 Prior art in TMDC photodetection

Photodetection based on TMDCs has received a lot of attention in recent years and a huge variety of performance results has been reported. There are many different device concepts that involve TMDCs in the detection process. They can roughly be summarized as (i) lateral metal-TMDC-metal photodetectors with applied bias for operation as photoconductors (ii) vertical heterojunctions of diverse 2D material systems for operation as photodiodes and (iii) surface-decorated hybrid phototransistors. The majority of reports focuses on MoS_2 in a lateral metal-TMD-metal architecture to exploit the existence of trap states and to operate the detector with high photoconductive gain. However, the first prototypes have demonstrated varying performance parameters despite similar detector designs and fabrication methods. On the one hand, low responsivity on the order of 7.5 mA/W [40] for monolayer or 100 mA/W [41] for multilayer MoS_2 together with fast temporal response on the order of milliseconds has been shown. On the other hand, detectors with high gain and responsivity of up to 880 A/W have been reported, however at the cost of slow decay times extending to thousands of seconds depending on surface treatments [42]. Similar findings have been published for other TMDCs, both CVD-grown and exfoliated, suggesting extrinsic rather than material-related effects [43–52].

Despite its generally beneficial 2D profile, the large surface-to-volume ratio of 2D materials render detector performance sensitive to the environment. Recently, Furchi *et al.* demonstrated that the photoresponse of MoS_2 is based on two distinct mechanisms, the photogating and photoconducting effect [60]. The photogating mechanism originates from long-lived charge-trapping processes at surface-bound water molecules or other surface adsorbates and is responsible for the extremely slow response dynamics and high responsivity values. The photoconducting mechansim has been demonstrated by applying two light sources, where a continuous light source fills adsorbate-related traps and a rapidly modulated light source probes the material-related photoconductivity. Under these conditions much lower optical gain and fast response times are observed. In other studies, it has been proven that physisorbed gas molecules such as O_2 and H_2O withdraw electrons from the MoS_2 and $MoSe_2$ channels and electrically deplete the devices [90, 91]. Vacuum

annealing at temperatures higher than 100 °C has been found to strongly n-type dope few-layer TMDC field-effect transistors and significantly improve their resistance and mobility [92–94]. Many different encapsulation methods have been tested, each showing similar electrical improvements: after some pre-annealing in vacuum, passivating films of Al_2O_3 [78,95], HfO_2 [96], or Si_3N_4 [97] were deposited resulting in strong electron doping, improved electronic performance, and reduced hysteresis. Yet, the influence of encapsulation on responsivity and temporal response time for photodetection has not been investigated.

For successful employment of 2D materials as ultra-thin photodetectors in imaging and video capture applications, high sensitivity together with decay times of a few tens of milliseconds are required. To achieve this goal, a robust passivation scheme with industrially accepted and broadly used ALD encapsulation is implemented.

4.2 Encapsulated monolayer MoS_2-FETs

Figure 4.1 illustrates the device schematics and the corresponding I_{DS}-V_G modulation curves of MoS_2-FETs before and after encapsulation. One can immediately observe in the linear modulation plots that simple device encapsulation with HfO_2 improves FET characteristics considerably, resulting in much larger on-currents and vanishing hysteresis.

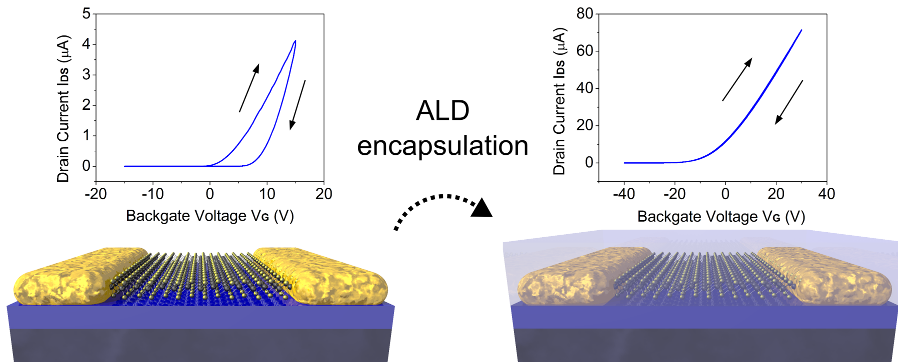

Figure 4.1: Encapsulated monolayer MoS_2-FET. Linear plot of the I_{DS}-V_G modulation curves (top) and its corresponding device schematic (bottom) before (left) and after (right) encapsulation. The simple device encapsulation with HfO_2 improves FET characteristics considerably with much larger on-currents and vanishing hysteresis.

The encapsulation approach is tested on several monolayer and bilayer MoS_2 devices and their electrical performance is measured before and after the ALD process to unveil the effects of encapsulation. The devices are fabricated on silicon substrates covered with 90 nm SiO_2 as described in chapter 3.2 and all measurements are performed under ambient conditions. The HfO_2 film is deposited by atomic layer deposition on top of the devices by using tetrakis(dimethylamino)hafnium and H_2O precursors. Previous reports on ALD growth of high-k dielectric oxides on TMDCs have shown non-uniform growth without prior surface functionalization or employment of a seeding layer [98]. To ensure full coverage and protection of the surface, a relatively thick oxide film of around 30 nm is deposited in a process of 300 cycles.

The physical mechanism behind the improvement of FET characteristics is sketched in Figure 4.2(a): the unprotected device is susceptible to all kinds of molecules from the atmosphere which physically adsorb on its surface, while adsorbates on the encapsulated device are removed by annealing prior to ALD deposition and the device remains protected by the oxide film.

In Figure 4.2(b), the modulation curve I_{DS}-V_G of an as-fabricated MoS_2 device is directly compared with the device encapsulated with HfO_2. The vanishing hysteresis is an indication of the removal of positive charges localized at the MoS_2 surface that trap and release electrons during forward and backward sweeps. While the curve of the as-fabricated MoS_2 shows a threshold voltage $V_{TH} \sim 2$ V, the ALD annealing and encapsulation shift its threshold down to $V_{TH} \sim$ -24 V. The n-type doping can be explained by the removal of charge-trapping adsorbates, H_2O and O_2, and by positively fixed charges inside the top-oxide layer that further induce electrons into the channel [95, 99].

From two-terminal measurements under low bias voltage the field-effect mobility and device resistance can be extracted. The mobility of this device improves clearly from 0.5 to 12 cm^2/Vs; a similar trend was seen for all monolayer and bilayer devices. The evident improvement of mobility is due to the removal of extrinsic charged impurities by the annealing process and quenching of homopolar phonon modes due to dielectric screening [94, 100]. Additionally the strong doping in the immediate vicinity of the metal contacts may also lead to lower contact resistance and increase the measured two-terminal field-effect mobility.

The device resistance reduces by $\sim$2 orders of magnitude from 5 MΩ to 55 kΩ at $V_G = 10$ V. Despite the strong doping, the device can be fully depleted at strong negative gate voltages, reaching the picoampere limit of the measuring unit. Moreover, it shows extremely high on/off ratios of 10^8 and ohmic output curves (see

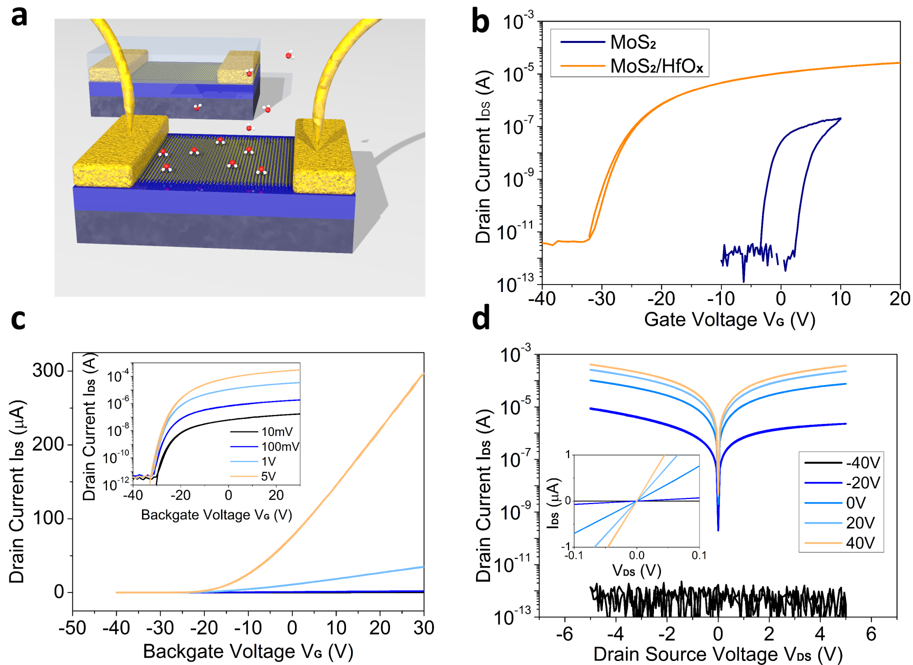

Figure 4.2: Device schematic, transfer, and output characteristics of MoS_2 and MoS_2/HfO_2 field effect transistor. (a) A 3D sketch of two typical TMDC FETs, the front device exposed to air and all types of molecules and the back device protected with HfO_2. (b) Transfer curve I_{DS}-V_G before and after ALD encapsulation. The protected MoS_2 FET shows strong n-type doping, vanishing hysteresis, and reduction of device resistance. (c) The transfer characteristics of MoS_2/HfO_2 for a range of bias voltages V_{DS} with on/off ratios of up to 10^8. The inset shows the curves in logarithmic scale. At very strong negative backgate voltage, the device can be switched off leading to dark currents of picoampere (at the limit of the measuring unit). (d) At V_G = -40 V, the device remains switched off even up to a high bias of 5 V while the output curves are nearly ohmic at positive V_G. The inset shows a linear plot of the I_{DS}-V_G curves. Channel dimensions: $W = 5\,\mu m$, $L = 3\,\mu m$.

Figure 4.2(c),(d)), as previously reported for HfO_2-encapsulated single layer MoS_2 FETs [96]. The improved mobility and resistance together with the ultra-low dark current in depletion constitute a fundamental basis for highly sensitive phototransistors. The performance of encapsulated devices was maintained for several weeks after encapsulation when stored inside a nitrogen glovebox.

4.3 Optoelectronic characteristics of MoS_2/HfO_2

In the previous section it is pointed out that the passivation layer improves electronic FET properties by strongly reducing the effect of extrinsic adsorbates. Likewise it is expected to minimize long trapping times in H_2O molecules on the surface, which lead to impractically long response times. Ideally, this is achieved without compromising the earlier reported high responsivity to maintain large sensitivity of MoS_2 phototransistors.

4.3.1 Responsivity and charge carrier dynamics

First, the spectral responsivity of a monolayer MoS_2-detector is measured over an incident wavelength range of 550 - 800 nm with a constant illumination power for all wavelength (Figure 4.3(a)). The transistor is operated in depletion at V_G = -32 V, which is the most sensitive region as will be explained later on. The spectrum reveals the expected sharp drop in response at $\lambda \sim 690$ nm, corresponding to its direct bandgap of 1.8 eV, and indicates the origin of photoresponse from the MoS_2 flake. Two prominent resonances, which stem from the direct bandgap transition at the K-point of the Brillouin zone, can clearly be resolved. These features, arise from optical transitions of the highest valence band to the lowest conduction band. The valence band is split due to spin-orbit coupling leading to the peaks denoted as exciton peak A and B [101]. The large spectral responsivity of more than 200 A/W throughout the visible absorption range indicates high sensitivity of the monolayer device based on photoconductive gain.

In figure 4.3(b) the gate-dependent transfer curve under dark and illuminated conditions shows the response of the phototransistor depending on the illumination power. The devices are illuminated globally with a spot size of 2 mm at a wavelength of 635 nm, which falls within its spectral selectivity. Even at a low power density of 25 μW/cm^2, a small shift in the threshold voltage can be detected and indicates a sensitive photogating effect.

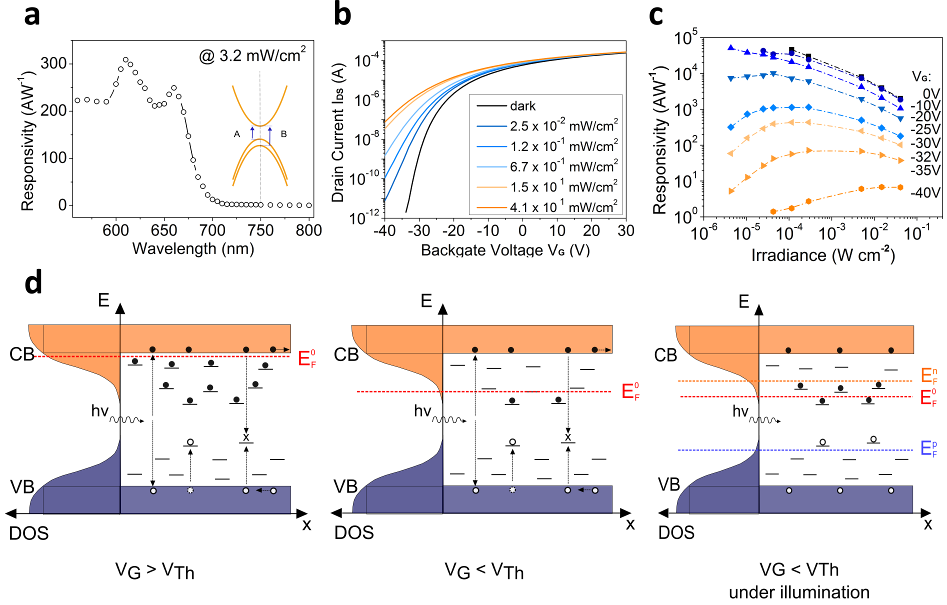

Figure 4.3: Optoelectronic response and charge carrier dynamics of MoS_2/HfO_2. (a) Spectral responsivity of a monolayer MoS_2/HfO_2 device measured at $V_G = -32$ V with an illumination intensity of 3.2 mW/cm^2. The two exciton peaks A and B, together with a sharp drop at 690 nm can clearly be resolved. (b) Measured I_{DS}-V_G curves in the dark (black) and under illumination with different light intensities (colored). (c) Power-dependent responsivity for a wide dynamic range at $V_G = -40$ V until 0 V. The responsivity was measured with a pulsed Laser at 635 nm with 1 Hz frequency. Two trends can be observed namely a general reduction of responsivity with gate bias strength and a drop in responsivity at lower illumination power in the regime of strongest gate voltage V_G. $V_{DS} = 5$ V. (d) Schematic to explain the behavior of power-dependent responsivity. On the left side of the energy axis, a bandgap model with continuous bandtail states for electrons and holes is shown. On the right side, a discrete model is used to depict the carrier excitation and trapping dynamics. The left image shows the case of $V_G > V_{TH}$. The centered and right images show $V_G < V_{TH}$ under dark and illuminated conditions, repectively. E_F^0 is the Fermi level, E_F^n and E_F^p the quasi Fermi levels of electrons and holes under illumination.

To gain deeper insight into the charge carrier dynamics under light, the power dependence of responsivity is measured for a wide range of light intensities and several backgate voltages $V_G \leq 0\,V$. Within this backgate range, the ratio I_{light}/I_{dark} reaches its highest value and is therefore most interesting for photodetection. The drain current I_{DS} is recorded over time and photocurrent is generated with a pulsed laser at a 1 Hz repetition rate and varying optical intensities. The resulting power-dependent responsivity is plotted in Figure 4.3(c), and a simple band model is sketched in Figure 4.3(d) to establish a physical picture behind the power dependence.

First, the backgate range of -20 to 0 V is considered, which corresponds to $V_G > V_{TH}$ in the schematic (left image). The band model is based on the existence of continuous bandtail and midgap states. These states are introduced in the bandgap due to disorder, defects, or sulfur vacancies and can lead to charge trapping and recombination, as previously reported [60, 102, 103].The right side of the y-axis shows a model with discrete gap-states to simplify the ongoing carrier dynamics, while the left side illustrates a more realistic, continuous energy distribution of the denisty of states (DOS). Under illumination, several mechanisms contribute to the overall photoresponse such as charge carrier excitation, separation, carrier trapping, and recombination. For $V_G > V_{TH}$, the Fermi level E_F is located close to the conduction band and the majority of available electron trap states is filled. In this case the power-dependent responsivity is dominated by hole traps. Under low light intensities, the deep lying, long-lived hole traps fill first and with increasing power the population of shallower trap states begins. The decay dynamics at higher optical intensities are determined by the high DOS of shallow traps. The long lifetime of trap states is essential for high photoconductive gain and thus the dominating shorter lifetime of shallow states reduces gain. This behavior is well-known for trap-dominated detectors and leads to sublinear power dependence of the photocurrent [104, 105]. The sublinearity can be observed in the logarithmic plot of Figure 4.3(c) where responsivity drops with increasing light intensity. Similar results were reported earlier for TMDC detectors [42, 44, 59]. The high responsivity of up to 5×10^4 A/W can be attributed to the low contact resistance at $V_G = 0\,V$, where the recirculation of electrons (gain) profits from lower shottky barrier heights due to the good alignment of conduction band edge with the contact metal.

For $V_G < V_{TH}$, a more complex behavior is met. A general trend of decreasing responsivity with rising modulation field strength can be seen with two different regimes in its power dependence: starting at the lowest powers an initial short rise of responsivity is observed with increasing power. At some point, a maximum respon-

sivity is reached, followed by a drop in responsivity at even higher power. This most sensitive point (responsivity maximum) shifts to higher illumination intensities with increasing gate strengths. To understand the mechanism behind this phenomenon, one has to carefully distinguish between recombination centers and (sensitizing) trap states [106, 107]. Recombination centers are located rather close to the midgap and favor recombination of electron–hole pairs, while trap states are closer to their corresponding band edge and are likely to trap one charge carrier for certain time depending on the depth of the trap state, contributing to photoconductive gain. At $V_G < V_{TH}$, the Fermi level E_F^0 (under dark conditions) moves away from the conduction band and frees progressively more gap states above it, which serve as recombination centers and reduce the responsivity (Figure 4.3(d) center). Under illumination, the electron and hole density is temporarily augmented (Figure 4.3(d) right) as demonstrated by the Quasi-Fermi levels E_F^n and E_F^p, respectively. Therefore, with an initial increase in light intensity, the Quasi-Fermi levels move apart and embrace more unoccupied recombination channels, effectively prolonging carrier lifetime of the majority carrier and consequently increasing responsivity. Because at stronger field modulation E_F^0 consecutively moves further into the midgap and the number of unoccupied recombination centers increases, higher light intensity is needed to fill these states and the responsivity maximum shifts to higher power. After that point, the quasi-Fermi level E_F^n approaches the conduction band and the same conditions are given as for $V_G > V_{TH}$, depicted in the left image of the schematic. Accordingly, the responsivity drops again as hole traps start to fill.

This is a simplified model to account for the experimental findings of Figure 4.3(c). In reality, more complex mechanisms are at play due to a possibly different trap energy distribution, trap density, and carrier capture probability for electrons and holes [106, 107]. Apart from the trap model, the increase in contact resistance for stronger gating and its influence on gain has to be taken into account.

4.3.2 Temporal response

One of the major limitations of previously reported MoS_2 phototransistors is a frequency response of much lower than 1 Hz for sensitive devices with gain, originating from long trapping times at surface-bound H_2O molecules underneath and on top of the MoS_2 flake. Yet, little effort has been put into reducing the effect of adsorbates and improving TMDC photodetectors in terms of speed, while maintaining high responsivity. Unprotected ultrathin MoS_2 devices usually suffer from current drifting after illumination, have extremely slow decays back to their previous dark

current levels or demonstrate persistent photoconductivity [44,108], thus hampering a reliable study of the decay dynamics in MoS_2 detectors.

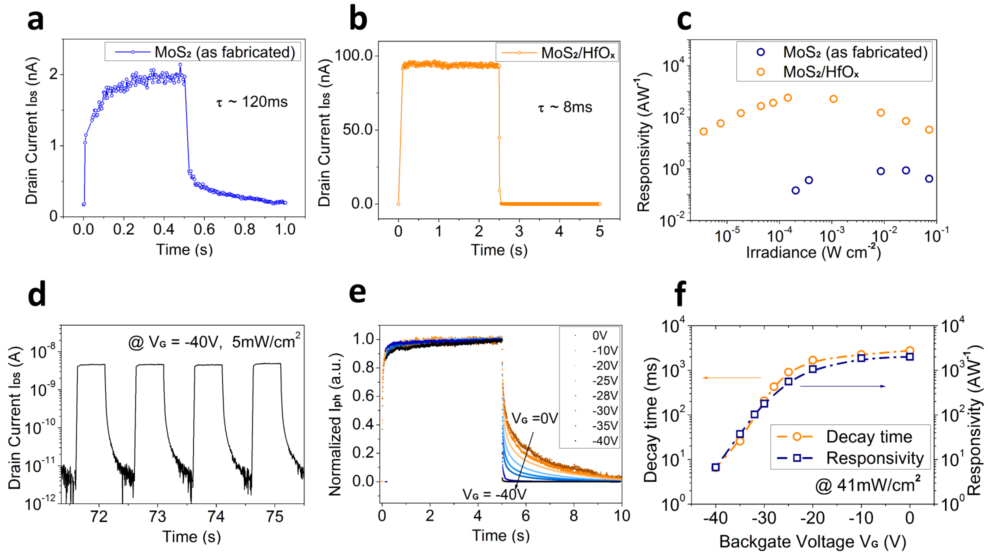

Figure 4.4: Encapsulation effect on photoresponse and temporal response of mono- and bilayer devices. Drain current during 1 cycle of light modulation for a bilayer MoS_2 device (a) and its corresponding protected device MoS_2/HfO_2 (b). The photocurrent increases by a factor of ∼40 and at the same time the decay time decreases by more than 1 order of magnitude. $V_{DS}=1$ V. (c) Direct comparison of power-dependent responsivity before and after HfO_2 encapsulation of a bilayer MoS_2 device. The responsivity is measured at backgate voltages where the device is fully depleted at $V_G=$-10 V and $V_G=$-40 V for MoS_2 and MoS_2/HfO_2, respectively. The responsivity is improved by more than an order of magnitude and the device is sensitive to even lower illumination intensity than before. $V_{DS}=1$ V. (d) Logarithmic scale photoresponse to light pulses of 5 mW/cm^2 with 1 Hz repetition rate. The pulses are stable, the drain current I_{DS} does not drift and returns to the initial picoampere level after switching off the light. (e) Normalized photocurrent pulses measured at 100 mHz and 41 mW/cm^2 for several backgate voltages. With increasing gate bias, the decay times (90 % - 10 %) reduce significantly. (f) The responsivity of a single layer MoS_2 device and its corresponding decay time as a function of backgate voltage plotted for 41 mW/cm^2 illumination intensity. $V_{DS}=5$ V.

In this section the influence of encapsulation on the temporal response of mono- and bilayer devices is studied. Figure 4.4, panels (a) and (b), show the measured I_{DS} during one cycle of light modulation for a bilayer MoS_2 device before and after encapsulation, respectively. The photocurrent improves by a factor of ∼40 while the decay time decreases by more than 1 order of magnitude.

The power-dependent responsivity of another bilayer device is illustrated before and after HfO_2 encapsulation in Figure 4.4(c). To fairly compare the device performance with and without encapsulation, the response is measured in the depletion of each device, i.e. at a backgate voltage at which the minimum dark current level is reached. This is the case at V_G = -10 V for MoS_2 and at V_G = -40 V for MoS_2/HfO_2, because of the strong doping after encapsulation. Significant enhancement of both responsivity and speed is observed for all measured devices after the encapsulation process. Moreover the strongly gated, encapsulated detectors demonstrate stable and constant photo-switching performance throughout many switching cycles. The logarithmic plot of drain current over time in Figure 4.4(d) displays the devices' fast decay to its initial dark conductivity after switching off the light source.

As discussed in the previous section, the gate voltage has a strong influence on the gain of the device because it controls the occupancy of gap states which, in turn, will affect its temporal response. Figure 4.4(e) compares the normalized photocurrent, measured at the same illumination power of 41 mW/cm^2, for different gate biases $V_G \leq 0$ V. The temporal response strongly depends on applied field modulation and is in agreement with the responsivity behavior: the larger amount of unoccupied recombination channels at strong gate voltage effectively shorten the majority carrier lifetime, resulting in much faster temporal response down to 7 ms.

The fall times, measured from 90 % to 10 % of the maximum photocurrent after light is switched off, together with its corresponding responsivity measured at 41 mW/cm^2 are plotted versus V_G in Figure 4.4(f). The decay of the photocurrent after ceasing the excitation depends on the light intensity incident on the device. The temporal response at lower intensity is primarily determined by the long lifetime of deep hole traps. With increasing intensity the deep trap states get saturated and the short-lived, shallow hole traps populate and dominate the decay dynamics. Thus, the decay time gets faster with higher illumination intensity.

4.3.3 Noise and sensitivity

As shown in previous sections, the responsivity and time response depend significantly on backgate voltage and can vary by orders of magnitude depending on if the device is operated in its depletion or accumulation regime. Although the highest responsivity is measured in the accumulating regime, the nearly ohmic contacts lead to lower contact resistance and thus result in high dark current that counteracts sensitive photodetection. While many TMDC photodetector reports focus on responsivity, reported at a variety of different V_G, a more important figure of

merit is the detectivity D* that also takes into account the bandwidth, geometry, and noise of the device. To get a quick estimation of the upper limit of sensitivity, the shot-noise can be considered as main noise source component, as explained in chapter 2. 2D materials however contain a predominant 1/f noise component due to non-ohmic contacts and disorder or edge defects, that cannot be neglected [109–111].

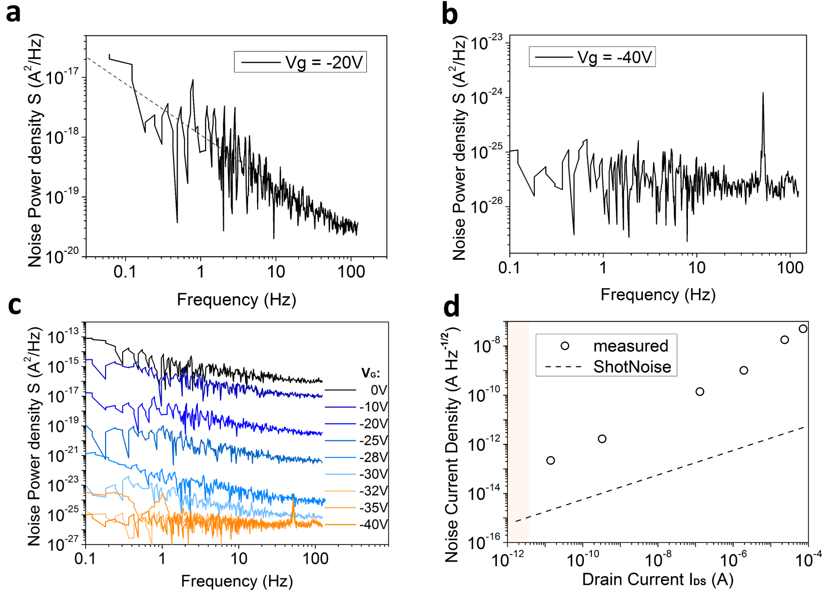

Figure 4.5: Measured noise and shot-noise limit. Measured noise power density at V_G = -20 V (a) and V_G = -40 V (b). At -20 V a clear 1/f component can be observed for the measured low-frequency range, whereas the noise floor of the measuring unit is reached at -40 V where the noise power density of the device cannot be determined. (c) Noise power spectral density for a full range of backgate voltages. Most of the curves show 1/f behavior except for the strong gating regime at -35 V and -40 V. (d) Measured noise current density versus shot-noise limited noise current density. For strong gating bias, the dark current reduces and the measured noise current slowly approaches the shot-noise limit.

In Figure 4.5, panel (a) and (b), the measured noise power density at V_G = -20 V and V_G = -40 V is plotted, respectively. At moderate gate voltage of -20 V, a clear 1/f noise component can be observed for the measured frequency range. At -40 V the noise floor of the measuring unit is reached, and the real noise power density of the device cannot be distinguished from the system noise. This is the lowest noise level measurable with the used Agilent system, corresponding to picoamperes of dark current.

Figure 4.5(c) summarizes a full set of measured spectral noise densities at dif-

ferent V_G to later determine the backgate-dependent detectivity. A considerable decrease in the spectral noise density by several orders of magnitude for stronger gating voltages can be observed due to the reduction of dark current. Most of the measured curves show 1/f behavior except for the strong gating regime at -35 V and -40 V, where the spectral noise density doesn't originate from the device. Rather it originates from the noise floor of the measuring unit, resulting in a flat line. Figure 4.5(d) demonstrates the measured noise and the calculated shot-noise versus dark current. The measured noise slowly approaches the shot-noise limit with increased gating strength, showing that there is still plenty of room for improvement.

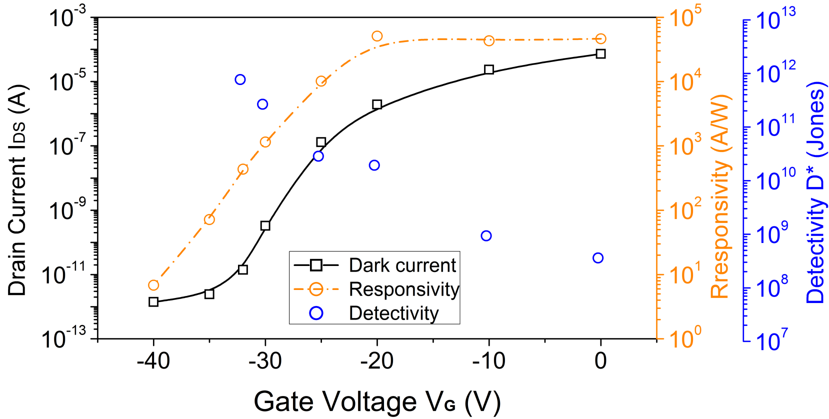

Figure 4.6: Gate-dependent performance parameters. Drain current I_{DS} (dark), responsivity R, and measured detectivity D* as a function of back-gate voltage V_G. The responsivity values correspond to the maximum values of Figure 4.3(c) for each backgate voltage. Despite the drop in responsivity for more negative V_G, the faster decreasing noise leads to an increase in sensitivity with maximum measured $D^* = 7.7 \times 10^{11}$ Jones at $V_G = -32$ V. At stronger V_G, the measuring unit reaches its noise floor. $V_{DS} = 5$ V.

Figure 4.6 outlines the dark current, the maximum responsivity and the resulting measured detectivity versus backgate voltage, recorded at a bandwidth of 1 Hz. Despite the huge responsivity values from $V_G \sim -20$ V to 0 V, the detectivity shows its lowest values due to the noise from the high dark current. The detectivity increases for stronger gating and reaches a maximum of 7.7×10^{11} Jones at $V_G = -32$ V; to the best of our knowledge this is the highest MoS_2 detectivity reported at the time of writing.

Following the observed trend of decreasing noise faster than responsivity at negative backgate voltage, further improvement of the sensitivity is expected at even stronger gating, where the actual noise of the device cannot be resolved with

the used measurement unit. The shot-noise limited detectivity of this device reaches 8×10^{13} Jones, 2 orders of magnitude higher than the measured sensitivity, showing the huge potential of MoS_2 for sensitive photodetection. Owing to the 1/f nature of the noise spectral density and the millisecond time response, even better detectivity can be achieved by measuring with lock-in detection at higher frequencies.

4.4 Stability under environmental stress conditions

To prove the impact of H_2O molecules on performance and stability of the devices, a series of control experiments have been conducted by exposing devices to highly humid conditions. Therefore two monolayer devices are prepared, a pristine MoS_2 and an encapsulated MoS_2/HfO_2, which are expose to the same humidity conditions at the same time. Both samples are characterized in ambient conditions first and then exposed to different humidity conditions inside a climatic chamber with relative humidities (RH) of 40 %, 60 % and 80 %. Both samples are kept inside the chamber under stable RH values for around one hour and then measured immediately afterwards.

The results are depicted in Figure 4.7 for the pristine (a) and the encapsulated device (b). The pristine device is clearly affected by the harsh environment and shows an increase in the hysteresis and a strong reduction in the on-current. The initial mobility of 3.7 cm^2/Vs in air is reduced to 1.7 cm^2/Vs, 1.4 cm^2/Vs and 0.9 cm^2/Vs after exposure to 40 %, 60 % and 80 % respectively. The protected device, on the other hand, shows minor impact from the harsh conditions. The I_{DS}-V_G curve remains free of hysteresis and mobility marginally changes, despite its exposure to relative humidity of up to 80 %.

Also the photoresponse and decay dynamics are quite stable after the humidity exposure and the devices show responsivities on the order of 30 A/W (measured at V_G = -40 V) with decay times of 90 - 150 ms, while the pristine devices measured under same conditions yield responsivities of 4 A/W with corresponding decay times of 2-3 s.

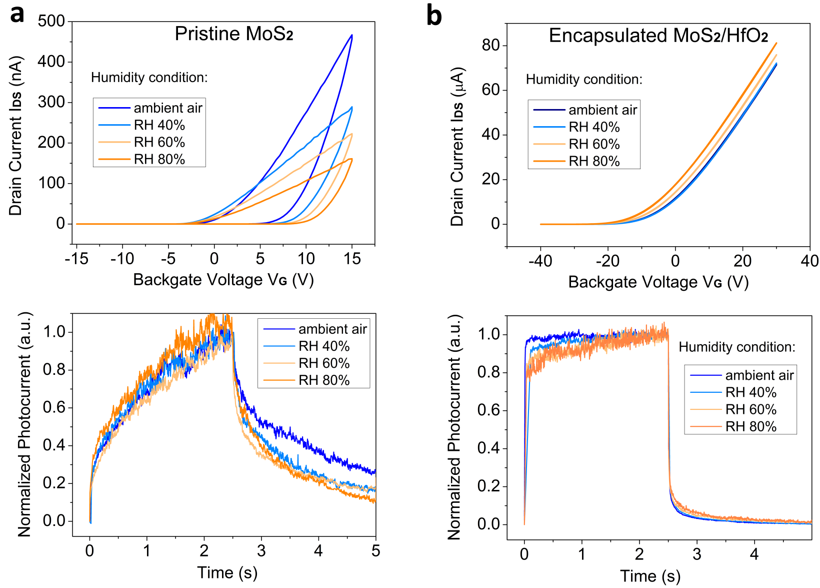

Figure 4.7: MoS_2 vs. MoS_2/HfO_2 device performance after exposure to humid conditions. The top panel shows the linear I_{DS}-V_G curves of the pristine (a) and the protected device (b) measured before and after different RH treatments of 40 %, 60 % and 80 %. The bottom panels show the corresponding decay dynamics.

4.5 Encapsulation of other TMDCs: $MoSe_2$

The findings of the previous sections demonstrate that the optoelectronic device performance is considerably enhanced by the covering oxide. To prove that this encapsulation route is versatile and generally applicable to other TMDCs or other encapsulant materials, a monolayer MoS_2 device encapsulated by Al_2O_3 and a multi-layer $MoSe_2$ device encapsulated with HfO_2 were fabricated.

Both devices exhibit a similar trend after encapsulation: reduction in hysteresis, n-type doping, and improvement in mobility (see Figure 4.8). The results of optoelectronic measurements for the $MoSe_2$ device are illustrated in Figure 4.9. A simultaneous enhancement of responsivity and temporal response as described in the previous chapters prove TMDC photodetectors generally benefit from encapsulation. Table 4.1 summarizes all investigated devices and their most important device characteristics for photodetection.

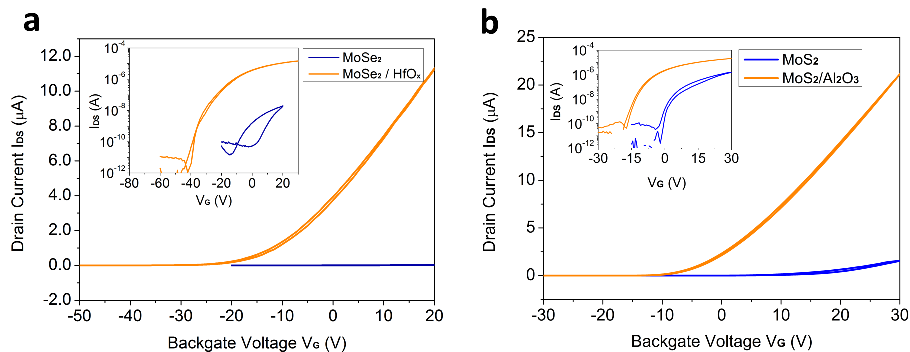

Figure 4.8: Modulation curves before and after encapsulation of $MoSe_2/HfO_2$ and MoS_2/Al_2O_3. Linear plot of the transfer curve I_{DS}-V_G before and after encapsulation of $MoSe_2$ with HfO_2 (a) and MoS_2 with Al_2O_3 (b). The insets show the corresponding logarithmic plots.

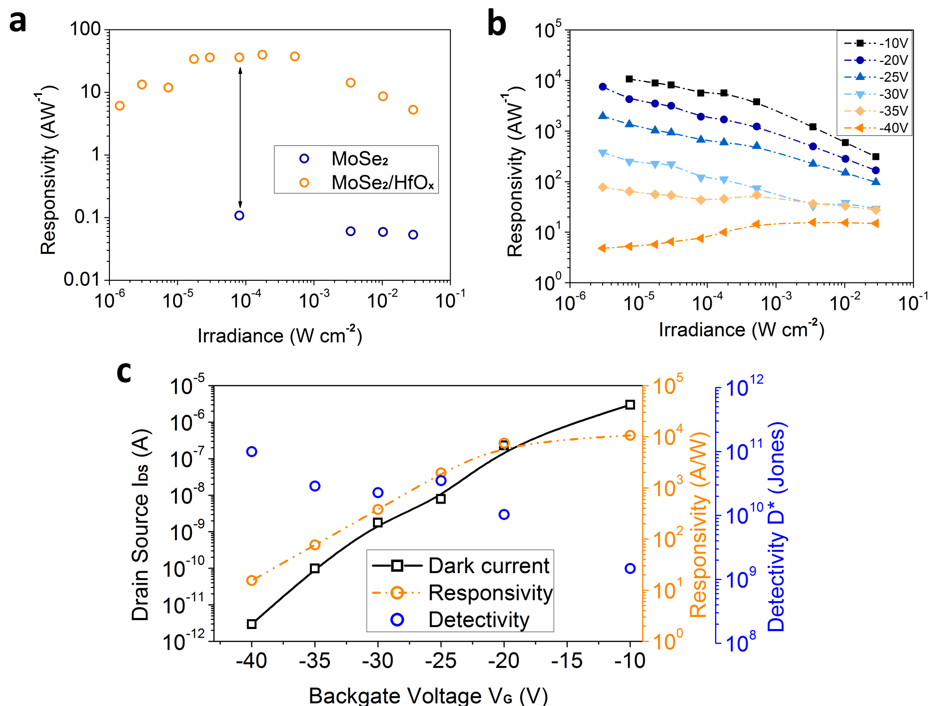

Figure 4.9: Full set of performance parameters of $MoSe_2/HfO_2$. (a) Illumination power dependent responsivity before and after HfO_2 encapsulation. The protected device is more sensitive to lower irradiance, and responsivity is enhanced by 2 orders of magnitude. $V_{DS} = 1V$. (b) Power dependent responsivity for different backgate voltages. $V_{DS} = 5V$. (c) Dark current, responsivitiy and detectivity as a function of backgate voltage. A similar trend as seen in MoS_2 devices is evident.

Table 4.1: Performance parameters of all fabricated devices.

Device	MoS_2 - 1	MoS_2 - 2	MoS_2 - 3	MoS_2 - 4	$MoSe_2$
Layer thickness	monolayer	bilayer	bilayer	monolayer	multi-layer
Dimension (W×L)	$5\times3\mu m^2$	$7\times4\mu m^2$	$12.5\times2.4\mu m^2$	$6\times1.5\mu m^2$	$11.5\times6.5\mu m^2$
Oxide	HfO_2	HfO_2	HfO_2	Al_2O_3	HfO_2
V_{DS}	5V	3V	1V	5V	5V
Mobility (pristine)	$0.5\,cm^2/Vs$	$6.4\,cm^2/Vs$	$3.3\,cm^2/Vs$	$10\,cm^2/Vs$	$5.9\,cm^2/Vs$
Mobility (encaps.)	$12\,cm^2/Vs$	$21.5\,cm^2/Vs$	$8.1\,cm^2/Vs$	$52\,cm^2/Vs$	$16\,cm^2/Vs$
Responsivity (depleted)	434 A/W	400 A/W	563 A/W	406 A/W	16 A/W
D^* (depleted)	7.7×10^{11} Jones	7.0×10^{10} Jones	1.7×10^{12} Jones	3.8×10^{11} Jones	1.0×10^{11} Jones
Decay time (depleted)	7 ms ($41\,mW/cm^2$)	10 ms ($41\,mW/cm^2$)	180 ms ($26\,mW/cm^2$)	55 ms ($3.5\,mW/cm^2$)	5 ms ($3\,\mu W/cm^2$)

4.6 Summary and outlook

In summary, it has been shown that encapsulation of TMDCs is a versatile route to enhance optoelectronic performance of ultra-thin 2D photodetectors. The large surface-to-volume ratio makes 2D materials prone to the detrimental impact of extrinsic factors such as adsorbates. Successful passivation schemes will therefore be essential in future device designs. The proof-of-concept passivation method, presented in this chapter, has largely demonstrated a solution to one of the biggest obstacles to date for TMDC phototransistors: the slow detector response time. To date, either fast and poorly responsive or slow and highly responsive MoS_2 phototransistors have been reported. This work has shown that an improvement of both the responsivity and response time is achieved by encapsulation. The sensitivity of the device is thereby enhanced to a record detectivity D^* of up to 10^{12} Jones in the devices' depletion regime. Moreover, in this regime the detector is operated at its

fastest speed, with response times around 10 ms or less, rendering the studied TMDC detectors capable of video capture applications. The D* of 10^{12} Jones approaches the sensitivity of Si-photodiodes, which is remarkable considering the device consists of only monolayer MoS_2 sheets with sub-nanometer thickness. The high sensitivity is achieved due to the extremely large photoconductive gain, together with ultra-low dark currents in depletion that minimize noise.

The stability in harsh humid conditions has been improved significantly compared to pristine devices. Moreover, the passivation technique has been proven to be a versatile approach generalizable to other material systems and encapsulants. This warrants further investigation to refine ALD growth and achieve high oxide quality on TMDCs for better passivation results. We anticipate that other protection schemes based on boron-nitride or organic coatings may also strongly improve device efficiency and stability. The performance of the TMDC phototransistor depends on mobility, contacts and noise, which all still have plenty of room for improvement. The growing knowledge in the community will therefore push the development of 2D crystal-based detecting systems forward.

A fundamental challenge of 2D detectors is their limited absorption. Although a monolayer of MoS_2 with a thickness of only 0.7 nm has remarkably high absorbance in the visible [112, 113], it is too low in absolute terms and impractical for some device applications. It is therefore a key task to maximize light-matter interaction within the material or to increase its absorption efficiency by other means.

Apart from the low absorption, there are other mechanisms inherent to MoS_2 that lead to recombination losses. Due to spatial confinement in the z-direction and low electrostatic screening [114], electron-hole pairs are strongly bound to each other, with reported exciton binding energies of 300 - 900 meV [101,115,116]. Photoexcited electron-hole pairs can easily recombine before they get separated by the applied electric field. In addition, the strong coulomb interactions in 2D materials favor Auger scattering processes, which lead to capture of electrons and holes at defect sites [117]. The well-known abundance of defect-states in MoS_2 leads to recombination channels which effectively decrease the quantum efficiency of MoS_2 detectors.

The quantum efficiency of the investigated devices can roughly be calculated from the measured responsivity R and from an estimation of the photoconductive gain by using equation 2.2 and 2.3: knowing the channel length, applied bias, and mobility, a transit time of 1 - 10 ns is estimated for the investigated devices. With measured decay times from Figure 4.4 corresponding to the carrier lifetimes, the gain is calculated to be on the order of 10^5-10^6 electrons per absorbed photon for

the strongest gating. Even higher gain is present approaching zero gate voltage. From the corresponding responsivity, a quantum efficiency of ~ 0.002 - $0.02\,\%$ is estimated. This indicates a significant amount of recombination losses before the charge carrier can be extracted into the electronic circuit.

From photoluminescence studies it is known that the quantum yield suffers strongly from the aforementioned recombination losses, and similarly poor yields of 0.001 - 0.1 % have been reported [63, 117]. Just recently the immersion of MoS_2 devices in organic superacids has shown to largely passivate electronically active defect-sites and enhance photoluminescence quantum yields by several orders of magnitude to 95 % [115]. New passivation methods based on chemical surface treatment or post-sulfurization of devices are encouraging ways to repair defects, such as the ones caused by sulfur vacancies. The controlled engineering of traps will open a new path to further enhance optoelectronic properties of 2D TMDCs.

5

Hybrid 2D-0D TMDC-QD phototransistor

Sensitive photodetection relies on detectors with large gain and low dark currents to facilitate a high signal-to-noise ratio. In the previous chapter it has been demonstrated that 2D dichalcogenides offer excellent mobilities for large carrier multiplication and a bandgap suited for for low dark-current operation in a phototransistor architecture. However, the wavelength range for efficient photodetection is limited by the large bandgap in the visible range and the weak light absorption in few-nanometer thin TMDCs. This requires a new strategy for enhanced light-matter interaction. Low-cost photodetectors based on colloidal quantum dots have emerged as new platform for high sensitivity sensing [104,105,118,119] across a broad spectral range. Yet, their performance is limited by the poor carrier mobility in quantum dot solids. In this chapter, the unique electronic properties of ultrathin MoS_2 channels are combined with the strong optical absorption of PbS colloidal quantum dots in a hybrid TMDC-QD phototransistor configuration. The hybrid device generates ultra-high gain on the order of 10^6 electrons per photon as a result of the high mobility of MoS_2. The spectral selectivity of the hybrid is now tunable across the vis-NIR and SWIR spectrum, because of the tailored bandgap of quantum dots. The effect of an applied backgate voltage to increase the sensitivity is exploited,

and different 2D and 0D materials are successfully incorporated in hybrid detectors. The sensitization of TMDCs with colloidial quantum dots is a promising synergy in which the inherent weakness of both systems, the low mobility in QDs and the low absorption efficiency in TMDCs, are overcome.

5.1 Colloidal quantum dots

Colloidal QDs (CQDs) are semiconducting nanocrystals synthesized in solution with diameters of a few nanometers. The nanometer-scale of these crystals confines its electrons and holes spatially in all three dimensions, leading to interesting quantum effects [120, 121]. By simply changing the size or the shape of QDs during synthesis, optical and electrical properties can be tuned and adapted to the intended application. The most peculiar feature of these quantum confinement effects is the size-tunable optical bandgap, which allows one to readily tune the absorption onset throughout a large spectral wavelength range from the visible to MIR. Over the last few decades, the research field of CQDs has witnessed rapid growth, and improved control over material synthesis and further device engineering has led to high quality photovoltaic [122], photodetecting [123, 124] and light-emitting devices [125–127]. In this section, a basic framework of the field of CQDs is provided to understand the advantages of their combination with 2D materials for sensitive photodetection.

Synthesis and surface chemistry. An attractive characteristic of CQDs is the manufacturing of solid semiconducting devices from a material in the solution phase. This allows the employment of low-cost deposition methods. Many bottom-up synthetic routes have been developed to produce CQDs in solution. The hot injection method, based on the injection of precursors into organic solvents at elevated temperatures, has been established as a standard method for high-quality nanocrystals (Figure 5.1). The procedure involves several reaction parameters, like injection temperature, precursors, stabilizing surfactants and reaction timing, that control the size, shape and composition of QDs. The synthesis consists of several consecutive stages: the nucleation stage from precursors, followed by the growth stage from the initial nuclei and finally the isolation of the nanocrystals from the reaction mixture. It is of importance to strictly separate the growth from the nucleation stage to achieve a highly monodisperse solution with narrow size distribution.

The surfactants, which typically are organic ligands, adhere to the QD surface during synthesis and prevent agglomeration. The entire reaction is carried out under inert gas atmosphere using standard Schlenkline techniques and maximum temperatures well below 200°C. Therefore, solution processing provides a convenient and

simple material manufacturing method at low cost compared to complex epitaxial methods, which require ultra-high vacuum conditions, high growth temperatures and expensive machinery. Diverse material processing methods like spin-coating, inkjet-printing or roll-to-roll techniques have evolved to produce cost-effective thin solid films on a large scale.

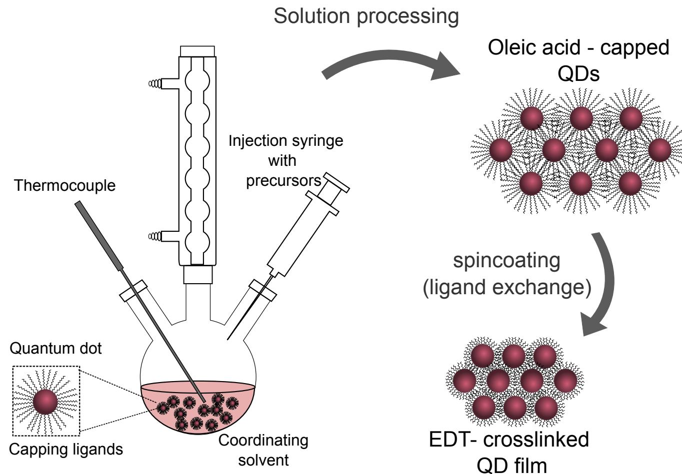

Figure 5.1: Hot-injection synthesis and ligand exchange of CQDs. Schematic of the synthetic apparatus to manufacture colloidal quantum dots. The solution-processed QDs are capped with long oleic acid ligands. A ligand exchange reaction is applied during the spincoating process to shorten the interparticle spacing for improved transport. The ligands used in this work to efficiently crosslink PbS QDs is ethanedithiol (EDT).

The CQD semiconducting compound of choice in this thesis is lead-sulfide (PbS). The final synthesis product, used for device fabrication, consists of PbS QDs with diameter of 2 - 10 nm capped with oleic acid ligands and dissolved in organic solvents. Oleic acid ligands are long-chain carboxylic acids with a length 18 carbon atoms. They are not only important for the chemical reaction process during synthesis, but also prevent oxidization and maintain the colloidal stability during further processing. Apart from that, the capping ligands play a major role in assembling nanocrystal solids for optoelectronic devices, as they finally determine the inter-particle spacing and have an impact on properties like electronic structure, nano-crystal interaction, and charge transport. The long distance between QDs capped with oleic acid (~2.5 nm) yields electrical isolation of the nanocrystals and largely increases device resistance [104]. Theoretically, the complete removal of ligands during solid film fabrication is the ideal scenario in view of inter-particle charge transport. However, it has been shown that the entire removal of ligands

(”necking”) can lead to deep-lying long-lived trap states, surface dangling bonds, and agglomerations [121]. Therefore, careful selection of appropriate ligands is crucial to control trap state density through surface state passivation and to obtain effective charge transport between nanocrystals. To date, several well performing ligand exchange reactions have been reported involving shorter organic and cross-linking ligands such as mercaptopropionic acid (MPA) and ethanedithiol (EDT) or inorganic capping ligands based on halides (Cl^-, Br^-, I^-) [122].

Spectral tunability of PbS QDs. The most intriguing characteristic of PbS QDs that is highly interesting for optoelectronic technologies is the tunable bandgap due to the quantum size effect. Bulk PbS has a small bandgap of 0.4 eV and excitons possess large Bohr-radius around 18 nm [128]. If the nanocrystal size of PbS QDs is on the order of the de Broglie wavelength of its charge carriers, quantum mechanical effects arise due to the spatial confinement. For PbS QDs, this is the case at crystal diameters smaller than roughly twice its exciton Bohr-radius. Highly monodisperse QD solutions (dispersion $< 5\%$) have been synthesized, and the bandgap has been tuned through a large spectral range from vis-SWIR by simply varying the QD diameter from 2 - 10 nm. Spectral absorption measurements in Figure 5.2 show the sizeable bandgap of PbS QDs with a shift of exciton peak from 600 - 1800 nm, where the energy gap decreases with increasing QD diameter.

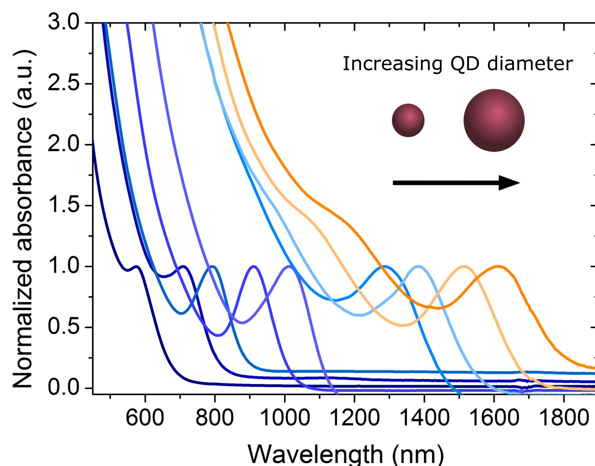

Figure 5.2: Absorbance spectra of PbS CQDs. Size tunable absorbance spectra of solution-processed PbS CQDs. The exciton peak shifts to longer wavelength with increasing QD diameter and a spectral range from 600 - 1800 nm is covered.

5.2 Hybrid 2D–0D photodetectors

Photodetectors made of colloidal PbS QDs have shown tremendous potential for highly sensitive light detection. Both photodiodes [120, 129] and photoconductors [104, 105] have been demonstrated with compelling performance, ready to compete with state-of-the-art technology. Their high sensitivity, low-cost fabrication, facile integrability with current CMOS technology, and variable spectral selectivity make CQD devices potential candidates for a new generation of photodetectors.

QD photoconductors especially have received renewed interest, since the existence of midgap trap-states yields gain on the order of 10^3 electrons per photon, thus offering detection and amplification within the same component. The sensitivity of final sensor arrays is often limited by the noise floor of the signal processing equipment (amplifier noise), as in the case of photodiodes. The internal amplification of photoconductors, however, can be benefitial if the output signal is raised above the noise floor of external components, thereby increasing the overall sensitivity of detector arrays. In order to improve the sensitivity of CQD photoconductors, noise has to be reduced and its inherent gain has to be further amplified. One way to increase gain is extended trapping time, which in turn would also lead to undesired slower response dynamics. A preferable solution is to decrease the carrier transit time, which, considering constant channel dimensions and bias voltage, can only be achieved by increase of mobility (see Equation 2.2).

While 2D photodetectors provide excellent electronic transport properties, they suffer from low absorption efficiency as seen in the previous chapter. Contrary is the case for CQDs: CQD solids are known to exhibit poor mobility in the range of 10^{-3} to $10^{-1}\,\mathrm{cm^2/Vs}$ due to inefficient charge hopping transport; however they strongly absorb light. The design of a hybrid 2D-0D device architecture combines the strength of both material systems. The hybrid phototransistor concept consists of a 2D FET sensitized with CQDs. After efficient light absorption in the QD solid, the photo-excited charge carriers are separated at the interface, provided that a proper heterojunction is formed. While one carrier type remains trapped inside the QD film, the other carrier is transferred into the 2D channel and recirculates the channel, benefiting from efficient carrier transport. The high carrier mobility of the channel, ideally orders of magnitude higher than in CQDs, then leads to much shorter transit times and enhances the internal current amplification.

To achieve large photoconductive gain, graphene is ideal for sensitized photo-FETs. The outstanding mobility in a single sheet of graphene of 10^3 - $10^4\,\mathrm{cm^2/Vs}$ is fundamental for high internal carrier multiplication. In addition, the control of

doping with gate voltage simplifies the formation of an efficient heterojunction with a semiconducting absorber of any polarity. Many distinct hybrid devices based on graphene have been investigated, making use of the large mobility in graphene and relying on the better absorption properties of sensitizers like TiO_2 [130], CNTs [131], TMDCs [132, 133], perovskites [22], PbS QDs [21, 23]. The most notable performance has been observed for the combination of graphene with colloidal PbS QDs. Ultrahigh gain on the order of 10^8 and sensitive detection of low light intensity down to 10 fW was achieved. One reason for such performance is the generally very attractive characteristics of PbS QDs for its use as sensitizers:

- The relatively long carrier lifetimes on the order of 1 - 10 μs [128] give photo-excited carriers enough time to diffuse to the junction between 2D channel and PbS, where holes and electrons get separated. Long diffusion length of 150 - 250 nm [124] and low exciton binding energies in PbS CQDs are benefitial factors for high charge transfer rates.
- The solution processing of the material facilitates its integration with 2D materials by simple spin- or spray-coating and is compatible with standard CMOS technology. The QD film thickness can thereby be optimized between absorption and charge transfer.
- The myriad of existing ligands to cap QDs allow improved transport, engineering of carrier lifetimes and even modification of the absolute energy of conduction and valence bands without changing the optical bandgap [134].
- The spectral tunability of PbS adds another degree of freedom. A simple change of QD size during synthesis allows one to adapt the hybrid's sensitivity to the desired spectral range from UV-SWIR.

One of the key challenges of graphene-based hybrid devices is the lack of a band gap and the resulting large dark currents. However, with the discovery of semiconducting TMDCs, a new class of materials interesting for hybrid phototransistors has emerged, which offers high in-plane mobility and the added advantage of field-effect controllable conductivity.

5.3 Vis-SWIR sensitive MoS_2/PbS photodetector

The focus of this work is on the two material systems MoS_2 and PbS. Although mobilities of the investigated few-layer MoS_2 devices are much lower than mobility in graphene, the achieved values of 1 - 60 cm^2/Vs significantly exceed the average 10^{-3} - 10^{-2} cm^2/Vs of fabricated PbS reference devices. Few-layer MoS_2-FETs are fabricated as explained in previous chapters and then a 40 - 60 nm thick QD film of oleate-ligand capped PbS is spin-coated over the device. Through a layer-by-layer deposition technique, the ligand exchange to much shorter 1,2-ethanedithiol (EDT) has been carried out to improve charge transfer from PbS to MoS_2. Several other ligands, commonly used for optoelectronic devices, have been tested, but best performance is obtained with EDT.

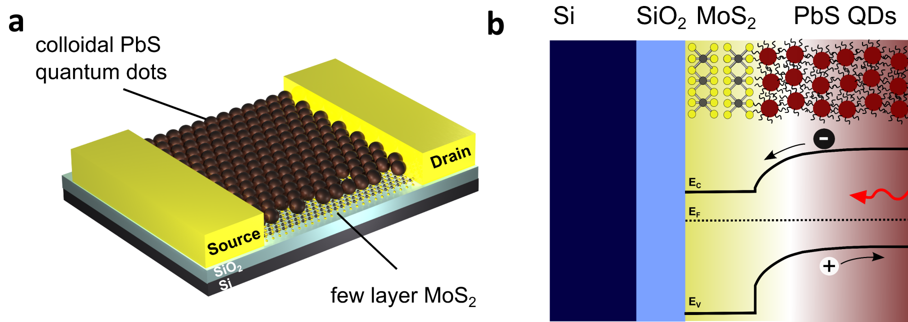

Figure 5.3: Device schematics and band alignment of MoS_2/PbS hybrid. (a) 3D view of a hybrid device architecture, which consists of a few layer n-type MoS_2 nanosheet on top of a Si/SiO_2 substrate with Ti/Au source and drain contacts in a two probe configuration. The colloidal p-type PbS film overcoats the whole device architecture. (b) Energy level diagram of the hybrid device. After QD deposition, electrons flow from MoS_2 into the PbS film until a built-in field has formed at the p-n-junction and Fermi levels are in equilibrium. Under illumination, the created electron-hole pairs are separated at the MoS_2/PbS interface.

The hybrid MoS_2–PbS device architecture is illustrated in Figure 5.3(a) with the resultant band-diagram of the heterojunction in Figure 5.3(b). Upon deposition of p-type PbS QDs on n-type MoS_2, electrons flow from MoS_2 into the PbS film until Fermi levels are in equilibrium and a bulit-in field has been generated at the interface. Incident light is absorbed in the PbS QD film and photo-excited electron-hole pairs are separated at the p-n-interface between MoS_2 and PbS. While holes remain within the QD layer, electrons drift vertically into the MoS_2 channel and travel to the electrode driven by an applied electric field.

5.3.1 Doping effects after PbS deposition

The main feature of this hybrid architecture is the field-effect modulated current flow controlled by application of a back-gate voltage. At strongly negative V_G, the gating depletes the n-type MoS_2 sheet and increases the resistance of the device (operation in OFF-state). By increasing V_G, the MoS_2 channel falls in the accumulation regime, and the transistor is in the ON-state. For practical photodetector applications the operational regime of interest is the depletion regime which yields low dark conductivity.

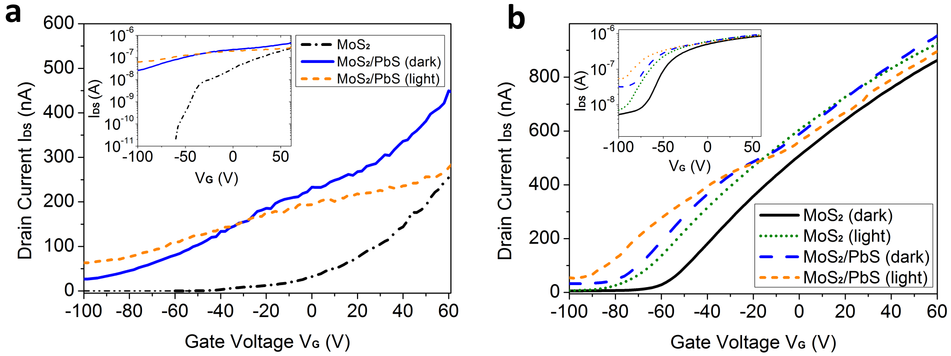

Figure 5.4: Transfer curves of MoS_2/PbS hybrids. Linear plot of the modulation characteristics under dark and illumintated conditions of a bilayer (a) and multilayer (>6 layer)(b) MoS_2 transistor. Both graphs show the transfer curves before and after PbS decoration. The inset shows the corresponding logarithmic plot of the drain-source current I_{DS} versus V_G. $V_{DS} = 50\,\text{mV}$

Figure 5.4 displays the field effect transistor characteristics of a bilayer (panel a) and multi-layer (panel b) MoS_2 transistor and its MoS_2/PbS hybrid device fabricated on a Si/SiO_2 substrate with SiO_2 thickness of 285 nm. All measurements are performed in a two-probe configuration and carried out under ambient conditions. The devices were measured before and after quantum dot deposition to directly compare the modulation behavior of the hybrid device to plain MoS_2. The I_{DS}-V_G transfer curves under bias voltage $V_{DS} = 50\,\text{mV}$ are presented in linear scale and logarithmic scale (inset). The bilayer MoS_2-only device shows large on/off ratios in the range of 10^5 - 10^6. For the multilayer device the on/off ratio is reduced since the field-effect gating affects the bottom layers more strongly and decreases in upper layers. After the deposition of QDs, both the thin and thick devices reveal similar doping behaviour. Under dark conditions, the threshold voltages shift to lower V_G, indicating a rather unexpected n-type surface-doping effect. The QD deposition leads to degenerate doping with significant loss of on/off ratio. This effect is more

pronounced in the bilayer case, as the surface-to-volume ratio increases for thinner MoS_2.

Under illumination, a peculiar gate-dependent photoresponse is found. The hybrid phototransistor exhibits positive photoconductivity at strongly negative V_G and negative photoconductivity after passing a certain backgate voltage crossover point. The positive photoconductivity at negative V_G is dictated by the band alignment of the MoS_2/PbS heterojunction that facilitates photo-generated electron injection from the PbS layer to the MoS_2. In the positive V_G regime the transfer characteristics are indicative of a mobility reduction of the MoS_2 channel upon photoexcitation evidenced by the decrease in the slope of the I_{DS}-V_G curve. A possible reason for this mechanism may be that, in the accumulation regime, the change of conductivity upon illumination is more sensitive to photo-induced changes in mobility. This could be due to increased charge scattering by the positive photo-charged PbS.

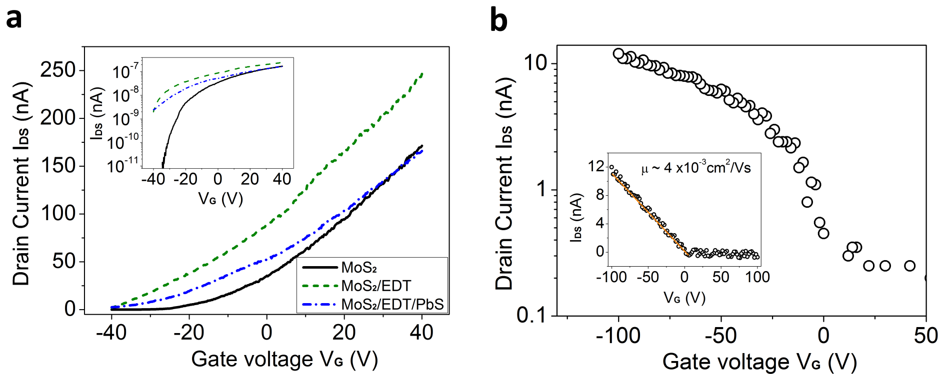

Figure 5.5: EDT doping effect and PbS reference transistor. (a) Linear and logarithmic (inset) plot of the modulation characteristics of bilayer MoS_2 right after fabrication, after EDT immersion and after PbS deposition. $V_{DS} = 50\,\text{mV}$. (b) Reference field effect transistor of p-type PbS quantum dots with similar channel dimensions as the hybrid devices. Bias 1V.

The unexpected electron-doping effect upon QD deposition and the loss of on/off ratio have a strong impact on the hybrid phototransistor performance and therefore merit further investigation. The large amount of sulfur vacancies in MoS_2 suggests that ligands with sulfur containing groups, such as EDT, possibly bind to unsaturated molybdenum sites. Therefore the impact of EDT on transistor performance was tested by soaking the sample briefly in an EDT-containing solvent prior to PbS deposition. After immersion in EDT, the MoS_2 layer becomes initially more n-type due to surface doping effects. The subsequent deposition of p-type

PbS QDs again turns the MoS_2 film less n-type doped due to the formation of the heterojunction between n-type MoS_2 layer and the p-type PbS QD film, as illustrated in Figure 5.5(a). The EDT coverage has no visible impact on carrier mobility, which, however, slightly decreases upon PbS decoration. This is possibly due to scattering effects at the interface.

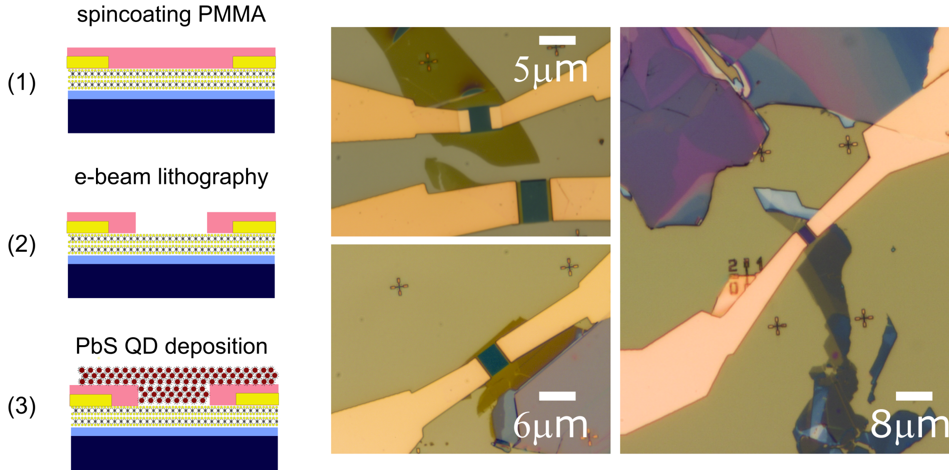

Figure 5.6: Isolation of PbS QDs from electrodes. The left column shows a step by step procedure to isolate the QDs from electrodes and residual surrounding flakes. On the right, several optical microscopy images of MoS_2 transistors covered with PMMA are shown, which have an exposed square "window" between the contacts after electron beam lithography (before quantum dot deposition).

Although the PbS solid has a much lower mobility than MoS_2, another reason for the increased off-currents might be the hole accumulation in PbS. A reference plain PbS-FET reveals the p-type hole transport at negative V_G (Figure 5.5(b)). In the hybrid device the accumulation of holes may subsequently increase the leakage current flowing through the QD film. To rule out any contribution of PbS to the drain current, several "window" samples, as displayed in Figure 5.6, were fabricated on which only the MoS_2 transistor channel gets exposed to quantum dots and its contact electrodes are isolated. To do so, a second electron beam lithography step is incorporated, which defines a little square inside the 150 nm thick PMMA film. The PMMA is hard-baked afterwards and the PbS QDs are spincoated on top of the device. The "window" can be fabricated within any insulating film (PMMA, SiO_2, Al_2O_3, etc.) to isolate QDs from the electrodes and to avoid leakage current through the PbS film. Devices with "windows", however, suffer from the same loss of on/off modulation as non-isolated devices. It is therefore evident that the change in modulation originates from doping or interface effects upon PbS deposition. This

challenge is addressed in Chapter 6 of this thesis.

5.3.2 Optoelectronic response and photocurrent dynamics

The hybrid MoS_2/PbS phototransistor combines two semiconducting material systems that are both responsive to illumination. To elucidate the origin of the photoresponse, the spectral responsivity is measured before and after QD deposition. Figure 5.7(a) shows the spectral responsivity of a MoS_2-only phototransistor. It exhibits responsivity of up to 5 A/W, and its spectral sensitivity is determined by the bandgap of the bilayer flake of around 1.8 eV. The hybrid detector shows dramatically higher responsivity of 10^5 A/W, and its spectral sensitivity is now extended to the NIR as dictated by the bandgap of the PbS QDs. Thus, hybrid detectors can be developed with spectral selectivity at even longer wavelengths, such as the SWIR or MIR, by choosing the appropriate QDs. This has been proven for larger PbS QDs with an excitonic peak at 1400 nm and responsivity beyond 10^4 A/W, as illustrated in Figure 5.7(b).

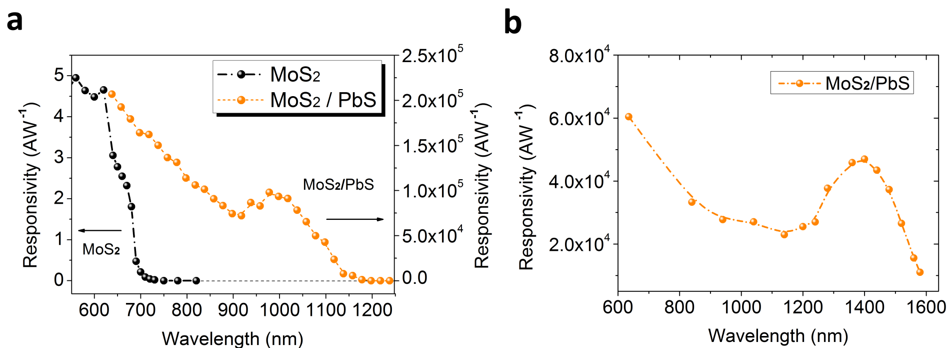

Figure 5.7: Spectral responsivity of MoS_2 and MoS_2/PbS hybrids. (a) Response to illumination as a function of wavelength of bilayer MoS_2 and its hybrid (with an active area of 15 μm^2). While the MoS_2 device absorbs only until a wavelength of ∼ 700 nm, the hybrid clearly follows the expected PbS absorption with an exciton peak at 980 nm. Apart from that, the hybrid detector shows dramatically higher responsivity of 10^5 A/W compared to the 5 A/W of the standalone MoS_2 detector. (b) The absorption onset can easily be tuned by controlling the quantum dot size to extend the spectral coverage of the hybrid device into the SWIR. The exciton peak of this device is at 1400 nm.

The responsivity of the detector is measured over six orders of magnitude of optical intensity showing significant dynamic range. The responsivity decreases with increasing optical intensity (Figure 5.8). At higher illumination intensities the increased number of separated charge carriers induces a reverse electric field,

effectively lowering the built-in field. Charge carrier recombination is therefore accelerated at the interface with the resulting drop in responsivity. In addition, saturation of sensitizing traps in PbS QDs from photogenerated carriers contributes to the decrease in responsivity.

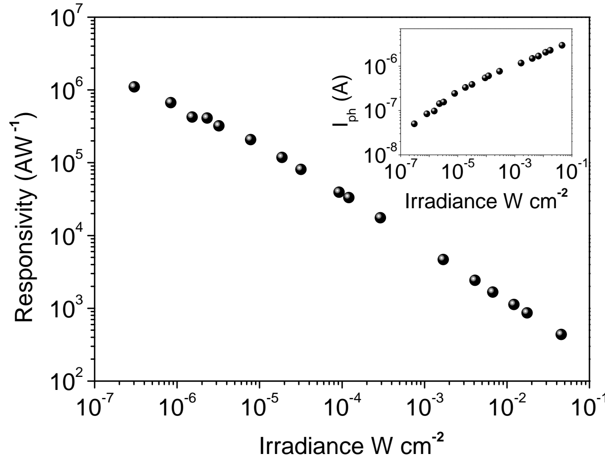

Figure 5.8: Power-dependent optoelectronic response. Responsivity of the hybrid device at a wavelength of 635 nm for different optical illumination intensities at an applied bias V_{DS}=1 V. The lowest detectable optical power leads to a responsivity of 10^6 A/W. Inset: photocurrent I_{Ph} in the OFF-state for different illumination intensities.

High photoconductive gain in this device originates from excellent transport properties in the MoS_2 channel. The underlying mechansim is sketched in Fig.5.9 (a). Once photo-generated electrons are extracted at one electrode, positive net charge remains in the QD solid. This causes another electron at the opposite electrode to be injected in order to maintain charge neutrality. The high electron mobility in MoS_2 yields a carrier transit time that is orders of magnitude shorter than the trapping lifetime in the quantum dots, resulting in multiple electron-circulation events, the number of which is given by $\tau_{lifetime}/\tau_{transit}$.

To eliminate the contribution from the PbS channel or surrounding residual MoS_2 flakes, hybrid control devices with isolated PbS QDs (as displayed before in Figure 5.6) were fabricated, which exhibit similar responsivity on the order of 10^5 - 10^6 A/W. Moreover, control devices with same channel dimensions and PbS QDs as the only photoactive material were fabricated. These plain PbS control detectors have orders of magnitude lower responsivity than hybrid devices due to the significantly lower carrier mobility of the QD solid. Based on this, we conclude that the reported responsivity is the result of the synergy between PbS QDs and

the MoS_2 layer.

The large gain influences the temporal response of the hybrid photodetector, which is also determined by the trapping lifetime. The longer the photogenerated holes remain in the QD solid, the higher the gain and the slower the device response will be. Independent of MoS_2 thickness, a decay time constant on the order of $\sim$0.3 s is measured (Figure 5.9 (b)). The obtained decay times of hybrid devices are at least one order of magnitude faster than those previously reported for plain MoS_2 phototransistors. Simultaneously hybrid responsivity outperforms plain MoS_2 references by a factor of 1000. Still the response times have to be improved for practical applications, for example, by trap-state engineering routes [135].

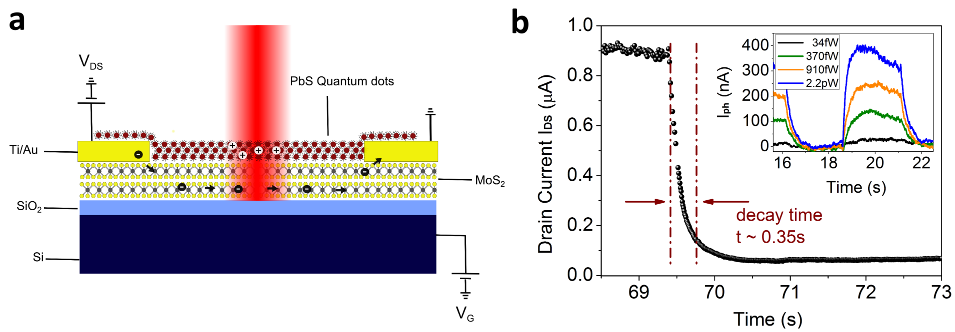

Figure 5.9: Gain mechanism and photocurrent dynamics. (a) Cross-sectional view of the device operation under illumination. While holes are trapped in the PbS volume, the electrons are transferred several times through the MoS_2 channel. The applied back-gate voltage V_G controls the current levels under illumination and in dark conditions to increase the hybrids photosensitivity. (b) The time-resolved photocurrent showed typical decay times of $\sim$0.3 - 0.4 s after switching off the laser. The inset shows pulsed photoresponse (I_{on}-I_{off}) over time for different illumination power.

To demonstrate the breakthrough improvement achieved by this hybrid architecture compared to the control devices based on MoS_2 and PbS QD alone, the key figures of merit are summarized in Table 5.1.

Table 5.1: Comparison of hybrid device performance with its single counterparts.

Device	Reference	Electric field [V/μm]	Dark current [A]	Spectral coverage [nm]	Responsivity [A/W]	Decay time [s]
MoS_2	[40]	0.4	2.5×10^{-8}	400-700	7.0×10^{-3}	0.05
MoS_2	[42]	8.0	2.0×10^{-12}	400-700	8.8×10^{2}	9
MoS_2	[41]	0.3	1.0×10^{-11}	400-900	0.12	–
PbS QDs	[this work]	1.0	3.0×10^{-10}	400-1500	4.3×10^{2}	0.02-0.03
MoS_2/PbS	[this work]	0.3	2.6×10^{-7}	400-1500	6.0×10^{5}	0.3-0.4

5.3.3 Backgate dependent sensitivity

The existence of a material with a bandgap in the channel of the transistor that allows the facile tuning of the dark conductivity is a powerful tool to increase the sensitivity of the detector. The use of the backgate as a knob to adjust the sensitivity of the MoS_2-PbS device is illustrated in Figure 5.10. The shot-noise limit is considered, as it is the noise component that is determined by the dark current of the photodetector. In this graph only the negative backgate range is taken into account, because the photoconductivity switches sign close to $V_G = 0$ V, and the dark current increases strongly in the accumulation regime for $V_G > 0$ V. At high negative backgate bias the MoS_2 channel is depleted from free carriers in the dark state, and therefore the detector has the potential to reach high sensitivity in the shot-noise limit with D^*_{SN} approaching 2×10^{14} Jones at V_G of -100 V and $V_{DS} = 1$ V. Note that the SiO_2 substrate thickness of this device is 285 nm, which allows backgate voltages up to 100 V. The detector is also tested at different applied biases. Significant performance is observed, with a corresponding responsivity of 10^3 A/W even at very low applied electric field of 3.3 mV/μm.

Figure 5.11(a) shows time traces of pulsed optical excitation of the detector at different backgate potentials to demonstrate the improved light-to-dark current ratio with increasing back-gate bias. The time-resolved photoresponse is measured at the same irradiance in all three cases. The gating effect improves the device sensitivity since the light response can clearly be distinguished from the lower dark

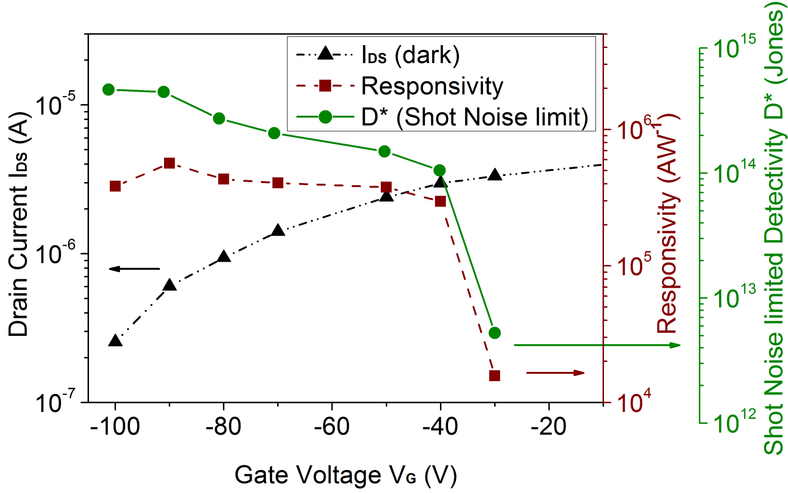

Figure 5.10: Hybrid photodetector device characteristics. Drain current I_{DS} (under dark conditions), responsivity R and the shot-noise limited detectivity D^* as a function of back-gate voltage V_G measured at $V_{DS} = 1$ V. The photoresponse was measured at 3 μW/cm^2 at all V_G except for V_G = -30 V, where the irradiance had to be increased to 90 μW/cm^2 to distinguish the signal from noise. The active area of the detector is 12 μm^2.

noise floor. While at -100 V even much lower irradiance levels could be sensed, the hybrid reaches its sensitivity limit for the gate-voltage -50 V at this incident light power.

To characterize the actual performance of the MoS_2/PbS hybrid, the spectral noise power of a device at applied negative backgate potentials is recorded. The measured noise in the dark current of the hybrid detector shows a strong 1/f component as it is observed for plain single and bilayer MoS_2 devices. With noise and responsivity acquired at a frequency of 1 Hz, this leads to noise equivalent power as low as 2×10^{-15} W Hz$^{-1/2}$ and 7×10^{-16} W Hz$^{-1/2}$ for bilayer and few-layer hybrids, respectively. The corresponding D^* values are 2×10^{11} Jones and 5×10^{11} Jones.

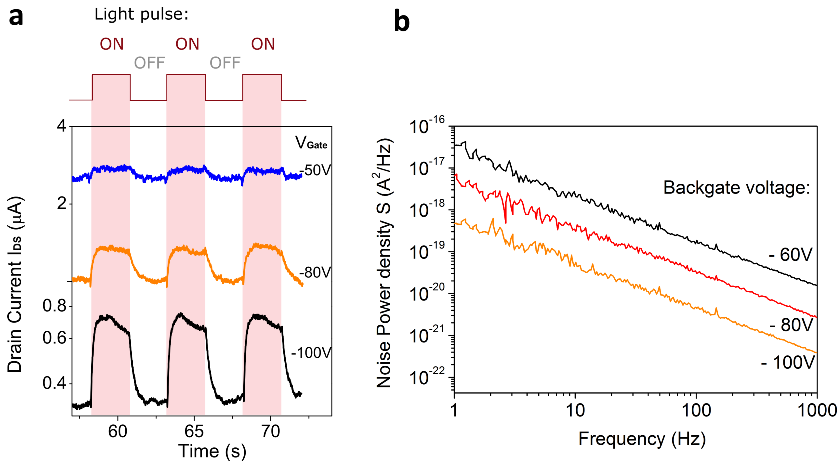

Figure 5.11: Gate-dependent signal-to-noise ratio. (a) The time-resolved photoresponse for three different back-gate voltages demonstrates how the hybrid device exhibits decreased dark current with stronger back-gate voltage. This effect improves the device sensitivity since low irradiance levels can be clearly distinguished from dark noise. (b) Noise power density of a typical MoS_2/PbS hybrid measured at different negative backgate voltages for a constant drain-source bias of 1 V. Independent of V_G, all traces are dominated by 1/f noise. With increasing gating strength the reduction of dark current leads to significantly lower noise.

5.4 Hybrid detectors based on other 2D and 0D systems

Although the proof-of-concept hybrid device based on MoS_2 and PbS shows results that are encouraging for further improvement, the extrapolation of the device concept to possibly integrate other material systems is of great importance. While MoS_2 is one of the most studied 2D semiconductors to date, the growing research efforts in the field may soon lead to the discovery of other materials with even better electronic properties. Also, the toxic lead component of PbS-based semiconductors has raised doubts for its application in commercial technology, and efforts have been made to develop non-toxic solution-processed QDs with similar properties. The rather simple fabrication procedure of hybrid phototransistors suggests straightforward integration of any 2D system with various 0D solution-processed nanocrystals.

Hybrids based on other TMDCs.
Other than MoS_2, WS_2- and $MoSe_2$-based hybrid transistors covered with PbS QDs have been investigated. The channel thickness of tested devices was between 10 - 20 layers, and two-terminal field-effect mobility in the range of 20 - 40 cm^2/Vs was obtained. Hybrid phototransistors based on $MoSe_2$ and WS_2 performed very similar to previous MoS_2 devices. The strong surface doping after PbS (EDT-treated) deposition likewise deteriorates the initially large on/off ratio, and upon light absorption ultra-high gain is generated, resulting in a responsivity of 10^5 A/W at lowest detectable power (Figure 5.12).

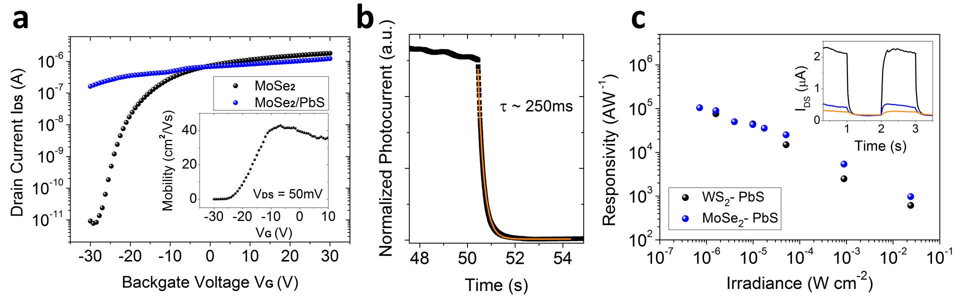

Figure 5.12: Hybrid PbS phototransistor based on $MoSe_2$ and WS_2. (a) Logarithmic plot of the I_{DS}-V_G modulation curves of $MoSe_2$ and $MoSe_2$/PbS under dark conditions. All tested $MoSe_2$ and WS_2 devices reached field-effect mobility of 20 - 40 cm^2/Vs. (b) Fall time of a light response of $MoSe_2$/PbS. The approximation with a single exponential function results in a time constant of 250 ms. (c) Responsivity of $MoSe_2$/PbS and WS_2/PbS devices as a function of irradiance. The inset plots the pulsed drain current I_{DS} over time for different illumination power.

Hybrids based on other QDs.
Apart from different channel layers, the sensitizing material is also widely selectable. PbS has many advantages, as pointed out in the first section of this chapter; however an often discussed drawback is the toxicity of the heavy metal lead. Non-toxic solution-processed $AgBiS_2$ QDs were therefore tested as sensitizers, as they operate comparably well in other optoelectronic devices, like solar cells.

Compared to PbS-based hybrid phototransistors, two distinct features are identified in the optoelectronic response of $MoS_2/AgBiS_2$ (see Figure 5.13). First, the gate-dependent drain currents under dark and illuminated conditions do not cross at any point, and conductivity is increased by light throughout the full backgate range. In addition, the response times around 10 ms are at least one order of magnitude faster than PbS-based hybrids. These findings suggest that the trap density and trap distribution of $AgBiS_2$ are distinct from PbS. If mainly shallow gap states dominate the trapping dynamics, the lifetime of trapped holes would decrease and

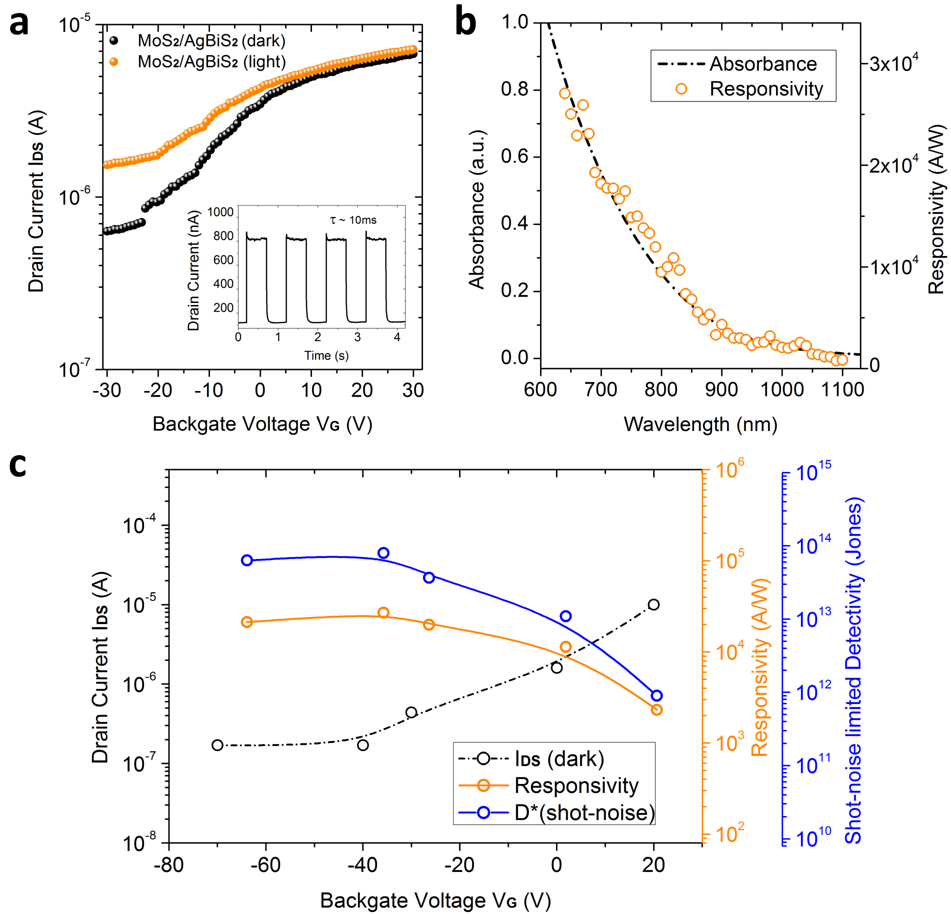

Figure 5.13: Hybrid MoS_2/$AgBiS_2$ phototransistor. (a) Logarithmic plot of the I_{DS}-V_G modulation curve of a MoS_2/$AgBiS_2$ hybrid under dark (black) and illuminated (orange) conditions. Compared to PbS-based hybrids, the $AgBiS_2$ hybrids respond to light with increasing conductivity throughout the full backgate range. In addition, the temporal response is faster by more than one order of magnitude (inset). (b) Absorbance and responsivity spectra of the hybrid device agree well and show enhanced absorption up to 1000 nm, dictated by the bandgap of $AgBiS_2$. (c) Dark current, responsivity and detectivity as a function of backgate voltage.

result in faster response and reduced gain.

The spectral responsivity is governed, as expected, by the absorption spectrum of $AgBiS_2$ due to the charge transfer of electrons into the MoS_2 channel upon illumination. Generally, the hybrid device characteristics follow a similar trend, with a highest measured sensitivity of 1×10^{11} Jones and a shot-noise limited sensitivity of 8×10^{13} Jones in the depletion regime. The maximum responsivity in the range of 10^4 A/W is about one order of magnitude lower than in PbS-sensitized devices. This is again in agreement with the picture of reduced carrier lifetime and gain, and points to different trapping behavior than in PbS.

5.5 Summary and outlook

Colloidal quantum dots are an interesting platform to combine with 2D materials for hybrid optoelectronic devices. Features like low-cost solution processing, facile integrability with 2D systems and spectral tunability make them highly attractive for sensitive hybrid phototransistors. The earlier discussed drawbacks of plain MoS_2 detectors can easily be overcome after hybridization with PbS. The spectral selectivity is then dictated by the tunable bandgap of PbS and adds another degree of freedom for its possible use in UV-SWIR detection simply by choosing the appropriate QD size. Calculating the quantum efficiency from the measured responsivity and the estimated gain (as done in chapter 4) yields values of up to 20 %. It is noteworthy that this quantum efficiency value is just a rough estimation, as it relies on parameters, like carrier mobility, which are not accurately determined in 2-terminal measurements. However, as the estimation procedure is the same for plain MoS_2, it serves to emphasize the improvement of quantum efficiency in hybrid systems by a factor of 1000, when compared to neat MoS_2 photodetectors.

The obtained detectivity of 10^{14} Jones in the shot-noise limit underpins the huge potential of the hybrid technology. Yet, the measured detectivity of 5×10^{11} Jones points out that the device performance needs further optimization. MoS_2-based hybrids suffer from large inherent noise especially in the low-frequency region (1/f noise). Further improvement towards the shot-noise limit can be expected by optimization of the metal contact/semiconductor interface to reduce contact resistance, as well as investigation of the noise contribution of the edges of the 2D material. Apart from that, the most puzzling and adverse behavior of all investigated TMDC-based hybrids is the degenerate doping and subsequent loss of effective gate-voltage modulation upon QD deposition. This leads to large dark currents in the off-state of the device and is the main factor that inhibits high sensitivity.

The hybrid device has been proven to be a versatile platform applicable to various other 2D or QD materials. As demonstrated in the case of $AgBiS_2$, the change of trap distribution and density within the sensitizing material can readily lead to changes in carrier dynamics. This motivates investigation of other material systems and trap state passivation schemes for higher bandwidth operation. The versatile incorporation of any solution-processed QDs is one of the strongest features of this hybrid detector design. In the MIR wavelength regime, for instance, conventional technology is made of expitaxial InSb and HgCdTe, which are extremely expensive and require cooling for high performance [119]. The synergy of 2D materials with MIR-sensitive QDs, such as HgTe, therefore constitute a compelling alternative to epitaxially-grown state-of-the-art detectors and deserve investigation.

6

Interface engineering in hybrid TMDC-QD phototransistors

In chapter 5, the hybridization of 2D TMDCs with colloidal quantum dots has been proven to be an ideal platform for highly sensitive photodetection due to large carrier multiplication producing gain. However, TMDCs respond sensitively to surface modifications, and the sensitizing quantum dots have introduced uncontrolled doping and interface effects which prevent these hybrids from maintaining the characteristically large on/off ratios of TMDC transistors. Chapter 4 has shown that TMDCs are susceptible to many extrinsic effects, and the transport properties of 2D materials can be preserved and even improved by encapsulation strategies.

Here, the findings of previous chapters are combined in a novel hybrid device architecture with a semiconducting titanium dioxide (TiO_2) passivation layer at the interface between MoS_2 and PbS QDs. This buffer-layer encapsulates the MoS_2 transistor and preserves the field-effect modulation by suppressing the high density of localized sub-bandgap states introduced after QD deposition which pin the Fermi level. The interlayer maintains gate control over carrier density in the channel and allows for low noise operation. Furthermore, by choosing a semiconducting passi-

vation film, effective charge separation and transfer occurs at the interface, and a quantum efficiency of up to 28 % is reached. The photoconductive gain can be tuned with gate voltage, yielding a responsivity of 10^3 - 10^5 A/W and specific detectivity of 10^{12} - 10^{13} Jones, more than one order of magnitude of improvement compared to the MoS2/PbS control. The present methodology discloses an encouraging path to control interface and degenerate doping effects of 2D crystal-based hybrid devices.

6.1 Device concept and electrical properties

Despite the large bandgap of 1.2 - 1.8 eV in few-layer MoS_2, the initially high on/off ratio gets significantly reduced upon sensitization with PbS QDs. The devices show relatively large dark currents of 10 - 100 nA, several orders of magnitude above those of high-quality MoS_2 transistors. The atomically thin profile renders TMDCs extremely sensitive to surface modifications. Controlled doping strategies still remain poorly understood and form one of the most challenging tasks for 2D-based optoelectronics. Various different approaches based on molecular doping [53–55, 81, 136], substitutional doping [76, 137], chemical surface treatment [138, 139], adsorbate doping [90], SAM functionalisation [56], plasma-assisted doping [140, 141] and strong bonding to defect sites [57, 142] have been employed. However, most of them cause either degenerate doping with metallic behavior or strongly reduced electrical gate-modulation, as in the case of MoS_2/PbS. While degenerate doping is useful for high quality contact formation with reduced resistance [55], the loss of on/off ratio is detrimental for optoelectronic performance of hybrid phototransistors.

Recently, it has been shown that defect sites, such as sulfur vacancies, play a major role in MoS_2 doping, as they offer connecting links for organic functional groups [57]. In optoelectronic heterojunctions, this can lead to a fundamental trade-off: for one, hybrids rely on strong electrical coupling at the interface for efficient charge transfer. To this purpose, defect sites can be useful to adhere organic functional groups and crosslink with sensitizers. However, the direct crosslinking of sensitizers at defects may also lead to aforementioned uncontrolled doping effects, increased charge scattering or a high density of localized states, which affect the field-effect modulation efficiency and charge transport of the hybrid.

6.1.1 Fabrication of MoS_2/TiO_2/PbS

To form efficient heterojunctions and support the charge transfer between MoS_2 and PbS without compromising its unique electronic transport properties, a thin semiconducting TiO_2 film is incorporated at the interface. Standard MoS_2 field effect

transistors with a variety of channel thickness from 1 to 10 layers and dimensions in the range of 30 - 50 μm^2 were fabricated on Si/SiO_2 substrates with oxide thickness of 90 nm. Figure 6.1 shows a sequence of device fabrication steps from left to right that include MoS_2 FET fabrication with Ti/Au contacts, ALD deposition of a thin oxide buffer-layer and final spincoating deposition of the QD film. After test

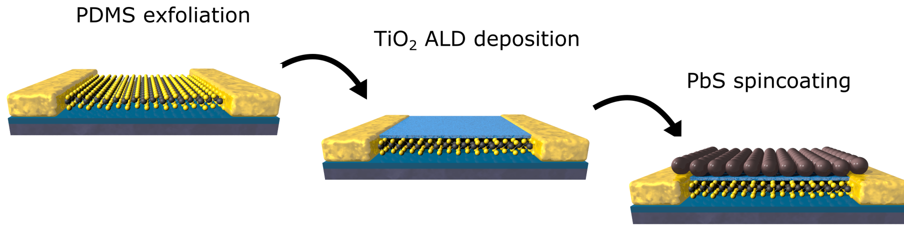

Figure 6.1: Sequence of MoS_2/TiO_2/PbS device fabrication. Device architecture after each fabrication step. Few-layer MoS_2-FETs are fabricated by PDMS-tape exfoliation and standard lithography, the TiO_2 film is deposited by atomic layer deposition and colloidal quantum dots are spincoated in a layer-by-layer process.

measurements of plain MoS_2 FETs in ambient conditions, devices were covered by TiO_2 with the atomic layer deposition technique. Prior to deposition, the samples are annealed in nitrogen atmosphere in the ALD chamber at 200°C for around one hour to remove surface-bound adsorbates. As shown in chapter 4, the encapsulation with isolating oxides such as HfO_2 or Al_2O_3 in a high temperature process alters electronic performance by boosting mobility, reducing hysteresis and increasing device on-currents.

For interface passivation the semiconducting oxide TiO_2 is chosen because it not only serves as a protection layer, but also acts as an efficient electron transport medium between MoS_2 and PbS. The large bandgap of 3.2 eV further ensures that TiO_2 has no impact on the optical properties of the device in the vis/NIR, as its absorption is limited to UV radiation. The thickness of the TiO_2 film was varied from 5-40 nm, but no clear influence in this range on final photodetecting device performance or on/off ratio was observed. A standard thickness of 25 nm is therefore used for this study. TiO_2 is a well-studied n-type semiconductor often used in solar cells to form an effective p-n-junction with colloidal PbS QD films [122, 143, 144]. In the last step of the fabrication process, the PbS quantum dots are spincoated from solution in a layer-by-layer technique with EDT-exchanged ligands up to a thickness of 80 - 100 nm.

6.1.2 Transport and doping

To evaluate the electrical performance of the new device design, the transfer curve I_{DS}-V_G is investigated. Figure 6.2 summarizes the modulation curves of a 5-layer thick MoS_2 device after each fabrication step, measured under bias voltage of 1 V. From previous results it is known that encapsulation with oxides can lead to n-type doping effects, which has been ascribed to the removal of adsorbates and to the presence of oxygen vacancies in non-stoichiometric oxide films that create donor states close to the conduction band. A similar electron doping effect upon encapsulation with ALD-deposited TiO_2 is observed, indicated by the shift of threshold voltage towards more negative V_G.

Although the ALD-deposited TiO_2 film is in contact with the gold drain- and source-electrodes, a negligible current leakage through the oxide film is observed. The low mobility of the non-stoichiometric TiO_x and a non-ohmic alignment to gold contacts effectively prevent the current flow through the oxide. The FET characteristics of pristine MoS_2 are mostly maintained, and slightly elevated off-currents of 100 pA are reached. The increase in off-current is independent of TiO_2 thickness up to 40 nm, suggesting that the off-current does not stem from leakage through the TiO_2 film, but rather from electron doping at the interface.

Upon deposition of p-type PbS QDs on top of the encapsulated channel, the threshold voltage clearly shifts back again, indicating a doping compensation effect of the MoS2/TiO2 hybrid as a result of the formation of the heterojunction. This leads to a drop of dark currents in the depletion regime to a few tens of pA. In the linear regime, under a low bias of 100 mV, the two-terminal field-effect mobility is estimated and shows only minor changes at all hybrid stages, ranging from 22 - 25 cm^2/Vs.

6.2 Fermi level pinning at the interface

To understand the effect of the oxide buffer-layer, the device characteristics have to be compared with MoS_2/PbS devices where the interface is not protected, referred to as control devices. In Figure 6.3(a), typical modulation curves of control devices are plotted before and after hybridization. In the previous chapter, the loss of modulation in the control device has been associated with strong doping effects, where dithiol ligands initially n-type dope MoS_2 strongly, and the addition of p-type PbS reversed the doping effect. Just recently, it was shown that thiols can be used for doping TMDCs, as the sulfuric component chemically interacts with sulfur-vacancy defect sites in the MoS_2 surface [57]. Depending on polarity of the functional group,

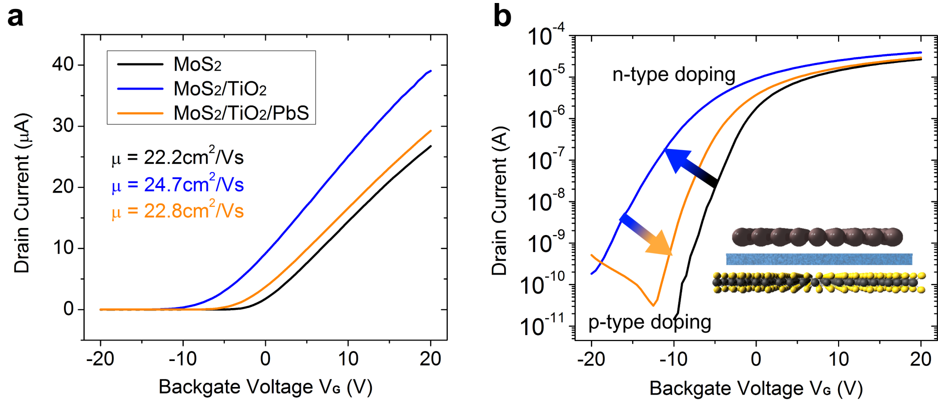

Figure 6.2: FET characteristics of $MoS_2/TiO_2/PbS$. The transfer curves for all stages of fabrication are plotted in linear (a) and logarithmic (b) scale. The shift of threshold voltage indicates clear n-type and p-type doping after TiO_2 and PbS deposition, respectively. The two-terminal field-effect mobility is estimated to 22 - 25 cm^2/Vs and shows only minor changes at all hybrid stages. $V_{DS} = 1$ V.

the doping effect can either be p- or n-type. In the case of MoS_2/PbS hybrids, the dithiols fill these defect sites and crosslink to PbS quantum dots, causing a strong charge transfer. Although doping plays a role in hybrid devices, it is, however, not the dominant mechanism behind the clear loss of modulation. When the defect-rich MoS_2 surface connects to PbS QDs, a detrimental side-effect of the direct cross-linking is a large density of localized states within the bandgap of the 2D material, as displayed in Figure 6.3(b). As a consequence, the Fermi level (E_F) is pinned, and the modulation via backgate voltage is reduced to on/off ratios of 10^2. The pinning effect on FET characteristics is clarified in Figure 6.3(c). Despite the high applied gate voltage, the hybrid control device cannot be switched off entirely, and a considerable amount of current is still induced into the channel. Additionally, the on-current flow in the accumulation regime is clearly reduced compared to its plain MoS_2 counterpart, attributed to the Fermi level pinning below the conduction band edge.

The phenomenon of Fermi level pinning can be quite problematic in low dimensional semiconductor devices. MoS_2 is known to be prone to such effects at semiconductor-metal interfaces [78, 145], where the pinning prevents ohmic contacts to be formed and eventually leads to high contact resistance. Little effort has been done, to date, to circumvent the pinning effect for metal contacts. A typical method to avoid Fermi level pinning is to passivate the interface traps with a thin oxide layer. The passivation of the MoS_2 contact areas with Al_2O_3 [146] or TiO_2 [147] has been shown to produce lower contact resistance.

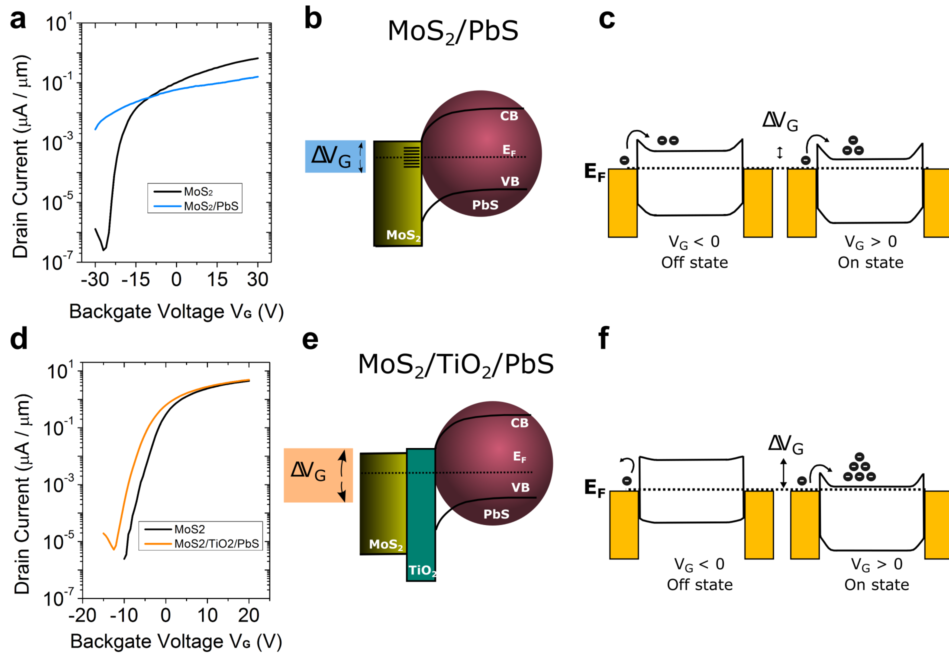

Figure 6.3: Modulation model and Fermi level pinning. (a) Transfer curve of a typical MoS_2/PbS control device. The on/off ratio of the standalone MoS_2 device is strongly reduced after PbS deposition. (b) Band alignment of MoS_2 and PbS in direct contact. The crosslinking with dithiol ligands creates a high density of localized sub-bandgap states in MoS_2 that pins E_F and reduces gate tunability to a small range ΔV_G. (c) Band diagram of the MoS_2-channel after PbS deposition with a Shottky barrier at the contact regions. The FET-channel can neither be sufficiently switched off (off-state) nor fully turned on (on-state) due to the reduced E_F control by backgate voltage. Panel (d)–(f) show the same model for the case of interface protected MoS_2/TiO_2/PbS hybrids. The on/off ratio is now largely maintained because of an effective passivation of the interface region. The control of E_F is preserved leading to low off-state current injection and high on-state current flow.

Figure 6.3(d) shows that with a thin TiO_2 film at the MoS_2/PbS interface low off- and high on-currents close to initial MoS_2 values are obtained in the depletion and accumulation regime, respectively. The regained backgate control of E_F leads to efficient channel depletion and accumulation, illustrated schematically in Figure 6.3(e) and (f).

Several devices of similar channel dimensions, with protected and unprotected interfaces, are compared and demonstrate highly reproducible results, as summarized in Figure 6.4. All tested control devices possess strongly reduced on/off ratios of only 10^2 with relatively large off current density in the range of 10 - 100 nA/μm at the strongest possible gating just before breakdown of the underlying SiO_2. The new device architecture MoS_2/TiO_2/PbS however largely retains its FET properties, and the on/off ratio is improved by more than 2 orders of magnitude compared to control devices.

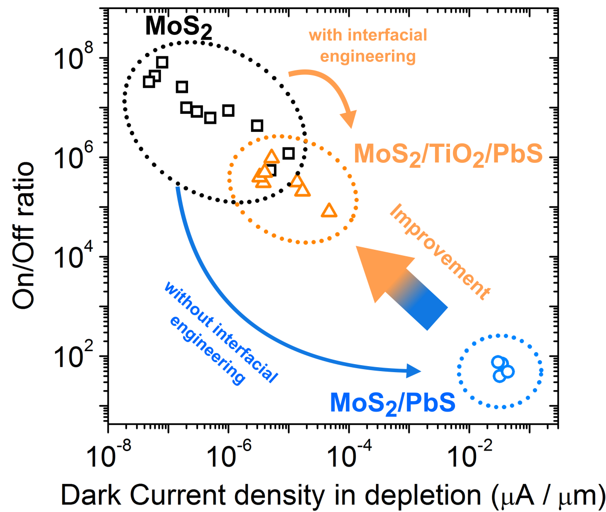

Figure 6.4: Transistor operation improvement after interface engineering. On/off ratio versus dark current plotted for many tested devices in their depletion regime. Initially obtained ratios of 10^6 - 10^8 for standalone MoS_2 are strongly reduced to 10^2 for MoS_2/PbS control devices (blue arrow) and only slightly decreased to 10^5 - 10^6 for interlayer protected MoS_2/TiO_2/PbS devices (orange arrow). Likewise, dark currents are strikingly decreased by around 3 orders of magnitude after implementation of the buffer-layer.

6.3 Gate-dependent photoresponse and sensitivity

In the previous chapter on MoS_2/PbS devices, a gain mechanism generated multiple electrons per single absorbed photon. Also, the backgate dependent light response of the MoS_2/PbS hybrid has shown quite peculiar behavior with a change of sign from positive photoresponse (depletion regime) to negative response (accumulation regime). Figure 6.5(a) shows the modulation curves of the interface-passivated MoS_2/TiO_2/PbS under dark and illuminated conditions for different powers. Here, the TiO_2 encapsulation maintains the positive photoresponse throughout the full gate voltage range. The oxide buffer-layer separates the electron-accumulating MoS_2-channel from the positively photo-charged PbS QDs and may thereby inhibit the earlier proposed charge scattering and mobility reduction under light. As depicted in the inset panel, the large bandgap interlayer also rules out the possibility of hole injection from PbS into MoS_2, as well as trap-assisted recombination at the interface, both plausible mechanisms that may have caused the sign switch of photoresponse in MoS_2/PbS devices.

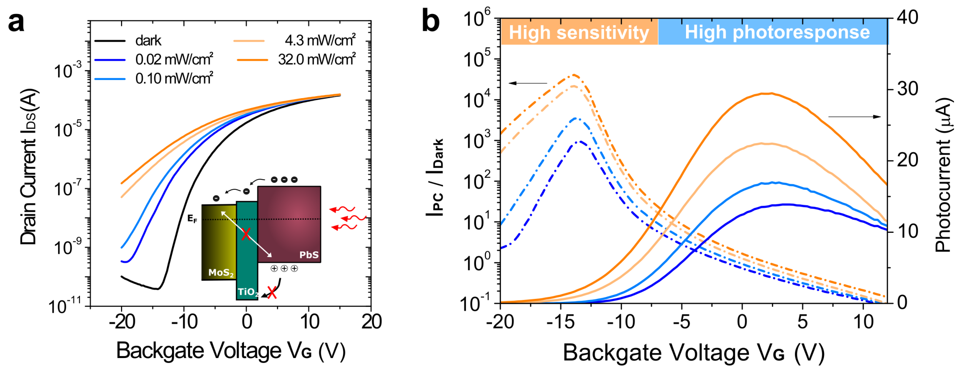

Figure 6.5: Backgate dependent photoresponse. (a) Transfer curves of a hybrid MoS_2/TiO_2/PbS device at different illumination intensity specified in the legend. The small inset illustrates the electron charge transfer mechanism after photoexcitation due to well aligned conduction bands. Holes stay trapped in the PbS film as they can neither surpass the large TiO_2 barrier nor recombine with electrons in the MoS_2 channel. (b) Backgate dependent photocurrent (right axis) and singal-to-noise ratio defined as the ratio of photocurrent to dark current (left axis). Despite displaying the strongest light response above the threshold voltage ($V_G \sim 0$ V), the highest sensitivity of the device is reached in the depletion regime ($V_G \sim$ -15 V).

The photocurrent I_{PC}=I_{Light}-I_{Dark} versus backgate voltage for different illumination intensities (Figure 6.5(b)) shows strong modulation with V_G and a clear maximum can be identified between 0 V and +5 V. The strongest response corresponds to the region with highest transconductance of the FET device, as already observed for standalone MoS_2 detectors [148]. The Fermi level alignment in this region is favorable for low contact resistance operation and ideal for many cycles of electron circulation to produce maximum gain. Yet, in this region the hybrid also operates at high dark currents, and therefore a more important figure of merit is the signal-to-noise ratio (SNR). In the same panel Figure 6.5(b) the SNR defined as I_{PC}/I_{Dark} is illustrated and points out the phototransistors' potential for highest sensitivity in its depletion regime at V_G of -12 V to -15 V. Here the lowest dark current and maximum sensitivity are achieved, despite the devices' concurrent drop in photocurrent.

To investigate in greater detail, the power dependent responsivity in the two distinct regimes of operation, at 0 V and -15 V (Figure 6.6(a)), is acquired. At both gate voltages the measured responsivity dropped with increasing power because of saturation of sensitizing traps in PbS QDs and shows a responsivity of 10^3 A/W and 10^5 A/W at around 10 nW/cm^2. This is a characteristic footprint of trap-dominated photoresponse already seen for the MoS_2/PbS control devices, where the ratio of the longer lifetime of minority carrier ($\tau_{lifetime}$) to the short transit time of the majority carrier ($\tau_{transit}$) produces internal photoconductive gain. The decay process can be approximated by a first-order exponential relaxation function (see Figure 6.6(b)). For a light pulse measured at 67 nW/cm^2 and $V_G = -15$ V, a time constant of $\tau_{decay} = 12$ ms is extracted, and with increasing illumination power the device response accelerates. Compared to MoS_2/PbS hybrids without interface passivation, the temporal response is now significantly faster. The enhancement of time response is attributed to the removal of surface-bound H_2O molecules during the annealing and encapsulation process of MoS_2 with the TiO_2 film. From the responsivity and corresponding response times measured at $V_G = 0$ V, a quantum efficiency around 28 % is extracted, which indicates efficient charge transfer from PbS to MoS_2.

The purpose of the TiO_2 interlayer in the MoS_2/TiO_2/PbS hybrid is two-fold, as it avoids the creation of high trap state density at the interface and prevents the pinning of E_F, but also allows charge transport between MoS_2 and PbS. To verify the actual charge transfer mechanism between PbS and MoS_2, the spectral response is measured at $V_G = -15$ V (Figure 6.6(c)). The curve clearly follows the absorption spectrum of the sensitizing QDs, with an exciton peak at 965 nm. Along with the

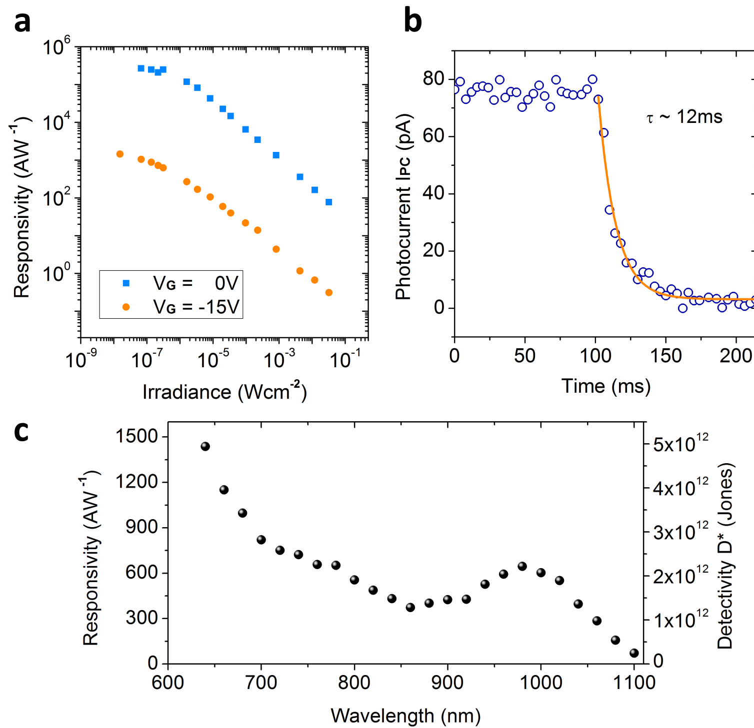

Figure 6.6: $MoS_2/TiO_2/PbS$ phototransistor properties. (a) Power dependent responsivity measured in the highly sensitive (-15 V) and highly responsive (0 V) regime. $V_{DS} = 1$ V. (b) Fall time of a light response at 67 nW/cm^2. The approximation with a single exponential function results in a time constant of 12 ms. (c) Spectral responsivity (left axis) and detectivity (right axis) reveal a highly sensitive hybrid system with light absorption in the quantum dot thin film. The sensitivity of the hybrid system exceeds 10^{12} Jones over the whole vis/NIR spectral range.

findings from Figure 6.6(a), it is evident that photons are absorbed within the QD film, and charge carriers are subsequently transferred into the MoS_2 channel, where the magnitude of internal amplification can be tuned with FET-channel conductance.

To assess the sensitivity of $MoS_2/TiO_2/PbS$ hybrid devices, the noise spectral density is recorded at both gate voltages (see Figure 6.7(a)) and the spectral detectivity at 1 Hz bandwidth is calculated. In the highest SNR regime at around -15 V, the hybrid device reaches a specific detectivity of 5×10^{12} Jones in the visible and exceeds 10^{12} Jones throughout the NIR wavelength range, measured at very low applied electric fields of only 0.2 V/μm (Figure 6.6(c)).

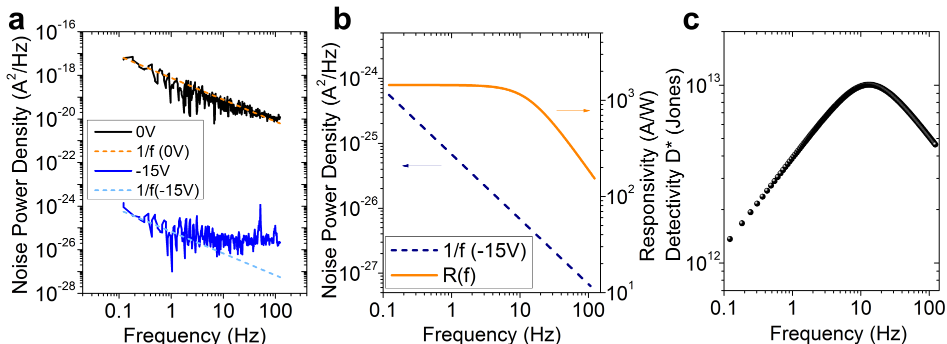

Figure 6.7: Noise spectra and detectivity estimation. (a) Measured noise power density and fitted 1/f curves at two backgate voltages, 0 V and -15 V. (b) Calculated responsivity and approximated 1/f noise spectral density at V_G = -15 V. (c) Estimated frequency dependence of D^* shows a maximum detectivity of 1×10^{13} Jones at $\sim$12 Hz.

The dominant 1/f noise component and the fast response of the device point to even higher sensitivity at higher frequencies. To predict the potential sensitivity of the device at higher frequencies, the noise power densities for both regimes at V_G = 0 V and V_G = - 15 V are approximated with theoretical fits (see Figure 6.7(a)). For V_G = 0 V, a good approximation with a 1/f curve is achieved, in agreement with previously reported 1/f noise for MoS_2 [109, 149]. The blue curve for V_G = - 15 V shows a similar 1/f trend at lower frequency up to a few Hz as seen for 0 V. However, at higher frequencies the measurement is limited by the white noise of the setup and the spectrum starts to flatten out. Therefore the frequency dependent $D^*(f)$ in the depletion regime can only be theoretically estimated, by using the fitted 1/f

curve at $_{G}$ = - 15 V and the calculated frequency-dependent responsivity

$$R(f) = \frac{R_0}{\sqrt{1 + (2\pi f \tau)^2}} \tag{6.1}$$

where R_0 is the measured d.c. responsivity and τ the measured decay time. This simple approximation of frequency-dependent noise and responsivity suggests potential detectivity up to remarkable 10^{13} Jones at a frequency of 12 Hz (see Figure 6.7(b) and (c)). The shot-noise estimated detectivity of 3×10^{14} Jones agrees well with previous values for MoS_2/PbS control devices. The sensitivity after interface engineering has therefore significantly approached the theoretical upper-limit given by the shot noise. In the highly responsive regime at $V_G = 0$ V the sensitivity D^* decreases as expected to 3×10^{11} Jones, due to the larger dark and noise currents. The novel hybrid phototransistor with an engineered interface shows improved sensitivity by more than one order of magnitude compared to its control device.

6.4 Summary and outlook

To conclude, a thin oxide buffer-layer has been successfully incorporated at the heterojunction of a 2D dichalcogenide and an absorbing sensitizer. In a proof-of-concept device, consisting of a MoS_2-PbS QDs hybrid phototransistor, defect sites present at the interface are passivated with a thin semiconducting TiO_2 layer, and the device thereby retains electrical control of its FET characteristics. The interlayer avoids the formation of a high density of localized states in the sub-bandgap region that pin the Fermi level and significantly hamper current modulation, as is the case for unprotected MoS_2/PbS devices. With this passivation scheme an improvement in modulation by more than 2 orders of magnitude is achieved, approaching the initial MoS_2 on/off-ratios. Moreover, the buffer-layer at the junction serves as efficient charge separation and transport layer leading to a quantum efficiency of up to 28 %. The demonstrated phototransistors show excellent performance parameters with a detectivity of 10^{12} - 10^{13} Jones in the vis/NIR and a temporal response ≤ 12 ms. This is more than an order of magnitude improvement in sensitivity and speed compared to control devices. This method presents a new route to engineer the interface between 2D materials and strongly absorbing semiconductors to form efficient heterojunctions without losing the unique electrical properties of the 2D

material.

Towards the goal of even higher quantum efficiency, knowledge from advances made in intensively studied PbS solar cells can be helpful. For instance, the usage of different capping ligands for several QD layers can engineer the band alignment in a way to extend the depletion width within the QD film [150]. A cascade-like alignment of the conduction band would thereby improve the electron transfer towards the TMDC-QD junction and increase the charge collection efficiency, allowing thicker QD films with higher absorption. Apart from ALD-deposited thin films, the exploitation of molecular self assembled monolayers at the interface may also lead to efficient crosslinking between QDs and TMDCs and simultaneously passivate electronic defect states at the TMDC surface [151–153]. The passivation mechanism shown in this chapter is one of many options to gain better control over interface and doping effects in 2D crystal-based heterostructures and can be useful for a wide range of applications.

Conclusion

The extensive research on graphene and other layered materials has advanced the field of 2D materials rapidly. Their unique electronic and optoelectronic properties, flexibility, and ultimate scalability down to single atomic layers are of great interest from a scientific as well as technological point of view.

In optoelectronic technology, photodetectors are of paramount importance, and the growing diversity of application areas demands new material systems and device designs. These need to meet basic requirements such as high sensitivity, fast response, and low-cost manufacturing, as well as add new functionality such as tunable spectral selectivity, mechanical flexibility or even partial transparency. This work has focused on 2D transition metal dichalcogenides, where the thickness-dependent bandgap allows for absorption in the vis/NIR and the atomically thin body provides low dark current operation for high sensitivity photodetectors. Prior to this work, some fundamental roadblocks had inhibited the exploitation of the properties of TMDCs for photodetectors:

Stable detector performance

The enormous variation in performance parameters reported for monolayer MoS_2 detectors is due to the extreme sensitivity to extrinsic factors, such as atmospheric adsorbates, on device operation, and is a major roadblock towards potential large scale manufacturing. Moreover, despite the large responsivity values reported in neat TMDC photodetectors, the slow response is impractical for most applications. In this thesis a simple encapsulation method has been developed to avoid uncontrolled extrinsic charge trapping, which deteriorates electrical transport and prolongs carrier lifetime. The removal of atmospheric molecules and introduction of surface

protection has led to high sensitivity of 10^{11} - 10^{12} Jones and response times of 10 ms. This is orders of magnitude faster than other sensitive MoS_2 detectors with gain. This methodology also served to eliminate undesired hysteresis effects and render the detectors more robust towards environmental exposure.

Spectral limitation and low absorption

The low absorption of atomically thin materials is perhaps one of the biggest challenges in 2D-material-based photodetection. Moreover, the large bandgap of MoS_2 has spectral selectivity limited to the visible. Even though some sensitivity extends into the NIR region with an increasing number of layers, the indirect bandgap of few-layer MoS_2 absorbs light inefficiently. In this work, this challenge has been successfully addressed by sensitizing MoS_2 with strongly absorbing PbS QDs in a hybrid TMDC-QD phototransistor. The decoupling of absorption and transport in two different material systems yields an ultrahigh gain of 10^6 electrons per absorbed photon, which is a strong basis for sensitive detection.

Selective interface engineering has been implemented to preserve control of field-effect modulated dark current and to strongly reduce noise. As a result, high detectivity of 10^{12} - 10^{13} Jones has been obtained, along with a 12 ms response time, sufficient for many imaging applications. The absorption efficiency and spectral sensitivity of this novel hybrid phototransistor are determined by the QDs, and can thus be tuned by making use of the quantum size effect. A spectral tunability with PbS QDs of different sizes has been demonstrated with high sensitivity into the SWIR.

Outlook

The sensitivity of plain MoS_2 phototransistors approaches values of conventional silicon-based photodiodes [124] in the visible. The flexible and transparent character of MoS_2-based devices is highly promising for application in bendable device concepts, for which bulky and brittle silicon is not compatible. Hybrid 2D-0D systems on the other hand have already shown sensitivity on par with detector technology based on silicon and InGaAs for the vis-SWIR range and have the potential to clearly outperform their detectivity. The variety of combinations of 2D channel materials and QD sensitizers allows application-specific tuning of the wavelength region of interest. Hybrid 2D-0D systems are therefore particularly interesting for spectral windows like the SWIR or MIR, which are only accessible with complex and costly expitaxy-based systems to date.

The major strength of 2D material phototransistors is the high in-plane charge

carrier mobility and potentially low dark current given by its thin channel body and efficient capacitive control over carrier density by means of the electric field effect. The choice of material system, for plain detectors as well as hybrid detectors, will therefore play a critical role for further development. Reported mobilities for commonly investigated 2D materials are widespread and a trade-off is met between mobility and bandgap [73, 154], which in turn determines the on/off ratio. Two popular examples are graphene, with average mobilities of $10^4\,\mathrm{cm^2/Vs}$ and on/off ratios of 10, and MoS_2, with mobilities of $60\,\mathrm{cm^2/Vs}$ and on/off ratios of 10^8 [155]. Black phosphorus is an interesting candidate between these two extreme cases. The combination of mobility up to $1000\,\mathrm{cm^2/Vs}$ and on/off ratios of 10^4 - 10^5 [156, 157] is intriguing for its application in hybrid phototransistors to achieve high gain-bandwidth product and sufficiently low off currents.

For both device concepts, wafer-scale manufacturing and successful implementation with integrated circuits for signal read-out will determine its prospect for commercialisation. The monolithic integration with existing silicon-based CMOS technology has already been proven for colloidal QDs [158, 159] and for graphene [160, 161]. Other layered material systems such as the TMDCS are expected to benefit from the rapid advances made in graphene technology. A further step will be the development of 2D material-based CMOS technology in which all essential circuit components comprise layered materials [162, 163]. 2D-material-based ICs are promising for high-density manufacturing and low-power operation, and their integration on soft substrates would open the door for new designs of all-2D-material-based flexible photodetectors.

To conclude, in this work two viable routes have been introduced to stabilize and to improve the light sensing ability of 2D-based phototransistors. Both device concepts are competitive with state-of-the-art photodetecting systems, add further functionality and have the potential to create a new generation of photodetectors. On a broader scale, this work introduced the concept of a heterojunction formed between 2D layered materials and QDs, paving the way towards new device concepts based on such architectures that go beyond photodetection, including hybrid 2D-QD solar cells and light emitting diodes.

Materials and methods

In this chapter the recipes used to fabricate TMDC-based photo-FETs and hybrid TMDC-QD devices are briefly described and the methods to characterize material quality and to measure the optoelectronic performance are summarized.

Field effect transistor fabrication

MoS_2 flakes of different thickness were micromechanically exfoliated with PDMS tape on pre-cleaned degenerately doped silicon substrates covered with a SiO_2 oxide of either 90 nm or 285 nm thickness. Metal contacts were fabricated by means of laser writer lithography or electron beam lithography, followed by electron beam and thermal evaporation of Ti (2 nm) and Au (50-100 nm), respectively. The samples were then annealed in vacuum for 12 h at $\sim 130°C$ to improve contact conductance. The lithography recipes are as follows:

Laser writer lithography: For improved lift-off, a bi-layer stack of LOR 5A (Microchem) and photolithography resist AZ5214 was prepared. The following steps were followed:

- Spincoating of LOR 5A (Microchem) at 4000 rpm for 30 s
- Pre-exposure baking at 170°C for 150 s.
- Spincoating of AZ5214 at 4000 rpm for 30 s
- Pre-exposure baking at 110°C for 90 s.

The devices are then exposed with lens number 5 for maximum resolution and developed in AZ 726 MIF for 90s. The development of the resist is stopped in DI water, and devices are dried with nitrogen gas. To achieve optimized results, a number of dose tests have been done for the substrates used. After metal evaporation the residual metal was lifted-off in NMP (1-methyl-2-pyrrolidone) for 2 h, followed by thorough acetone and isopropanol rinse.

Electron beam lithography: The fabrication of electrodes and also the "window"-masks of devices described in chapter 5 follow the same recipe.

- Spincoating of PMMA 950k (PMMA : Trichlorobenzene 3:1) at 8000 rpm for 60 s
- Pre-exposure baking at 175°C for 5 minutes.

Several dose tests have been done to find optimized exposure parameters depending on the lithography system. The devices were then developed in MIBK:isopropanol (1:3) for 45 s and the development was stopped in isopropanol. After metal evaporation the residual metal was lifted-off in acetone (at 55°C) for 3 h and rinsed with isopropanol.

For "window" devices, as shown in chapter 5, two lithographic steps are necessary. The first step defines the electrode areas to contact the flakes and several alignment markers in the close surrounding. These markers are then used as a reference to precisely align the second lithography with the previous exposure. While the first lithography step can be performed with laser writer lithography or electron beam lithography, the second step is always done by electron beam lithography, as it allows for higher resolution and the used PMMA resist is compatible with further processing with colloidal quantum dots.

A similar two-step lithography is applied for pure Au contacts without a Ti adhesion layer. Au poorly adheres to SiO_2 substrates, and large Au contacts are easily lifted off. Therefore, Ti/Au electrodes were fabricated in a first step to form the well attached contact basis, and a second lithography step was used to expose

only small contact areas, which overlap with Ti/Au electrodes and define the channel dimensions of the flake. In this area pure Au is deposited to form the final contact.

Quantum dot synthesis

Synthesis of PbS quantum dots with an excitonic peak at 980 nm: The reaction was carried out using standard Schlenk techniques. All reagents were purchased from Sigma Aldrich. PbO (2 mmol), oleic acid (OA) (4 mmol) and 1-octadecene (ODE) (8 mmol) were pumped overnight at 95°C. After this time, ODE (15 ml) was added and the temperature of the reaction was raised to 120°C. When this point was reached, hexamethyldisilathiane (HMS) (1 mmol) mixed with ODE (10 ml) were quickly injected. The heating was stopped (without removing the heating mantel) and the reaction was allowed to cool down slowly. The nanocrystals were isolated by addition of acetone and centrifugation, purified by dispersion/precipitation with toluene/acetone, and finally dispersed in anhydrous toluene.

Synthesis of PbS Quantum Dots with Excitonic Peak at 1380 nm: PbO (2 mmol) and OA (Oleic acid) (12 mmol) were pumped overnight at 85°C. After this time, ODE (1-Octadecene) (15 ml) was added and the reaction of the temperature was raised to 135°C. When this temperature was reached, HMS (Hexamethyldisilathiane) (1 mmol) mixed with ODE (10 ml) were quickly injected while the heating was stopped (without removing the heating mantel), and the reaction was allowed to cool down slowly ($\sim$65 min). The nanocrystals were isolated after the addition of acetone and ethanol (5:1) and centrifugation, purified by two successive dispersions in toluene and precipitations with acetone/EtOH (4:1), and finally dispersed in anhydrous toluene.

After synthesis, oleylamine was added to the quantum dot solution, and the solution was stored for three days in the glovebox. Before the devices were fabricated, the quantum dots were cleaned by precipitation/dispersion in methanol/toluene two times.

Fabrication of hybrid TMDC-QD phototransistors: After the fabrication procedure of TMDC-FETs, a thin film of quantum dots was spincoated on top. Many different QD types (size and compound), organic ligands, and solvents have been used, which all followed a similar layer-by-layer deposition technique. For instance, PbS QDs were spincoated at 2000 rpm and crosslinked with EDT ligands as follows:

- Rinsing of substrate with several drops of acetonitril and toluene
- Deposition of one drop of PbS ($\sim$ 20-30 mg/ml in toluene) through a filter to avoid agglomerated QDs
- Deposition of 1-2 drops of EDT ($\sim$ 2% in acetonitrile) to crosslink the QDs
- Rinsing with several drops of acetonitrile and toluene

This procedure was repeated until the desired thickness was reached. For the stated concentrations, a film thickness of 15-25 nm per layer is achieved. For "window" devices, the solvents toluene and acetonitrile were replaced by octane and isopropanol, because they do not dissolve the PMMA film used for the window mask.

ALD recipes

Hafnia deposition: HfO_2 was deposited by atomic layer deposition (Savannah 200, Cambridge Nanotech).The carrier and purge gas was nitrogen (N_2) in which the sample was annealed at 200°C for around 1 h prior to deposition to remove surface bound adsorbates. After that, the temperature was kept at 200°C during deposition. Tetrakis(dimethylamino)-hafnium and H_2O precursors were used, alternating open valve times of 0.15 and 0.015 s, respectively, separated by a 25 s pump time. The resulting growth rate was determined with a profilometer (Alpha-Step IQ) to be $\sim$0.1 nm/cycle.

Alumina deposition: Water and trimethylaluminium were used as precursors with open valve times of 0.03 s, followed by a 65 s pump time (0.1 nm/cycle). The chamber was kept at 80°C during the deposition process. The substrates were heated at 80°C for 12h prior to the deposition to remove moisture traces .

Titania deposition: The carrier and purge gas was nitrogen (N_2) in which the sample was annealed at 200°C for around 1 h prior to deposition to remove surface bound adsorbates. After that, the temperature was kept at 200°C during deposition. Titanium isopropoxide and H_2O precursors were used, alternating open valve times of 0.1 s and 0.015 s, respectively, separated by a 10 s pump time. The resulting growth rate was 0.04nm/cycle.

Device characterization

Atomic-Force-Microscopy: Atomic force microscopy (AFM) studies were carried out using a Vecco Dimension 3100 system in tapping mode.

Raman: Raman spectroscopy studies were performed with a Renishaw Invia Raman Microscope at a wavelength of 532 nm.

Optoelectronic characterization All measurements were performed in ambient conditions. Current-voltage characteristics were acquired using an Agilent B1500A semiconducting device analyzer. The optoelectronic response was measured under global illumination with a spot size of 2 mm. The spectral photoresponse was recorded by illuminating the device with fiber-coupled and spectrally filtered light from a supercontinuum light source (SuperKExtreme EXW-4, NKT Photonics). Responsivity and temporal response were measured under short-pulsed illumination at a wavelength of 635 nm from a 4-channel laser controlled with an Agilent A33220A waveform generator.

The frequency-dependent noise current was obtained by analysing the dark current in the conducting channel. Several dark current traces were acquired with the Agilent system under same V_G and V_{DS} conditions as the optical measurements. Since responsivity was usually measured at a light modulation frequency of 1 Hz, the noise current was extracted at 1 Hz to calculate the corresponding detectivity D*(1Hz).

Bibliography

[1] P. Cambou, J.-L. Jaffard, “CMOS Image Sensors - Status of the CMOS Image Sensor Industry report,” Yole Developpment, 2015. (see pp. 1 and 3)

[2] G. Girardin, B. Roussel, S. Clerc, “Wearable Electronics - Sensors for Wearable Electronics & Mobile Healthcare.” Yole Developpment, 2015. (see p. 1)

[3] T. Hirayama, “The evolution of CMOS image sensors,” in *2013 IEEE Asian Solid-State Circuits Conference (A-SSCC)*, pp. 5–8, IEEE, nov 2013. (see p. 2)

[4] A. Lustica, “CCD and CMOS image sensors in new HD cameras,” *ELMAR, 2011 Proceedings*, 2011. (see p. 2)

[5] M. El-Desouki, M. J. Deen, Q. Fang, L. Liu, F. Tse, and D. Armstrong, “CMOS Image Sensors for High Speed Applications.,” *Sensors (Basel, Switzerland)*, vol. 9, pp. 430–44, jan 2009. (see p. 2)

[6] M.-J. Lee, H. Rucker, and W.-Y. Choi, “Effects of Guard-Ring Structures on the Performance of Silicon Avalanche Photodetectors Fabricated With Standard CMOS Technology,” *IEEE Electron Device Letters*, vol. 33, pp. 80–82, jan 2012. (see p. 3)

[7] E. Kamrani, F. Lesage, and M. Sawan, “Premature edge breakdown prevention techniques in CMOS APD fabrication,” in *10th IEEE International NEWCAS Conference*, pp. 345–348, IEEE, jun 2012. (see p. 3)

[8] A. K. Dutta, “Imaging beyond human vision,” in *8th International Conference on Electrical and Computer Engineering*, pp. 224–229, IEEE, dec 2014. (see pp. 3 and 4)

[9] M. Buscema, J. O. Island, D. J. Groenendijk, S. I. Blanter, G. A. Steele, H. S. J. van der Zant, and A. Castellanos-Gomez, “Photocurrent generation with two-

dimensional van der Waals semiconductors.," *Chemical Society reviews*, apr 2015. (see pp. 3, 5, and 12)

[10] M. Cohen, M. Lange, M. Ettenberg, P. Dixon, and G. Olsen, "A thin film indium gallium arsenide focal plane array for visible and near infrared hyperspectral imaging," in *1999 IEEE LEOS Annual Meeting Conference Proceedings. LEOS'99. 12th Annual Meeting. IEEE Lasers and Electro-Optics Society 1999 Annual Meeting* , vol. 2, pp. 744–745, IEEE, 1999. (see p. 4)

[11] J. Jiang, S. Tsao, T. OSullivan, M. Razeghi, and G. J. Brown, "Fabrication of indium bumps for hybrid infrared focal plane array applications," *Infrared Physics & Technology*, vol. 45, pp. 143–151, mar 2004. (see p. 4)

[12] G. Konstantatos and E. H. Sargent, "Solution-Processed Quantum Dot Photodetectors," *Proceedings of the IEEE*, vol. 97, pp. 1666–1683, oct 2009. (see pp. 4 and 18)

[13] A. Nathan, A. Ahnood, M. T. Cole, Y. Suzuki, P. Hiralal, F. Bonaccorso, T. Hasan, L. Garcia-Gancedo, A. Dyadyusha, S. Haque, P. Andrew, S. Hofmann, J. Moultrie, A. J. Flewitt, A. C. Ferrari, M. J. Kelly, J. Robertson, G. A. J. Amaratunga, and W. I. Milne, "Flexible Electronics: The Next Ubiquitous Platform," *Proceedings of the IEEE*, vol. 100, pp. 1486–1517, may 2012. (see p. 4)

[14] K. S. Novoselov, A. K. Geim, S. V. Morozov, D. Jiang, Y. Zhang, S. V. Dubonos, I. V. Grigorieva, and A. A. Firsov, "Electric field effect in atomically thin carbon films.," *Science*, vol. 306, pp. 666–9, oct 2004. (see pp. 4 and 23)

[15] T. Mueller, F. Xia, and P. Avouris, "Graphene photodetectors for high-speed optical communications," *Nature Photonics*, vol. 4, pp. 297–301, mar 2010. (see p. 5)

[16] F. Xia, T. Mueller, Y.-M. Lin, A. Valdes-Garcia, and P. Avouris, "Ultrafast graphene photodetector.," *Nature nanotechnology*, vol. 4, pp. 839–43, dec 2009. (see p. 5)

[17] T. Echtermeyer, L. Britnell, P. Jasnos, A. Lombardo, R. Gorbachev, A. Grigorenko, A. Geim, A. Ferrari, and K. Novoselov, "Strong plasmonic enhancement of photovoltage in graphene," *Nature Communications*, vol. 2, p. 458, aug 2011. (see p. 5)

[18] Y. Liu, R. Cheng, L. Liao, H. Zhou, J. Bai, G. Liu, L. Liu, Y. Huang, and X. Duan, "Plasmon resonance enhanced multicolour photodetection by graphene.," *Nature communications*, vol. 2, p. 579, jan 2011. (see p. 5)

[19] X. Gan, R.-J. Shiue, Y. Gao, I. Meric, T. F. Heinz, K. Shepard, J. Hone, S. Assefa, and D. Englund, "Chip-integrated ultrafast graphene photodetector with high responsivity," *Nature Photonics*, vol. 7, pp. 883–887, sep 2013. (see p. 5)

[20] A. Pospischil, M. Humer, M. M. Furchi, D. Bachmann, R. Guider, T. Fromherz, and T. Mueller, "CMOS-compatible graphene photodetector covering all optical communication bands," *Nature Photonics*, vol. 7, pp. 892–896, sep 2013. (see p. 5)

[21] G. Konstantatos, M. Badioli, L. Gaudreau, J. Osmond, M. Bernechea, F. P. Garcia de Arquer, F. Gatti, and F. H. L. Koppens, "Hybrid graphene-quantum dot phototransistors with ultrahigh gain.," *Nature nanotechnology*, vol. 7, pp. 363–8, jun 2012. (see pp. 5 and 58)

[22] Y. Lee, J. Kwon, E. Hwang, C.-H. Ra, W. J. Yoo, J.-H. Ahn, J. H. Park, and J. H. Cho, "High-performance perovskite-graphene hybrid photodetector.," *Advanced materials*, vol. 27, pp. 41–6, jan 2015. (see pp. 5 and 58)

[23] Z. Sun, Z. Liu, J. Li, G.-A. Tai, S.-P. Lau, and F. Yan, "Infrared photodetectors based on CVD-grown graphene and PbS quantum dots with ultrahigh responsivity.," *Advanced materials*, vol. 24, pp. 5878–83, nov 2012. (see pp. 5 and 58)

[24] K.-J. Baeg, M. Binda, D. Natali, M. Caironi, and Y.-Y. Noh, "Organic light detectors: photodiodes and phototransistors.," *Advanced materials* , vol. 25, pp. 4267–95, aug 2013. (see p. 5)

[25] A. K. Geim and I. V. Grigorieva, "Van der Waals heterostructures.," *Nature*, vol. 499, pp. 419–25, jul 2013. (see p. 5)

[26] D. Akinwande, N. Petrone, and J. Hone, "Two-dimensional flexible nanoelectronics.," *Nature communications*, vol. 5, p. 5678, jan 2014. (see pp. 5 and 6)

[27] L. Britnell, R. M. Ribeiro, A. Eckmann, R. Jalil, B. D. Belle, A. Mishchenko, Y.-J. Kim, R. V. Gorbachev, T. Georgiou, S. V. Morozov, A. N. Grigorenko,

A. K. Geim, C. Casiraghi, A. H. C. Neto, and K. S. Novoselov, "Strong Light-Matter Interactions in Heterostructures of Atomically Thin Films," *Science*, vol. 340, pp. 1311–1314, may 2013. (see p. 5)

[28] A. Pospischil, M. M. Furchi, and T. Mueller, "Solar-energy conversion and light emission in an atomic monolayer p-n diode.," *Nature nanotechnology*, vol. 9, pp. 257–61, apr 2014. (see p. 5)

[29] B. W. H. Baugher, H. O. H. Churchill, Y. Yang, and P. Jarillo-Herrero, "Optoelectronic devices based on electrically tunable p-n diodes in a monolayer dichalcogenide.," *Nature nanotechnology*, vol. 9, pp. 262–7, apr 2014. (see p. 5)

[30] S. Bertolazzi, D. Krasnozhon, and A. Kis, "Nonvolatile memory cells based on MoS2/graphene heterostructures.," *ACS nano*, vol. 7, pp. 3246–52, apr 2013. (see p. 5)

[31] L. Britnell, R. V. Gorbachev, R. Jalil, B. D. Belle, F. Schedin, A. Mishchenko, T. Georgiou, M. I. Katsnelson, L. Eaves, S. V. Morozov, N. M. R. Peres, J. Leist, A. K. Geim, K. S. Novoselov, and L. A. Ponomarenko, "Field-effect tunneling transistor based on vertical graphene heterostructures.," *Science*, vol. 335, pp. 947–50, feb 2012. (see p. 5)

[32] S. Das, R. Gulotty, A. V. Sumant, and A. Roelofs, "All two-dimensional, flexible, transparent, and thinnest thin film transistor.," *Nano letters*, vol. 14, pp. 2861–6, may 2014. (see p. 5)

[33] H.-Y. Chang, S. Yang, J. Lee, L. Tao, W.-S. Hwang, D. Jena, N. Lu, and D. Akinwande, "High-performance, highly bendable MoS2 transistors with high-k dielectrics for flexible low-power systems.," *ACS nano*, vol. 7, pp. 5446–52, jun 2013. (see p. 5)

[34] G.-H. Lee, Y.-J. Yu, X. Cui, N. Petrone, C.-H. Lee, M. S. Choi, D.-Y. Lee, C. Lee, W. J. Yoo, K. Watanabe, T. Taniguchi, C. Nuckolls, P. Kim, and J. Hone, "Flexible and transparent MoS2 field-effect transistors on hexagonal boron nitride-graphene heterostructures.," *ACS nano*, vol. 7, pp. 7931–6, sep 2013. (see p. 5)

[35] M. R. Laskar, L. Ma, S. Kannappan, P. Sung Park, S. Krishnamoorthy, D. N. Nath, W. Lu, Y. Wu, and S. Rajan, "Large area single crystal (0001) oriented MoS2," *Applied Physics Letters*, vol. 102, p. 252108, jun 2013. (see p. 6)

[36] Y. Shi, H. Li, and L.-J. Li, "Recent advances in controlled synthesis of two-dimensional transition metal dichalcogenides via vapour deposition techniques.," *Chemical Society reviews*, vol. 44, pp. 2744–56, may 2015. (see p. 6)

[37] Q. H. Wang, K. Kalantar-Zadeh, A. Kis, J. N. Coleman, and M. S. Strano, "Electronics and optoelectronics of two-dimensional transition metal dichalcogenides.," *Nature nanotechnology*, vol. 7, pp. 699–712, nov 2012. (see pp. 6 and 24)

[38] N. Izhaky, M. T. Morse, S. Koehl, O. Cohen, D. Rubin, A. Barkai, G. Sarid, R. Cohen, and M. J. Paniccia, "Development of CMOS-Compatible Integrated Silicon Photonics Devices," *IEEE Journal of Selected Topics in Quantum Electronics*, vol. 12, pp. 1688–1698, nov 2006. (see p. 6)

[39] F. H. L. Koppens, T. Mueller, P. Avouris, A. C. Ferrari, M. S. Vitiello, and M. Polini, "Photodetectors based on graphene, other two-dimensional materials and hybrid systems," *Nature Nanotechnology*, vol. 9, pp. 780–793, oct 2014. (see p. 6)

[40] Z. Yin, H. Li, H. Li, L. Jiang, Y. Shi, Y. Sun, G. Lu, Q. Zhang, X. Chen, and H. Zhang, "Single-layer MoS2 phototransistors.," *ACS nano*, vol. 6, pp. 74–80, jan 2012. (see pp. 7, 33, 34, and 66)

[41] W. Choi, M. Y. Cho, A. Konar, J. H. Lee, G.-B. Cha, S. C. Hong, S. Kim, J. Kim, D. Jena, J. Joo, and S. Kim, "High-detectivity multilayer MoS(2) phototransistors with spectral response from ultraviolet to infrared.," *Advanced materials* , vol. 24, pp. 5832–6, nov 2012. (see pp. 7, 33, 34, and 66)

[42] O. Lopez-Sanchez, D. Lembke, M. Kayci, A. Radenovic, and A. Kis, "Ultrasensitive photodetectors based on monolayer MoS2.," *Nature nanotechnology*, vol. 8, pp. 497–501, jul 2013. (see pp. 7, 33, 34, 40, and 66)

[43] J. Kwon, Y. K. Hong, G. Han, I. Omkaram, W. Choi, S. Kim, and Y. Yoon, "Giant Photoamplification in Indirect-Bandgap Multilayer MoS2 Phototransistors with Local Bottom-Gate Structures.," *Advanced materials* , vol. 27, pp. 2224–30, apr 2015. (see pp. 7, 33, and 34)

[44] W. Zhang, J.-K. Huang, C.-H. Chen, Y.-H. Chang, Y.-J. Cheng, and L.-J. Li, "High-gain phototransistors based on a CVD MoS monolayer.," *Advanced materials*, vol. 25, pp. 3456–61, jul 2013. (see pp. 7, 33, 34, 40, and 42)

[45] Y.-H. Chang, W. Zhang, Y. Zhu, Y. Han, J. Pu, J.-K. Chang, W.-T. Hsu, J.-K. Huang, C.-L. Hsu, M.-H. Chiu, T. Takenobu, H. Li, C.-I. Wu, W.-H. Chang, A. T. S. Wee, and L.-J. Li, "Monolayer MoSe2 grown by chemical vapor deposition for fast photodetection.," *ACS nano*, vol. 8, pp. 8582–90, aug 2014. (see pp. 7, 33, and 34)

[46] H. S. Lee, S.-W. Min, Y.-G. Chang, M. K. Park, T. Nam, H. Kim, J. H. Kim, S. Ryu, and S. Im, "MoS nanosheet phototransistors with thickness-modulated optical energy gap.," *Nano letters*, vol. 12, pp. 3695–700, jul 2012. (see pp. 7, 33, and 34)

[47] D.-S. Tsai, K.-K. Liu, D.-H. Lien, M.-L. Tsai, C.-F. Kang, C.-A. Lin, L.-J. Li, and J.-H. He, "Few-Layer MoS2 with high broadband Photogain and fast optical switching for use in harsh environments.," *ACS nano*, vol. 7, pp. 3905–11, may 2013. (see pp. 7, 33, and 34)

[48] W. Zhang, M.-H. Chiu, C.-H. Chen, W. Chen, L.-J. Li, and A. T. S. Wee, "Role of metal contacts in high-performance phototransistors based on WSe2 monolayers.," *ACS nano*, vol. 8, pp. 8653–61, aug 2014. (see pp. 7, 33, and 34)

[49] N. Huo, S. Yang, Z. Wei, S.-S. Li, J.-B. Xia, and J. Li, "Photoresponsive and gas sensing field-effect transistors based on multilayer WS nanoflakes.," *Scientific reports*, vol. 4, p. 5209, jan 2014. (see pp. 7, 33, and 34)

[50] N. Perea-López, A. L. Elías, A. Berkdemir, A. Castro-Beltran, H. R. Gutiérrez, S. Feng, R. Lv, T. Hayashi, F. López-Urías, S. Ghosh, B. Muchharla, S. Talapatra, H. Terrones, and M. Terrones, "Photosensor Device Based on Few-Layered WS 2 Films," *Advanced Functional Materials*, vol. 23, pp. 5511–5517, nov 2013. (see pp. 7, 33, and 34)

[51] N. Perea-López, Z. Lin, N. R. Pradhan, A. Iñiguez-Rábago, A. Laura Elías, A. McCreary, J. Lou, P. M. Ajayan, H. Terrones, L. Balicas, and M. Terrones, "CVD-grown monolayered MoS2 as an effective photosensor operating at low-voltage," *2D Materials*, vol. 1, p. 011004, apr 2014. (see pp. 7, 33, and 34)

[52] A. Abderrahmane, P. J. Ko, T. V. Thu, S. Ishizawa, T. Takamura, and A. Sandhu, "High photosensitivity few-layered MoSe2 back-gated field-effect phototransistors.," *Nanotechnology*, vol. 25, p. 365202, sep 2014. (see pp. 7, 33, and 34)

[53] Y. Du, H. Liu, A. T. Neal, M. Si, and P. D. Ye, "Molecular Doping of Multilayer MoS2 Field-Effect Transistors: Reduction in Sheet and Contact Resistances,"

IEEE Electron Device Letters, vol. 34, pp. 1328–1330, oct 2013. (see pp. 8 and 74)

[54] D. Kiriya, M. Tosun, P. Zhao, J. S. Kang, and A. Javey, “Air-stable surface charge transfer doping of MoS by benzyl viologen.,” *Journal of the American Chemical Society*, vol. 136, pp. 7853–6, jun 2014. (see pp. 8 and 74)

[55] H. Fang, M. Tosun, G. Seol, T. C. Chang, K. Takei, J. Guo, and A. Javey, “Degenerate n-doping of few-layer transition metal dichalcogenides by potassium.,” *Nano letters*, vol. 13, pp. 1991–5, may 2013. (see pp. 8, 28, and 74)

[56] Y. Li, C.-Y. Xu, P. Hu, and L. Zhen, “Carrier Control of MoS2 Nanoflakes by Functional Self-Assembled Monolayers.,” *ACS nano*, vol. 7, pp. 7795–804, sep 2013. (see pp. 8 and 74)

[57] D. M. Sim, M. Kim, S. Yim, M.-J. Choi, J. Choi, S. Yoo, and Y. S. Jung, “Controlled Doping of Vacancy-Containing Few-Layer MoS2 via Highly Stable Thiol-Based Molecular Chemisorption.,” *ACS nano*, vol. 9, pp. 12115–23, dec 2015. (see pp. 8, 74, and 76)

[58] M. Buscema, M. Barkelid, V. Zwiller, H. S. J. van der Zant, G. A. Steele, and A. Castellanos-Gomez, “Large and tunable photothermoelectric effect in single-layer MoS2.,” *Nano letters*, vol. 13, pp. 358–63, feb 2013. (see p. 12)

[59] C.-C. Wu, D. Jariwala, V. K. Sangwan, T. J. Marks, M. C. Hersam, and L. J. Lauhon, “Elucidating the Photoresponse of Ultrathin MoS 2 Field-Effect Transistors by Scanning Photocurrent Microscopy,” *The Journal of Physical Chemistry Letters*, vol. 4, pp. 2508–2513, aug 2013. (see pp. 12 and 40)

[60] M. M. Furchi, D. K. Polyushkin, A. Pospischil, and T. Mueller, “Mechanisms of photoconductivity in atomically thin MoS2.,” *Nano letters*, vol. 14, pp. 6165–70, nov 2014. (see pp. 12, 34, and 40)

[61] G. B. E.L. Dereniak, *Infrared Detectors and Systems.* 1996. (see p. 18)

[62] A. Splendiani, L. Sun, Y. Zhang, T. Li, J. Kim, C.-Y. Chim, G. Galli, and F. Wang, “Emerging photoluminescence in monolayer MoS2.,” *Nano letters*, vol. 10, pp. 1271–5, apr 2010. (see pp. 22 and 23)

[63] K. F. Mak, C. Lee, J. Hone, J. Shan, and T. F. Heinz, “Atomically Thin MoS_{2}: A New Direct-Gap Semiconductor,” *Physical Review Letters*, vol. 105, p. 136805, sep 2010. (see pp. 22, 23, 27, and 51)

[64] A. Kuc, N. Zibouche, and T. Heine, "Influence of quantum confinement on the electronic structure of the transition metal sulfide T S 2," *Physical Review B*, vol. 83, p. 245213, jun 2011. (see p. 22)

[65] S.-L. Li, K. Komatsu, S. Nakaharai, Y.-F. Lin, M. Yamamoto, X. Duan, and K. Tsukagoshi, "Thickness scaling effect on interfacial barrier and electrical contact to two-dimensional MoS2 layers.," *ACS nano*, vol. 8, pp. 12836–42, dec 2014. (see p. 23)

[66] C. Lee, H. Yan, L. E. Brus, T. F. Heinz, J. Hone, and S. Ryu, "Anomalous lattice vibrations of single- and few-layer MoS2.," *ACS nano*, vol. 4, pp. 2695–700, may 2010. (see pp. 24 and 26)

[67] A. Molina-Sánchez and L. Wirtz, "Phonons in single-layer and few-layer MoS 2 and WS 2," *Physical Review B*, vol. 84, p. 155413, oct 2011. (see p. 26)

[68] A. Taube, J. Judek, C. Jastrzbski, A. Duzynska, K. Świtkowski, and M. Zdrojek, "Temperature-dependent nonlinear phonon shifts in a supported MoS2 monolayer.," *ACS applied materials & interfaces*, vol. 6, pp. 8959–63, jun 2014. (see p. 26)

[69] M. Buscema, G. A. Steele, H. S. J. van der Zant, and A. Castellanos-Gomez, "The effect of the substrate on the Raman and photoluminescence emission of single-layer MoS2," *Nano Research*, vol. 7, pp. 561–571, jan 2015. (see p. 26)

[70] J. Appenzeller, J. Knoch, V. Derycke, R. Martel, S. Wind, and P. Avouris, "Field-modulated carrier transport in carbon nanotube transistors.," *Physical review letters*, vol. 89, p. 126801, sep 2002. (see p. 27)

[71] J. Appenzeller, M. Radosavljević, J. Knoch, and P. Avouris, "Tunneling versus thermionic emission in one-dimensional semiconductors.," *Physical review letters*, vol. 92, p. 048301, jan 2004. (see p. 27)

[72] A. V. Penumatcha, R. B. Salazar, and J. Appenzeller, "Analysing black phosphorus transistors using an analytic Schottky barrier MOSFET model.," *Nature communications*, vol. 6, p. 8948, jan 2015. (see p. 27)

[73] D. Lembke, S. Bertolazzi, and A. Kis, "Single-layer MoS2 electronics.," *Accounts of chemical research*, vol. 48, pp. 100–10, jan 2015. (see pp. 28 and 89)

[74] Y. Yoon, K. Ganapathi, and S. Salahuddin, "How good can monolayer MoS transistors be?," *Nano letters*, vol. 11, pp. 3768–73, sep 2011. (see p. 28)

[75] C.-P. Lu, G. Li, J. Mao, L.-M. Wang, and E. Y. Andrei, "Bandgap, mid-gap states, and gating effects in MoS2.," *Nano letters*, vol. 14, pp. 4628–33, aug 2014. (see p. 28)

[76] J. Suh, T.-E. Park, D.-Y. Lin, D. Fu, J. Park, H. J. Jung, Y. Chen, C. Ko, C. Jang, Y. Sun, R. Sinclair, J. Chang, S. Tongay, and J. Wu, "Doping against the native propensity of MoS2: degenerate hole doping by cation substitution.," *Nano letters*, vol. 14, pp. 6976–82, dec 2014. (see pp. 28 and 74)

[77] I. Popov, G. Seifert, and D. Tománek, "Designing electrical contacts to MoS2 monolayers: a computational study.," *Physical review letters*, vol. 108, p. 156802, apr 2012. (see p. 28)

[78] S. Das, H.-Y. Chen, A. V. Penumatcha, and J. Appenzeller, "High performance multilayer MoS2 transistors with scandium contacts.," *Nano letters*, vol. 13, pp. 100–5, jan 2013. (see pp. 28, 30, 35, and 77)

[79] G. R. Bhimanapati, Z. Lin, V. Meunier, Y. Jung, J. J. Cha, S. Das, D. Xiao, Y. Son, M. S. Strano, V. R. Cooper, L. Liang, S. G. Louie, E. Ringe, W. Zhou, B. G. Sumpter, H. Terrones, F. Xia, Y. Wang, J. Zhu, D. Akinwande, N. Alem, J. A. Schuller, R. E. Schaak, M. Terrones, and J. A. Robinson, "Recent Advances in Two-Dimensional Materials Beyond Graphene.," *ACS nano*, vol. 9, pp. 11509–11539, nov 2015. (see p. 28)

[80] R. Kappera, D. Voiry, S. E. Yalcin, B. Branch, G. Gupta, A. D. Mohite, and M. Chhowalla, "Phase-engineered low-resistance contacts for ultrathin MoS2 transistors.," *Nature materials*, vol. 13, pp. 1128–34, dec 2014. (see p. 28)

[81] L. Yang, K. Majumdar, H. Liu, Y. Du, H. Wu, M. Hatzistergos, P. Y. Hung, R. Tieckelmann, W. Tsai, C. Hobbs, and P. D. Ye, "Chloride molecular doping technique on 2D materials: WS2 and MoS2.," *Nano letters*, vol. 14, pp. 6275–80, nov 2014. (see pp. 28 and 74)

[82] K. Majumdar, P. D. Kirsch, and P. D. Ye, "MoS2 Field-Effect Transistors With Graphene/Metal Heterocontacts," *IEEE Electron Device Letters*, vol. 35, pp. 599–601, may 2014. (see p. 28)

[83] X. Cui, G.-H. Lee, Y. D. Kim, G. Arefe, P. Y. Huang, C.-H. Lee, D. A. Chenet, X. Zhang, L. Wang, F. Ye, F. Pizzocchero, B. S. Jessen, K. Watanabe, T. Taniguchi, D. A. Muller, T. Low, P. Kim, and J. Hone, "Multi-terminal transport measurements of MoS2 using a van der Waals heterostructure device

platform.," *Nature nanotechnology*, vol. 10, pp. 534–40, jun 2015. (see pp. 28 and 30)

[84] W. Liu, J. Kang, W. Cao, D. Sarkar, Y. Khatami, D. Jena, and K. Banerjee, "High-performance few-layer-MoS¡inf¿2¡/inf¿ field-effect-transistor with record low contact-resistance," in *2013 IEEE International Electron Devices Meeting*, pp. 19.4.1–19.4.4, IEEE, dec 2013. (see pp. 28 and 31)

[85] A. Castellanos-Gomez, E. Cappelluti, R. Roldán, N. Agraït, F. Guinea, and G. Rubio-Bollinger, "Electric-field screening in atomically thin layers of MoS: the role of interlayer coupling.," *Advanced materials* , vol. 25, pp. 899–903, feb 2013. (see p. 28)

[86] H. Schmidt, F. Giustiniano, and G. Eda, "Electronic transport properties of transition metal dichalcogenide field-effect devices: surface and interface effects," *Chem. Soc. Rev.*, vol. 44, pp. 7715–7736, oct 2015. (see pp. 28 and 30)

[87] S.-L. Li, K. Wakabayashi, Y. Xu, S. Nakaharai, K. Komatsu, W.-W. Li, Y.-F. Lin, A. Aparecido-Ferreira, and K. Tsukagoshi, "Thickness-dependent interfacial Coulomb scattering in atomically thin field-effect transistors.," *Nano letters*, vol. 13, pp. 3546–52, aug 2013. (see p. 30)

[88] K. Kaasbjerg, K. S. Thygesen, and K. W. Jacobsen, "Phonon-limited mobility in n -type single-layer MoS 2 from first principles," *Physical Review B*, vol. 85, p. 115317, mar 2012. (see p. 30)

[89] N. Ma and D. Jena, "Charge Scattering and Mobility in Atomically Thin Semiconductors," *Physical Review X*, vol. 4, p. 011043, mar 2014. (see p. 30)

[90] S. Tongay, J. Zhou, C. Ataca, J. Liu, J. S. Kang, T. S. Matthews, L. You, J. Li, J. C. Grossman, and J. Wu, "Broad-range modulation of light emission in two-dimensional semiconductors by molecular physisorption gating.," *Nano letters*, vol. 13, pp. 2831–6, jun 2013. (see pp. 34 and 74)

[91] Q. Yue, Z. Shao, S. Chang, and J. Li, "Adsorption of gas molecules on monolayer MoS2 and effect of applied electric field.," *Nanoscale research letters*, vol. 8, p. 425, jan 2013. (see p. 34)

[92] B. W. H. Baugher, H. O. H. Churchill, Y. Yang, and P. Jarillo-Herrero, "Intrinsic electronic transport properties of high-quality monolayer and bilayer MoS2.," *Nano letters*, vol. 13, pp. 4212–6, sep 2013. (see p. 35)

[93] D. Ovchinnikov, A. Allain, Y.-S. Huang, D. Dumcenco, and A. Kis, "Electrical transport properties of single-layer WS2.," *ACS nano*, vol. 8, pp. 8174–81, aug 2014. (see p. 35)

[94] D. Lembke, A. Allain, and A. Kis, "Thickness-dependent mobility in two-dimensional MoS2 transistors.," *Nanoscale*, vol. 7, pp. 6255–60, mar 2015. (see pp. 35 and 36)

[95] J. Na, M.-K. Joo, M. Shin, J. Huh, J.-S. Kim, M. Piao, J.-E. Jin, H.-K. Jang, H. J. Choi, J. H. Shim, and G.-T. Kim, "Low-frequency noise in multilayer MoS2 field-effect transistors: the effect of high-k passivation.," *Nanoscale*, vol. 6, pp. 433–41, jan 2014. (see pp. 35 and 36)

[96] B. Radisavljevic, A. Radenovic, J. Brivio, V. Giacometti, and A. Kis, "Single-layer MoS2 transistors.," *Nature nanotechnology*, vol. 6, pp. 147–50, mar 2011. (see pp. 35 and 38)

[97] D. J. Late, B. Liu, H. S. S. R. Matte, V. P. Dravid, and C. N. R. Rao, "Hysteresis in single-layer MoS2 field effect transistors.," *ACS nano*, vol. 6, pp. 5635–41, jun 2012. (see p. 35)

[98] L. Cheng, X. Qin, A. T. Lucero, A. Azcatl, J. Huang, R. M. Wallace, K. Cho, and J. Kim, "Atomic layer deposition of a high-k dielectric on MoS2 using trimethylaluminum and ozone.," *ACS applied materials & interfaces*, vol. 6, pp. 11834–8, aug 2014. (see p. 36)

[99] H. Liu and P. D. Ye, "MoS2 Dual-Gate MOSFET With Atomic-Layer-Deposited Al2O3 as Top-Gate Dielectric," *IEEE Electron Device Letters*, vol. 33, pp. 546–548, apr 2012. (see p. 36)

[100] B. Radisavljevic and A. Kis, "Mobility engineering and a metal-insulator transition in monolayer MoS.," *Nature materials*, vol. 12, pp. 815–20, sep 2013. (see p. 36)

[101] T. Cheiwchanchamnangij and W. R. L. Lambrecht, "Quasiparticle band structure calculation of monolayer, bilayer, and bulk MoS 2," *Physical Review B*, vol. 85, p. 205302, may 2012. (see pp. 38 and 50)

[102] S. Ghatak, A. N. Pal, and A. Ghosh, "Nature of electronic states in atomically thin MoS field-effect transistors.," *ACS nano*, vol. 5, pp. 7707–12, oct 2011. (see p. 40)

[103] S. Ghatak and A. Ghosh, "Observation of trap-assisted space charge limited conductivity in short channel MoS2 transistor," *Applied Physics Letters*, vol. 103, p. 122103, sep 2013. (see p. 40)

[104] G. Konstantatos, I. Howard, A. Fischer, S. Hoogland, J. Clifford, E. Klem, L. Levina, and E. H. Sargent, "Ultrasensitive solution-cast quantum dot photodetectors.," *Nature*, vol. 442, pp. 180–3, jul 2006. (see pp. 40, 53, 55, and 57)

[105] G. Konstantatos, J. Clifford, L. Levina, and E. H. Sargent, "Sensitive solution-processed visible-wavelength photodetectors," *Nature Photonics*, vol. 1, pp. 531–534, sep 2007. (see pp. 40, 53, and 57)

[106] V. Klee, E. Preciado, D. Barroso, A. E. Nguyen, C. Lee, K. J. Erickson, M. Triplett, B. Davis, I.-H. Lu, S. Bobek, J. McKinley, J. P. Martinez, J. Mann, A. A. Talin, L. Bartels, and F. Léonard, "Superlinear Composition-Dependent Photocurrent in CVD-Grown Monolayer MoS2(1-x)Se2x Alloy Devices.," *Nano letters*, vol. 15, pp. 2612–9, apr 2015. (see p. 41)

[107] A. Rose, "Recombination Processes in Insulators and Semiconductors," *Physical Review*, vol. 97, pp. 322–333, jan 1955. (see p. 41)

[108] E. Zhang, W. Wang, C. Zhang, Y. Jin, G. Zhu, Q. Sun, D. W. Zhang, P. Zhou, and F. Xiu, "Tunable charge-trap memory based on few-layer MoS2.," *ACS nano*, vol. 9, pp. 612–9, jan 2015. (see p. 42)

[109] J. Renteria, R. Samnakay, S. L. Rumyantsev, C. Jiang, P. Goli, M. S. Shur, and A. A. Balandin, "Low-frequency 1/f noise in MoS2 transistors: Relative contributions of the channel and contacts," *Applied Physics Letters*, vol. 104, p. 153104, apr 2014. (see pp. 44 and 83)

[110] H.-J. Kwon, H. Kang, J. Jang, S. Kim, and C. P. Grigoropoulos, "Analysis of flicker noise in two-dimensional multilayer MoS2 transistors," *Applied Physics Letters*, vol. 104, p. 083110, feb 2014. (see p. 44)

[111] S. Ghatak, S. Mukherjee, M. Jain, D. D. Sarma, and A. Ghosh, "Microscopic origin of low frequency noise in MoS2 field-effect transistors," *APL Materials*, vol. 2, p. 092515, sep 2014. (see p. 44)

[112] M. Bernardi, M. Palummo, and J. C. Grossman, "Extraordinary sunlight absorption and one nanometer thick photovoltaics using two-dimensional monolayer materials.," *Nano letters*, vol. 13, pp. 3664–70, aug 2013. (see p. 50)

[113] L. Britnell, R. M. Ribeiro, A. Eckmann, R. Jalil, B. D. Belle, A. Mishchenko, Y.-J. Kim, R. V. Gorbachev, T. Georgiou, S. V. Morozov, A. N. Grigorenko, A. K. Geim, C. Casiraghi, A. H. Castro Neto, and K. S. Novoselov, "Strong light-matter interactions in heterostructures of atomically thin films.," *Science* , vol. 340, pp. 1311–4, jun 2013. (see p. 50)

[114] G. Eda and S. A. Maier, "Two-dimensional crystals: managing light for optoelectronics.," *ACS nano*, vol. 7, pp. 5660–5, jul 2013. (see p. 50)

[115] M. Amani, D.-H. Lien, D. Kiriya, J. Xiao, A. Azcatl, J. Noh, S. R. Madhvapathy, R. Addou, S. KC, M. Dubey, K. Cho, R. M. Wallace, S.-C. Lee, J.-H. He, J. W. Ager, X. Zhang, E. Yablonovitch, and A. Javey, "Near-unity photoluminescence quantum yield in MoS2," *Science*, vol. 350, pp. 1065–1068, nov 2015. (see pp. 50 and 51)

[116] A. Ramasubramaniam, "Large excitonic effects in monolayers of molybdenum and tungsten dichalcogenides," *Physical Review B*, vol. 86, p. 115409, sep 2012. (see p. 50)

[117] H. Wang, C. Zhang, and F. Rana, "Ultrafast dynamics of defect-assisted electron-hole recombination in monolayer MoS2.," *Nano letters*, vol. 15, pp. 339–45, jan 2015. (see pp. 50 and 51)

[118] V. Sukhovatkin, S. Hinds, L. Brzozowski, and E. H. Sargent, "Colloidal quantum-dot photodetectors exploiting multiexciton generation.," *Science*, vol. 324, pp. 1542–4, jun 2009. (see p. 53)

[119] S. Keuleyan, E. Lhuillier, V. Brajuskovic, and P. Guyot-Sionnest, "Mid-infrared HgTe colloidal quantum dot photodetectors," *Nature Photonics*, vol. 5, pp. 489–493, jul 2011. (see pp. 53 and 72)

[120] J. Y. Kim, V. Adinolfi, B. R. Sutherland, O. Voznyy, S. J. Kwon, T. W. Kim, J. Kim, H. Ihee, K. Kemp, M. Adachi, M. Yuan, I. Kramer, D. Zhitomirsky, S. Hoogland, and E. H. Sargent, "Single-step fabrication of quantum funnels via centrifugal colloidal casting of nanoparticle films.," *Nature communications*, vol. 6, p. 7772, jan 2015. (see pp. 54 and 57)

[121] D. V. Talapin, J.-S. Lee, M. V. Kovalenko, and E. V. Shevchenko, "Prospects of colloidal nanocrystals for electronic and optoelectronic applications.," *Chemical reviews*, vol. 110, pp. 389–458, jan 2010. (see pp. 54 and 56)

[122] G. H. Carey, A. L. Abdelhady, Z. Ning, S. M. Thon, O. M. Bakr, and E. H. Sargent, "Colloidal Quantum Dot Solar Cells," *Chemical Reviews*, vol. 115, p. 150624090720003, jun 2015. (see pp. 54, 56, and 75)

[123] G. Konstantatos and E. H. Sargent, "Nanostructured materials for photon detection.," *Nature nanotechnology*, vol. 5, pp. 391–400, jun 2010. (see p. 54)

[124] R. Saran and R. J. Curry, "Lead sulphide nanocrystal photodetector technologies," *Nature Photonics*, vol. 10, pp. 81–92, jan 2016. (see pp. 54, 58, and 88)

[125] L. Qian, Y. Zheng, J. Xue, and P. H. Holloway, "Stable and efficient quantum-dot light-emitting diodes based on solution-processed multilayer structures," *Nature Photonics*, vol. 5, pp. 543–548, aug 2011. (see p. 54)

[126] L. Li, A. Pandey, D. J. Werder, B. P. Khanal, J. M. Pietryga, and V. I. Klimov, "Efficient synthesis of highly luminescent copper indium sulfide-based core/shell nanocrystals with surprisingly long-lived emission.," *Journal of the American Chemical Society*, vol. 133, pp. 1176–9, feb 2011. (see p. 54)

[127] J. Steckel, S. Coe-Sullivan, V. Bulović, and M. Bawendi, "1.3μm to 1.55μm Tunable Electroluminescence from PbSe Quantum Dots Embedded within an Organic Device," *Advanced Materials*, vol. 15, pp. 1862–1866, nov 2003. (see p. 54)

[128] E. Sargent, "Photodetectors: A sensitive pair.," *Nature nanotechnology*, vol. 7, pp. 349–50, jun 2012. (see pp. 56 and 58)

[129] J. P. Clifford, G. Konstantatos, K. W. Johnston, S. Hoogland, L. Levina, and E. H. Sargent, "Fast, sensitive and spectrally tuneable colloidal-quantum-dot photodetectors.," *Nature nanotechnology*, vol. 4, pp. 40–4, jan 2009. (see p. 57)

[130] K. K. Manga, Y. Zhou, Y. Yan, and K. P. Loh, "Multilayer Hybrid Films Consisting of Alternating Graphene and Titania Nanosheets with Ultrafast Electron Transfer and Photoconversion Properties," *Advanced Functional Materials*, vol. 19, pp. 3638–3643, nov 2009. (see p. 58)

[131] Y. Liu, F. Wang, X. Wang, X. Wang, E. Flahaut, X. Liu, Y. Li, X. Wang, Y. Xu, Y. Shi, and R. Zhang, "Planar carbon nanotube-graphene hybrid films for high-performance broadband photodetectors.," *Nature communications*, vol. 6, p. 8589, jan 2015. (see p. 58)

[132] K. Roy, M. Padmanabhan, S. Goswami, T. P. Sai, G. Ramalingam, S. Raghavan, and A. Ghosh, "Graphene-MoS2 hybrid structures for multifunctional photoresponsive memory devices.," *Nature nanotechnology*, vol. 8, pp. 826–30, nov 2013. (see p. 58)

[133] Y. Zhang, H. Li, L. Wang, H. Wang, X. Xie, S.-L. Zhang, R. Liu, and Z.-J. Qiu, "Photothermoelectric and photovoltaic effects both present in MoS2.," *Scientific reports*, vol. 5, p. 7938, jan 2015. (see p. 58)

[134] P. R. Brown, D. Kim, R. R. Lunt, N. Zhao, M. G. Bawendi, J. C. Grossman, and V. Bulović, "Energy level modification in lead sulfide quantum dot thin films through ligand exchange.," *ACS nano*, vol. 8, pp. 5863–72, jun 2014. (see p. 58)

[135] G. Konstantatos, L. Levina, A. Fischer, and E. H. Sargent, "Engineering the temporal response of photoconductive photodetectors via selective introduction of surface trap states.," *Nano letters*, vol. 8, pp. 1446–50, may 2008. (see p. 65)

[136] J. D. Lin, C. Han, F. Wang, R. Wang, D. Xiang, S. Qin, X.-A. Zhang, L. Wang, H. Zhang, A. T. S. Wee, and W. Chen, "Electron-doping-enhanced trion formation in monolayer molybdenum disulfide functionalized with cesium carbonate.," *ACS nano*, vol. 8, pp. 5323–9, may 2014. (see p. 74)

[137] K. Zhang, S. Feng, J. Wang, A. Azcatl, N. Lu, R. Addou, N. Wang, C. Zhou, J. Lerach, V. Bojan, M. J. Kim, L.-Q. Chen, R. M. Wallace, M. Terrones, J. Zhu, and J. A. Robinson, "Manganese Doping of Monolayer MoS2: The Substrate Is Critical.," *Nano letters*, vol. 15, pp. 6586–91, oct 2015. (see p. 74)

[138] S. Lei, X. Wang, B. Li, J. Kang, Y. He, A. George, L. Ge, Y. Gong, P. Dong, Z. Jin, G. Brunetto, W. Chen, Z.-T. Lin, R. Baines, D. S. Galvão, J. Lou, E. Barrera, K. Banerjee, R. Vajtai, and P. Ajayan, "Surface functionalization of two-dimensional metal chalcogenides by Lewis acidbase chemistry," *Nature Nanotechnology*, vol. advance on, feb 2016. (see p. 74)

[139] S. Mouri, Y. Miyauchi, and K. Matsuda, "Tunable photoluminescence of monolayer MoS via chemical doping.," *Nano letters*, vol. 13, pp. 5944–8, jan 2013. (see p. 74)

[140] M. Chen, H. Nam, S. Wi, L. Ji, X. Ren, L. Bian, S. Lu, and X. Liang, "Stable few-layer MoS2 rectifying diodes formed by plasma-assisted doping," *Applied Physics Letters*, vol. 103, p. 142110, oct 2013. (see p. 74)

[141] A. Nipane, D. Karmakar, N. Kaushik, S. Karande, and S. Lodha, “Few-Layer MoS2 p-Type Devices Enabled by Selective Doping Using Low Energy Phosphorus Implantation.,” *ACS nano*, jan 2016. (see p. 74)

[142] Z. Yu, Y. Pan, Y. Shen, Z. Wang, Z.-Y. Ong, T. Xu, R. Xin, L. Pan, B. Wang, L. Sun, J. Wang, G. Zhang, Y. W. Zhang, Y. Shi, and X. Wang, “Towards intrinsic charge transport in monolayer molybdenum disulfide by defect and interface engineering.,” *Nature communications*, vol. 5, p. 5290, jan 2014. (see p. 74)

[143] A. G. Pattantyus-Abraham, I. J. Kramer, A. R. Barkhouse, X. Wang, G. Konstantatos, R. Debnath, L. Levina, I. Raabe, M. K. Nazeeruddin, M. Grätzel, and E. H. Sargent, “Depleted-heterojunction colloidal quantum dot solar cells.,” *ACS nano*, vol. 4, pp. 3374–80, jun 2010. (see p. 75)

[144] D. A. R. Barkhouse, R. Debnath, I. J. Kramer, D. Zhitomirsky, A. G. Pattantyus-Abraham, L. Levina, L. Etgar, M. Grätzel, and E. H. Sargent, “Depleted bulk heterojunction colloidal quantum dot photovoltaics.,” *Advanced materials* , vol. 23, pp. 3134–8, jul 2011. (see p. 75)

[145] C. Gong, L. Colombo, R. M. Wallace, and K. Cho, “The unusual mechanism of partial Fermi level pinning at metal-MoS2 interfaces.,” *Nano letters*, vol. 14, pp. 1714–20, jan 2014. (see p. 77)

[146] W. Park, Y. Kim, U. Jung, C. Cho, and H.-B.-R. Lee, “Contact resistance reduction using Fermi level de-pinning layer for MoS2 FETs,” in *2014 IEEE International Electron Devices Meeting*, pp. 5.1.1–5.1.4, IEEE, dec 2014. (see p. 77)

[147] N. Kaushik, D. Karmakar, A. Nipane, S. Karande, and S. Lodha, “Interfacial n-Doping Using an Ultrathin TiO2 Layer for Contact Resistance Reduction in MoS2.,” *ACS applied materials & interfaces*, vol. 8, pp. 256–63, jan 2016. (see p. 77)

[148] H.-M. Li, D.-Y. Lee, M. S. Choi, D. Qu, X. Liu, C.-H. Ra, and W. J. Yoo, “Metal-semiconductor barrier modulation for high photoresponse in transition metal dichalcogenide field effect transistors.,” *Scientific reports*, vol. 4, p. 4041, jan 2014. (see p. 81)

[149] V. K. Sangwan, H. N. Arnold, D. Jariwala, T. J. Marks, L. J. Lauhon, and M. C. Hersam, “Low-frequency electronic noise in single-layer MoS2 transistors.,” *Nano letters*, vol. 13, pp. 4351–5, sep 2013. (see p. 83)

[150] C.-H. M. Chuang, P. R. Brown, V. Bulović, and M. G. Bawendi, "Improved performance and stability in quantum dot solar cells through band alignment engineering.," *Nature materials*, vol. 13, pp. 796–801, aug 2014. (see p. 85)

[151] A. Tada, Y. Geng, Q. Wei, K. Hashimoto, and K. Tajima, "Tailoring organic heterojunction interfaces in bilayer polymer photovoltaic devices.," *Nature materials*, vol. 10, pp. 450–5, jun 2011. (see p. 85)

[152] Z. He, C. Zhong, X. Huang, W.-Y. Wong, H. Wu, L. Chen, S. Su, and Y. Cao, "Simultaneous enhancement of open-circuit voltage, short-circuit current density, and fill factor in polymer solar cells.," *Advanced materials* , vol. 23, pp. 4636–43, oct 2011. (see p. 85)

[153] L. Barnea-Nehoshtan, P. K. Nayak, A. Shu, T. Bendikov, A. Kahn, and D. Cahen, "Enhancing the tunability of the open-circuit voltage of hybrid photovoltaics with mixed molecular monolayers.," *ACS applied materials & interfaces*, vol. 6, pp. 2317–24, feb 2014. (see p. 85)

[154] F. Schwierz, "Graphene transistors.," *Nature nanotechnology*, vol. 5, pp. 487–96, jul 2010. (see p. 89)

[155] G. Fiori, F. Bonaccorso, G. Iannaccone, T. Palacios, D. Neumaier, A. Seabaugh, S. K. Banerjee, and L. Colombo, "Electronics based on two-dimensional materials.," *Nature nanotechnology*, vol. 9, pp. 768–79, oct 2014. (see p. 89)

[156] A. Castellanos-Gomez, "Black Phosphorus: Narrow Gap, Wide Applications.," *The journal of physical chemistry letters*, vol. 6, pp. 4280–91, nov 2015. (see p. 89)

[157] L. Li, Y. Yu, G. J. Ye, Q. Ge, X. Ou, H. Wu, D. Feng, X. H. Chen, and Y. Zhang, "Black phosphorus field-effect transistors," *Nature Nanotechnology*, vol. 9, pp. 372–377, mar 2014. (see p. 89)

[158] T.-H. Kim, K.-S. Cho, E. K. Lee, S. J. Lee, J. Chae, J. W. Kim, D. H. Kim, J.-Y. Kwon, G. Amaratunga, S. Y. Lee, B. L. Choi, Y. Kuk, J. M. Kim, and K. Kim, "Full-colour quantum dot displays fabricated by transfer printing," *Nature Photonics*, vol. 5, pp. 176–182, feb 2011. (see p. 89)

[159] J. Bao and M. G. Bawendi, "A colloidal quantum dot spectrometer," *Nature*, vol. 523, pp. 67–70, jul 2015. (see p. 89)

[160] L. Huang, H. Xu, Z. Zhang, C. Chen, J. Jiang, X. Ma, B. Chen, Z. Li, H. Zhong, and L.-M. Peng, "Graphene/Si CMOS hybrid hall integrated circuits.," *Scientific reports*, vol. 4, p. 5548, jan 2014. (see p. 89)

[161] S. K. Banerjee, L. F. Register, E. Tutuc, D. Basu, S. Kim, D. Reddy, and A. H. MacDonald, "Graphene for CMOS and Beyond CMOS Applications," *Proceedings of the IEEE*, vol. 98, pp. 2032–2046, dec 2010. (see p. 89)

[162] A. B. Sachid, M. Tosun, S. B. Desai, C.-Y. Hsu, D.-H. Lien, S. R. Madhvapathy, Y.-Z. Chen, M. Hettick, J. S. Kang, Y. Zeng, J.-H. He, E. Y. Chang, Y.-L. Chueh, A. Javey, and C. Hu, "Monolithic 3D CMOS Using Layered Semiconductors.," *Advanced materials* , feb 2016. (see p. 89)

[163] M. Amani, R. A. Burke, R. M. Proie, and M. Dubey, "Flexible integrated circuits and multifunctional electronics based on single atomic layers of MoS2 and graphene.," *Nanotechnology*, vol. 26, p. 115202, mar 2015. (see p. 89)

List of publications

This thesis is based on the following publications:

- **Dominik Kufer**, Tania Lasanta, Maria Bernechea, Frank Koppens and Gerasimos Konstantatos, "Interface Engineering in hybrid Quantum Dot - 2D phototransistors", *submitted* (2016).
- **Dominik Kufer**, Ivan Nikitskiy, Tania Lasanta, Gabriele Navickaite, Frank Koppens, and Gerasimos Konstantatos, "Hybrid 2D/0D MoS_2/PbS quantum dot photodetectors", *Advanced Materials* 27, 176180 (2015).
- **Dominik Kufer** and Gerasimos Konstantatos, "Highly sensitive, encapsulated MoS_2 photodetector with gate controllable gain and speed", *Nano Letters* 15, 7307-7313 (2015).

Other publications by the author:

- I. Nikitskiy, S. Goossens, **D. Kufer**, T. Lasanta, G. Navickaite, F. Koppens and G. Konstantatos, "Integrating an electrically active colloidal quantum dot photodiode with a graphene phototransistor", *under review* 2016.
- H. Wang, F. Li, **D. Kufer**, W. Yu, E. Alarousu, C. Ma, Y. Li, Z. Liu, C. Liu, N. Wei, Y. Chen, F. Wang, L. Chen, O. F. Mohammed, A. Fratalocchi, G. Konstantatos, T. Wu, "Achieving ultrahigh carrier mobility and photo-responsivity in solution-processed perovskite/carbon nanotubes phototransistors", *submitted* 2016.
- S. L. Diedenhofen, **D. Kufer**,T. Lasanta and G. Konstantatos, "Integrated colloidal quan-tum dot photodetectors with color-tunable plasmonic nanofocusing lenses", *Light: Science & Applications* 4, e234 (2015).
- H. Tian, J. Verbeeck, S. Brück, M. Paul, **D. Kufer**,M. Sing, R. Claessen, and G. Van Tendeloo, "Interface-induced modulation of charge and polarization in thin film Fe3O4", *Advanced Materials* 26, 461 (2014).

- F. P. Garca de Arquer, A. Mihi, **D. Kufer** and G. Konstantatos, “Photoelectric energy conversion of plasmon-generated hot carriers in metal-insulator-semiconductor structures”, *ACS Nano* 7, 3581-3588 (2013).
- A. Mihi, M. Bernechea,, **D. Kufer** and G. Konstantatos, “Coupling resonant modes of em-bedded dielectric microspheres in solution-processed solar cells”, *Advanced Optical Materials* 1, 139-143 (2013)
- S. Brück, M. Paul, H. Tian, A. Müller, **D. Kufer** C. Praetorius, K. Fauth, P. Audehm, E. Goering, J. Verbeeck, G. van Tendeloo, M. Sing, and R. Claessen, “Magnetic and elec-tronic properties of the interface between half metallic Fe3O4 and semiconducting ZnO”, *Applied Physics Letters* 100, 081603 (2012)

Filed Patent by the author:

- EP14177172.5/ US14/800,320 ; Optolelectronic apparatus and fabrication method of the same; G. Konstantatos, F. Koppens, **D. Kufer**, I. Nikitskiy; (150714)